

IN SILICO INTERACTION
OF ADAPTIVE TISSUES AND DEVICES

A DISSERTATION
SUBMITTED TO THE DEPARTMENT OF MECHANICAL ENGINEERING
AND THE COMMITTEE ON GRADUATE STUDIES
OF STANFORD UNIVERSITY
IN PARTIAL FULFILLMENT OF THE REQUIREMENTS
FOR THE DEGREE OF
DOCTOR OF PHILOSOPHY

Alexander M Zöllner

March 2016

© 2016 by Alexander Martin Zoellner. All Rights Reserved.
Re-distributed by Stanford University under license with the author.

This dissertation is online at: <http://purl.stanford.edu/wt951gn6092>

I certify that I have read this dissertation and that, in my opinion, it is fully adequate in scope and quality as a dissertation for the degree of Doctor of Philosophy.

Ellen Kuhl, Primary Adviser

I certify that I have read this dissertation and that, in my opinion, it is fully adequate in scope and quality as a dissertation for the degree of Doctor of Philosophy.

Marc Levenston

I certify that I have read this dissertation and that, in my opinion, it is fully adequate in scope and quality as a dissertation for the degree of Doctor of Philosophy.

Charles Steele

Approved for the Stanford University Committee on Graduate Studies.

Patricia J. Gumport, Vice Provost for Graduate Education

This signature page was generated electronically upon submission of this dissertation in electronic format. An original signed hard copy of the signature page is on file in University Archives.

Abstract

Finite element simulations were introduced in the aviation industry in the 1970s and soon found their way into other industries as well as biomedical research. Since then, constitutive laws have been developed with the goal of building realistic organ level models and ultimately creating a whole human model. The attempts to model the fibrous soft tissue in the human body has led to the development of anisotropic models as conceived by Fung or Holzapfel and active muscle models as developed by Hill. These models have led to a better understanding of the underlying biomechanics in both passive and active systems and their interaction with devices or changing boundary conditions during disease. However, the human body's ability to adapt to boundary conditions, particularly in conjunction with devices or disease, has been ignored in most of these models. Here, I present constitutive laws for soft tissue adaptation, their implementation into general purpose finite element codes, and applications to clinically relevant problems. I applied a continuum mechanics framework to model the in-plane area growth of skin upon overstretch, the adaptation of skeletal muscle to changes in its mechanical environment, and the effect of annuloplasty ring sizes during mitral valve repair surgery. Our results demonstrate how the finite element method can be applied to model the interaction of adapting soft tissue with medical devices and changing mechanical changes in its environment. We anticipate our models to open new avenues in surgical planning and to enhance the treatment of patients in both plastic and cardiovascular surgery. Furthermore, I expect these models to be used by medical device manufacturers as part of their computer-aided engineering pipelines.

Acknowledgements

I would like to take this opportunity to thank the people who have contributed to this thesis in many different ways.

Firstly, I would like to thank my advisor Prof. Ellen Kuhl for her continuous support of my PhD research, for her patience, motivation, and immense knowledge. Her guidance has helped me during my time at Stanford and I could not imagine a better advisor, mentor, and teacher.

Besides my advisor, I would like to thank Prof. Marc Levenston and Prof. Charles Steele for being members of my reading committee as well as Prof. Sunil Puria and Prof. John Lipa for being part of my defense committee.

I also want to thank my co-authors for their help and contribution to my published research work. Special thanks go to Uwe Raaz and Oscar Abilez for the opportunity to transduce theory into practice.

I thank the former and current living matter lab members Manuel Rausch, Jonathan Wong, Adrian Buganza, Corey Murphy, Maria Holland, Mona Eskandari, Annette Böhmer, Jaqi Pok, Martin Genet, Jacob Gowan, Rijk de Rooij, Francisco Sahli, Moritz Mangold, Johannes Weickenmeier, Caitlin Ploch, and Doreen Wood.

Thanks to Jan and Annette Hennigs and Kiril Penov for your medical expertise and patience answering every single one of my questions.

Last but not the least, I would like to thank my family. Thank you to my parents Armin and Heidi Zöllner for their unconditional support and patience. Finally, I want to thank my brother Andreas Zöllner who has always been my best friend for his help and opinion over more than 20 years.

Contents

Abstract	iv
Acknowledgements	v
Introduction	1
1 Tissue expansion in Lagrangian Formulation	4
1.1 Motivation	4
1.2 Methods	7
1.3 Results	15
1.4 Discussion	18
2 Tissue expansion in Eulerian formulation	25
2.1 Motivation	26
2.2 Methods	29
2.3 Results	32
2.4 Discussion	38
2.5 Conclusion	44
3 Realistic, volume controlled skin expander model	45
3.1 Mechanobiology Of Growing Skin	46
3.2 Histology Of Growing Skin	51
3.3 Continuum Modeling Of Growing Skin	52
3.4 Computational Modeling Of Growing Skin	54
3.5 Simulation Of Growing Skin	56
3.6 Discussion	64
3.7 Conclusion	68

4	Chronic muscle lengthening through sarcomerogenesis	70
4.1	Introduction	71
4.2	Methods	73
4.3	Results	77
4.4	Discussion	87
4.5	Conclusion	88
4.6	Acknowledgments	89
5	A multiscale model for sarcomere loss	90
5.1	Motivation	91
5.2	Methods	93
5.3	Results	101
5.4	Discussion	107
5.5	Concluding remarks	109
6	A virtual sizing tool for mitral valve annuloplasty	111
6.1	Motivation	111
6.2	Methods	114
6.3	Results	117
6.4	Discussion	121
	Conclusions	125
	Bibliography	128

List of Tables

1.1	Algorithmic flowchart for strain-driven transversely isotropic area growth	14
4.1	Material parameters for elastic model and growth model	77
4.2	Sarcomere lengths in chronically stretched skeletal muscle	79
5.1	Dimensions of muscle tendon unit in flat foot and high heel positions	99
5.2	Muscle fiber orientations in the gastrocnemius muscle	100
6.1	Annular dimensions of healthy and dilated annulus	118
6.2	Annular dimensions with 24 mm, 28 mm, and 32 mm diameter Physio rings implanted	121
6.3	Suture forces upon ring implantation	122

List of Figures

1.1	Tissue expansion for pediatric forehead reconstruction	5
1.2	Schematic sequence of tissue expander inflation	6
1.3	Tissue expander to grow skin for defect correction in reconstructive surgery	7
1.4	Tissue expansion in equi-biaxial stretch	11
1.5	Three-dimensional computer tomography scans from the skull of a one-year old child	14
1.6	Mesh generation from clinical images	16
1.7	Temporal evolution of tissue expansion in the scalp	17
1.8	Spatio-temporal evolution of tissue expansion in the scalp	18
1.9	Remaining deformation after tissue expansion in the scalp	19
1.10	Temporal evolution of tissue expansion in the forehead	19
1.11	Spatio-temporal evolution of tissue expansion in the forehead	20
1.12	Remaining deformation after issue expansion in the forehead	20
1.13	Temporal evolution of tissue expansion in the cheek	21
1.14	Spatio-temporal evolution of tissue expansion in the cheek	22
1.15	Remaining deformation tissue expansion in the cheek	23
2.1	Mechanotransduction of growing skin	26
2.2	Biomechanics of growing skin	28
2.3	Temporal evolution of total area for displacement driven skin expansion	33
2.4	Temporal evolution of skin thickness t for displacement driven skin expansion	34
2.5	Skin expansion in pediatric forehead reconstruction	36
2.6	Skin expansion in pediatric forehead reconstruction	37
2.7	Spatio-temporal evolution of area for case study I	38
2.8	Temporal evolution of normalized area for case study II	39
2.9	Spatio-temporal evolution of area for case study II	40
3.1	Skin expansion in pediatric scalp reconstruction	46
3.2	Histological cross section of human skin	48
3.3	Mechanotransduction of growing skin	50

3.4	Histological sections of expanded and non-expanded skin	51
3.5	Filling volume of skin expanders over time	57
3.6	Skin growth over time	58
3.7	Expander pressure during skin expansion	59
3.8	Spatio-temporal evolution of skin growth upon tissue expansion	60
3.9	Spatio-temporal evolution of von Mises stress during skin growth upon tissue expansion	61
3.10	Spatio-temporal evolution of growth multiplier during skin growth upon tissue expansion	63
4.1	Sarcomere units in striated muscle	71
4.2	Stretching skeletal muscle	72
4.3	Temporal evolution of sarcomere length l_s in stretched skeletal muscle	78
4.4	Temporal evolution of serial sarcomere number ϑ in stretched skeletal muscle	79
4.5	Single-step stretching vs multi-step stretching of skeletal muscle	80
4.6	Temporal evolution of muscle stretch λ , muscle stress σ/σ_0 , serial sarcomere number ϑ , and sarcomere length l_s in chronically stretched skeletal muscle	81
4.7	Finite element model of biceps brachii muscle	82
4.8	Spatio-temporal evolution of sarcomere length l_s/l_o	83
4.9	Spatio-temporal evolution of serial sarcomere number ϑ	84
4.10	Temporal evolution of average sarcomere length l_s/l_o	85
4.11	Temporal evolution of serial sarcomere number ϑ	86
5.1	Chronic muscle adaptation across the scales	91
5.2	Chronic muscle adaptation on the sarcomere scale	92
5.3	Sagittal magnetic resonance images of the right lower limb of a healthy 20-year old female subject	97
5.4	Generation of finite element model from magnetic resonance images of the lower limb	97
5.5	Finite element model of the lower limb	98
5.6	Muscle fiber orientation model of the gastrocnemius muscle	100
5.7	Finite element model of muscle shortening in response to frequent high heel use . . .	101
5.8	Acute decrease in sarcomere length when switching from flat footwear to high heels .	103
5.9	Chronic increase in sarcomere length when frequently wearing high-heeled footwear .	104
5.10	Chronic decrease in sarcomere length when frequently wearing high-heeled footwear	104
5.11	Chronic increase in sarcomere length when switching from flat footwear to high heels	105
5.12	Chronic decrease in sarcomere number when switching from flat footwear to high heels	105
5.13	Acute increase in sarcomere length when switching from high heels to flat footwear .	106
6.1	Mitral annuloplasty	112
6.2	The Living Heart model	113

6.3	Using the Living Heart model as virtual sizing tool for mitral annuloplasty	117
6.4	Two chamber and four chamber views of the heart before and after ventricular re-modeling in response to diastolic overload	118
6.5	Two chamber and four chamber views of the heart before and after annular dilation in response to diastolic overload	119
6.6	Two chamber and four chamber views of the heart after virtual ring implantation . .	120
6.7	Annular stretch in the healthy and dilated annulus, and after ring-implantation . . .	121

Introduction

Motivation

What if surgical outcomes and medical device performance could be predicted in the same way that crash test simulations predict the crashworthiness of automobiles? The human body and its organs, despite being more familiar to most of us than for example cars, are infathomably complex systems that are much less understood than designed engineering systems [153]. A layer of complexity unknown to engineering systems and materials is the ability of tissue and organs to heal, grow, and regenerate [197]. When living tissue is damaged, it is automatically repaired through an orchestrated cascade of inflammation, tissue growth, and tissue remodeling. Similarly, when living tissue is overstretched or overstressed, a cascade of biochemical events forms new tissue. In the extreme, some species like the axolotl are capable of regenerating entire lost limbs [35]. While the human body adapts to a variety of thermal, radiological, electrical, biochemical, or mechanical boundary conditions and loads, mechanical changes are the most relevant for surgical procedures and medical device development [185]. Typical phenomena observed in healthcare include cardiac growth upon hypertension or dilation, sarcomerogenesis or sarcomere loss upon chronic muscle over or under stretch, and skin growth through controlled tissue expansion. All these applications are highly nonlinear in terms of the underlying elasticity model, the growth model, geometry, and boundary conditions. Common options to characterize the baseline elasticity of these biological tissues are neo-Hookean, Fung type, or Holtzapfel material models [90]. In addition to the baseline elasticity, a suitable material model needs to include a growth component to describe the addition or loss of sarcomeres, skin area, or more generally mass. The choice of growth model depends on the clinically observed phenomena [197]. In addition to influence of the different boundary conditions, it is important to note that wide range of tissue and their mechanical responses. Overstretched skeletal muscle is, for example, typically associated with one dimensional growth along a preferred fiber direction while skin growth is typically linked to growth in two dimensions, normal to the skin surface.

Goals

The goal of this dissertation was to create in silico tissue adaptation models for a different clinical scenarios. I derived the governing equations of growing biological tissues. I implemented these equations in the scientific computing framework MATLAB for testing and calibrating. Ultimately, these equations were solved using nonlinear finite element methods. To simulate large systems the equations were implemented efficiently as a user-defined material subroutine into the general purpose finite element code ABAQUS. I demonstrated the clinical applications of the growth models using custom built three-dimensional meshes based on clinical imaging data.

Contributions

Constitutive model for skin growth

Motivated by the work of Buganza et al. [36], I have derived a universal, three-dimensional, modular framework for the simulation of skin growth on arbitrary geometries. A Lagrangian setting was used for the initial formulation [224]. To improve the computational efficiency and stability a second version was derived in Eulerian setting [225]. Both algorithms were implemented in the general purpose finite element code FEAP [205]. Subsequently, the improved algorithm was implemented into the commercial finite element code ABAQUS Standard as a user subroutine (UMAT) [1].

Constitutive Model for Muscle Adaptation

Motivated by animal experiments, I have developed a constitutive model for sarcomerogenesis, the serial addition of sarcomere units in response to passive skeletal muscle overstretch [227]. Similar to sarcomerogenesis, a model for sarcomere loss after chronic muscle understretch was developed [229]. Both models were combined into a skeletal muscle adaptation framework and implemented into ABAQUS Standard. The result is efficient, modular, and can be controlled using scalar field variables for realistic simulations.

3D Skin Model of Pediatric Head

I created a modular, high definition finite element model of a pediatric head. Despite its anatomical complexity and multi-layered structure, the model has a relatively low number of degrees of freedom. This allows for quick turnaround times that models created by commercial software, to date, cannot provide. As I have demonstrated, this model can be used to simulate realistic skin expansion and plan reconstructive surgery in different settings.

3D Model of Human Lower Limb

Based on magnetic resonance imaging data, I have build a finite element model of the human lower limb including fibula, tibia, and tarsal bones, as well as calceal tendon, and gastrocnemius muscle. The model features a smooth node connected interface between the muscle and tendon that does not require a computationally expensive contact model [102] and allows for highly efficient simulations.

3D Modular Annuloplasty Model

Based on the Simulia Living Heart Project, I created a virtual model of dilated cardiomyopathy and implanted three mitral valve annuloplasty rings to reduce the size of the dilated mitral annulus. The created model is highly modular and can be used to simulate the effect of different annuloplasty rings and ring sizes to quantify the suture forces, myocardial strain, and annular stretch after mitral annuloplasty surgery.

Overview

The individual chapters of this thesis have been originally published as peer reviewed journal articles. A short description of each of these chapters is given in the following. The first chapter presents the skin expansion model in Lagrangian formulation and demonstrates its applications during pediatric forehead reconstruction. The skin expander is modeled as a subset of elements under continuous pressure. The second chapter presents the skin expansion model in Eulerian setting. The expression of the stress and tangent in material configuration increases the efficiency threefold compared to the previous Lagrangian model. The simulations for the first two chapters were run in the Finite Element Analysis Program (FEAP). The simulations in the third chapter employ the Eulerian model introduced in chapter two, implemented into the commercial finite element code Abaqus Standard. For the first time, volume controlled expanders are used to simulate skin expansion following a clinical protocol. The fourth chapter presents a sarcomerogenesis model for skeletal muscle. The model in Eulerian setting was implemented in Abaqus Standard. The model parameters were found calibrating it using murine data before the model was applied to simulate a limb lengthening procedure. The fifth chapter presents a material model for sarcomere loss in skeletal muscle. A three-dimensional model of the lower human limb was created from medical imaging. The material model and the geometric model were used to simulate the effect of excessive plantarflexion on the human gastrocnemius muscle in women wearing high heeled footwear. In chapter six a mitral valve annuloplasty surgery on a dilated heart was simulated. The Abaqus Living Heart model was used to simulate the effect of different annuloplasty ring sizes on the surgery outcome was evaluated both qualitatively and quantitatively.

Chapter 1

Tissue expansion in Lagrangian Formulation

Abstract

Tissue expansion is a common surgical procedure to grow extra skin through controlled mechanical over-stretch. It creates skin that matches the color, texture, and thickness of the surrounding tissue, while minimizing scars and risk of rejection. Despite intense research in tissue expansion and skin growth, there is a clear knowledge gap between heuristic observation and mechanistic understanding of the key phenomena that drive the growth process. Here, we show that a continuum mechanics approach, embedded in a custom-designed finite element model, informed by medical imaging, provides valuable insight into the biomechanics of skin growth. In particular, we model skin growth using the concept of an incompatible growth configuration. We characterize its evolution in time using a second-order growth tensor parameterized in terms of a scalar-valued internal variable, the in-plane area growth. When stretched beyond the physiological level, new skin is created, and the in-plane area growth increases. For the first time, we simulate tissue expansion on a patient-specific geometric model, and predict stress, strain, and area gain at three expanded locations in a pediatric skull: in the scalp, in the forehead, and in the cheek. Our results may help the surgeon to prevent tissue over-stretch and make informed decisions about expander geometry, size, placement, and inflation. We anticipate our study to open new avenues in reconstructive surgery, and enhance treatment for patients with birth defects, burn injuries, or breast tumor removal.

1.1 Motivation

One percent of neonates is born with congenital melanocytic nevi, dark-colored surface lesions present at birth [45]. Congenital nevi may vary in size, shape, texture, color, hairiness, and location, but they have one thing in common: their high malignant potential [100]. Birthmarks larger than 10 cm



Figure 1.1: Tissue expansion for pediatric forehead reconstruction. The patient, a one-year old boy presented with a giant congenital nevus involving 25 percent of his forehead, extending to the right temporal scalp and cheek. Simultaneous forehead, cheek, and scalp expanders were implanted for in situ skin growth. This technique allows to resurface large anatomical areas with skin of similar color, quality, and texture. The follow-up photograph shows the boy at age three, after completed forehead, scalp, and cheek reconstruction.

in diameter are classified as giant congenital nevi and have a prevalence of one in 20,000 infants [172]. Because giant congenital nevi place the child at an increased risk to develop skin cancer, surgical excision remains the standard treatment option [81]. Cosmetic deformity, significant aesthetic disfigurement, and severe psychological distress are additional compelling reasons for nevus removal, especially in the craniofacial region [100].

To reconstruct the defect, preserve function, and maintain aesthetic appearance, tissue expansion has become a major treatment modality in the management of giant congenital nevi [137]. Tissue expansion was first proposed more than half a century ago to reconstruct a traumatic ear and has since then revolutionized reconstructive surgery [154]. Today it is widely used to repair birth defects [11], correct burn injuries [9], and reconstruct breasts after tumor removal [173]. Tissue expansion is the ideal strategy to grow skin that matches the color, texture, hair bearance, and thickness of the surrounding healthy skin, while minimizing scars and risk of rejection [181].

Figure 1.1, left, shows a one-year old boy who presented with a giant congenital nevus concerning 25 percent of his forehead, extending to the right temporal scalp and cheek [83]. To resurface the nevus region and stimulate in situ skin growth, three simultaneous forehead, cheek, and scalp expanders are used. They are implanted in subcutaneous pockets adjacent to the defect, where they are gradually filled with saline solution. The amount of filling is controlled by visual inspection of skin color and capillary refill [181]. Multiple serial inflations stretch the skin and stimulate tissue growth over a period of several weeks [222]. Once enough skin is created, the expanders are removed, the nevus

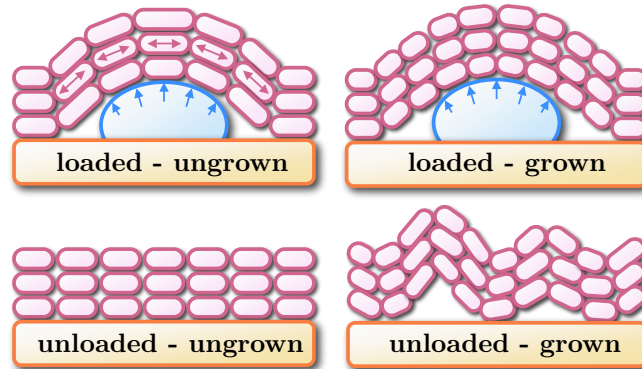


Figure 1.2: Schematic sequence of tissue expander inflation. At biological equilibrium, the skin is in a physiological state of resting tension, unloaded and ungrown. When an expander is implanted and inflated, the skin is stretched, loaded and ungrown. Mechanical stretch beyond a critical level triggers a series of signaling pathways eventually leading to the creation of new skin to restore the state of resting tension, loaded and grown. Upon expander removal, elastic deformations retract and inelastic deformations remain, unloaded and grown.

is excised, and the newly grown skin flaps are advanced to close the defect zone. Figure 1.1, right, shows the boy at age three, after completed forehead, scalp, and cheek reconstruction.

Figure 1.2 shows a schematic sequence of the mechanical processes during tissue expansion. Initially, at biological equilibrium, the skin is in a natural state of resting tension [191]. When the expander is implanted and inflated, skin is loaded in tension. Stretch beyond a critical level triggers a series of signaling pathways eventually leading to the creation of new skin [203]. On the cellular level, mechanotransduction affects a network of several integrated cascades including growth factors, cytoskeletal rearrangement, and protein kinases [55]. On the tissue level, skin growth induces stress relaxation and restores the state of resting tension [191]. The cycle of expander inflation, stretch, growth, and relaxation is repeated multiple times, typically on a weekly basis [222]. As demonstrated by immunocytochemistry, the expanded tissue undergoes normal cell differentiation and maintains its characteristic phenotype [218]. Skin initially displays thickness changes upon expansion, however, these changes are fully reversible upon expander removal [210]. When the expander is removed, the skin retracts and reveals the irreversible nature of skin growth, associated with growth-induced residual stresses [77, 149]. Figure 1.3 shows a commonly used tissue expander to grow skin in reconstructive surgery.

To predict stress, strain, and area gain during tissue expansion in pediatric forehead reconstruction, we adopt a novel mechanistic approach [36, 37], based on the continuum framework of finite growth [183]. Originally developed for isotropic volumetric growth [62, 139], finite growth theories are based on the multiplicative decomposition of the deformation gradient into an elastic and a growth part [67, 140], a concept adopted from finite plasticity [125]. Depending on the format of their growth tensor, continuum growth theories have been refined to characterize isotropic [79, 118],



Figure 1.3: Tissue expander to grow skin for defect correction in reconstructive surgery. Typical applications are birth defects, burn injuries, and breast reconstruction. Devices consist of a silicone elastomer inflatable expander with a reinforced base for directional expansion, and a remote silicone elastomer injection dome. Courtesy of Mentor Worldwide LLC.

transversely isotropic [176, 197], orthotropic [72], or generally anisotropic growth [148, 150], either compressible [148] or incompressible [186]. Recent trends focus on the computational modeling of finite growth [87], typically by introducing the growth tensor as an internal variable within a finite element framework [71, 110], a strategy that we also adopt here. A recent monograph that compares different approaches to growth and summarizes the essential findings, trends, and open questions in this progressively evolving new field [6]. Despite ongoing research in growing biological systems, the growth of thin biological membranes remains severely understudied. Only few attempts address the growth of thin biological plates [56] and membranes [148]. Motivated by a first study on axisymmetric skin growth [193], we have recently established a prototype model for growing membranes to predict skin expansion in a general three-dimensional setting [36]. This study capitalizes on recent developments in reconstructive surgery, continuum mechanics of growing tissues, and computational modeling, supplemented by medical image analysis. It documents our first attempts to model and simulate skin expansion in pediatric forehead reconstruction using a real patient-specific geometry.

1.2 Methods

1.2.1 Continuum modeling of skin growth

We adopt the kinematics of finite deformations and introduce the deformation map φ , which, at any given time t maps the material placement \mathbf{X} of a physical particle in the material configuration to its spatial placement \mathbf{x} in the spatial configuration, $\mathbf{x} = \varphi(\mathbf{X}, t)$. We choose a formulation which is entirely related to the material frame of reference, and use $\nabla\{\circ\} = \partial_{\mathbf{X}}\{\circ\}|_t$ and $\text{Div}\{\circ\} = \partial_{\mathbf{X}}\{\circ\}|_t : \mathbf{I}$ to denote the gradient and the divergence of any field $\{\circ\}(\mathbf{X}, t)$ with respect to the material placement \mathbf{X} at fixed time t . Here, \mathbf{I} is the material identity tensor. To characterize finite growth, we introduce an incompatible growth configuration, and adopt the multiplicative decomposition of the deformation gradient

$$\mathbf{F} = \nabla_{\mathbf{X}}\varphi = \mathbf{F}^e \cdot \mathbf{F}^g \quad (1.1)$$

into a reversible elastic part \mathbf{F}^e and an irreversible growth part \mathbf{F}^g . This multiplicative decomposition, reminiscent of the decomposition of the elastoplastic deformation gradient [125], was first used to describe growth of biological tissues in [183]. Similarly, we can then decompose the total Jacobian

$$J = \det(\mathbf{F}) = J^e J^g \quad (1.2)$$

into an elastic part $J^e = \det(\mathbf{F}^e)$ and a growth part $J^g = \det(\mathbf{F}^g)$. We idealize skin as a thin layer characterized through the unit normal \mathbf{n}_0 in the undeformed reference configuration. The length of the deformed skin normal $\mathbf{n} = \text{cof}(\mathbf{F}) \cdot \mathbf{n}_0 = J \mathbf{F}^{-t} \cdot \mathbf{n}_0$ introduces the area stretch

$$\vartheta = \|\text{cof}(\mathbf{F}) \cdot \mathbf{n}_0\| = \vartheta^e \vartheta^g \quad (1.3)$$

which we can again decompose into an elastic area stretch $\vartheta^e = \|\text{cof}(\mathbf{F}^e) \cdot \mathbf{n}_g / \|\mathbf{n}_g\|\|$ and a growth area stretch $\vartheta^g = \|\text{cof}(\mathbf{F}^g) \cdot \mathbf{n}_0\|$ [36]. Here, $\mathbf{n}_g = \text{cof}(\mathbf{F}^g) \cdot \mathbf{n}_0 = J^g \mathbf{F}^{g-t} \cdot \mathbf{n}_0$ denotes the grown skin normal, and $\text{cof}(\circ) = \det(\circ) (\circ)^{-t}$ denotes the cofactor of the second order tensor (\circ) . As characteristic deformation measures, we introduce the right Cauchy Green tensor \mathbf{C} in the undeformed reference configuration

$$\mathbf{C} = \mathbf{F}^t \cdot \mathbf{F} = \mathbf{F}^{gt} \cdot \mathbf{F}^{et} \cdot \mathbf{F}^e \cdot \mathbf{F}^g \quad (1.4)$$

and its elastic counterpart $\mathbf{C}^e = \mathbf{F}^{et} \cdot \mathbf{F}^e = \mathbf{F}^{g-t} \cdot \mathbf{C} \cdot \mathbf{F}^{g-1}$ in the intermediate configuration. This allows us to rephrase the total area stretch as $\vartheta = J [\mathbf{n}_0 \cdot \mathbf{C}^{-1} \cdot \mathbf{n}_0]^{1/2}$. Finally, we introduce the pull back of the spatial velocity gradient $\mathbf{l} = \dot{\mathbf{F}} \cdot \mathbf{F}^{-1}$ to the intermediate configuration,

$$\mathbf{F}^{e-1} \cdot \mathbf{l} \cdot \mathbf{F}^e = \mathbf{L}^e + \mathbf{L}^g \quad (1.5)$$

which obeys the additive decomposition into the elastic velocity gradient $\mathbf{L}^e = \mathbf{F}^{e-1} \cdot \dot{\mathbf{F}}^e$ and the growth velocity gradient $\mathbf{L}^g = \dot{\mathbf{F}}^g \cdot \mathbf{F}^{g-1}$. Here, $\{\dot{\circ}\} = \partial_t \{\circ\}|_{\mathbf{X}}$ denotes the material time derivative of any field $\{\circ\}(\mathbf{X}, t)$ at fixed material placement \mathbf{X} .

We characterize growing tissue using the framework of open system thermodynamics in which the material density ρ_0 is allowed to change as a consequence of growth [112, 114]. The balance of mass for open systems balances its rate of change $\dot{\rho}_0$ with a possible in- or outflux of mass \mathbf{R} and mass source \mathcal{R}_0 [115, 165].

$$\dot{\rho}_0 = \text{Div}(\mathbf{R}) + \mathcal{R}_0 \quad (1.6)$$

Similarly, the balance of linear momentum balances the density-weighted rate of change of the velocity $\rho_0 \mathbf{v} = \rho_0 \dot{\boldsymbol{\varphi}}$, with the momentum flux $\mathbf{P} = \mathbf{F} \cdot \mathbf{S}$, and the momentum source $\rho_0 \mathbf{b}$,

$$\rho_0 \dot{\mathbf{v}} = \text{Div}(\mathbf{F} \cdot \mathbf{S}) + \rho_0 \mathbf{b} \quad (1.7)$$

here stated in its mass-specific form [113]. \mathbf{P} and \mathbf{S} are the first and second Piola-Kirchhoff stress tensors. Last, we would like to point out that the dissipation inequality for open systems

$$\rho_0 \mathcal{D} = \mathbf{S} : \frac{1}{2} \dot{\mathbf{C}} - \rho_0 \dot{\psi} - \rho_0 \mathcal{S} \geq 0 \quad (1.8)$$

typically contains an extra entropy source $\rho_0 \mathcal{S}$ to account for the growing nature of living biological systems [112, 149]. Equations (1.7) and (1.8) represent the mass-specific versions of the balance of momentum and of the dissipation inequality which are particularly useful in the context of growth since they contains no explicit dependencies on the changes in mass [113].

To close the set of equations, we introduce the constitutive equations for the mass source \mathcal{R}_0 , for the momentum flux \mathbf{S} , and for the growth tensor \mathbf{F}^g , assuming that the mass flux $\mathbf{R} = \mathbf{0}$, the momentum source $\mathbf{b} = \mathbf{0}$, and the acceleration $\dot{\mathbf{v}} = \mathbf{0}$ are negligibly small. On the cellular level, immunocytochemistry has shown that expanded tissue undergoes normal epidermal cell differentiation [218]. On the organ level, mechanical testing has confirmed that the newly grown skin has the same material properties as the initial tissue [222]. Accordingly, we assume that the newly grown skin has the same density as the initial tissue. This implies that the mass source

$$\mathcal{R}_0 = \rho_0 \operatorname{tr}(\mathbf{L}^g) \quad (1.9)$$

can be expressed as the density-weighted trace of the growth velocity gradient $\operatorname{tr}(\mathbf{L}^g) = \dot{\mathbf{F}}^g : \mathbf{F}^{g-t}$ [87]. We model skin as a hyperelastic material characterized through the Helmholtz free energy $\psi = \hat{\psi}(\mathbf{C}, \mathbf{F}^g)$, which we use to evaluate the dissipation inequality (1.8).

$$\rho_0 \mathcal{D} = \left[\mathbf{S} - \rho_0 \frac{\partial \psi}{\partial \mathbf{C}} \right] : \frac{1}{2} \dot{\mathbf{C}} + \mathbf{M}^e : \mathbf{L}^g - \rho_0 \frac{\partial \psi}{\partial \rho_0} \mathcal{R}_0 - \rho_0 \mathcal{S}_0 \geq 0 \quad (1.10)$$

We observe that the Mandel stress of the intermediate configuration $\mathbf{M}^e = \mathbf{C}^e \cdot \mathbf{S}^e$ is energetically conjugate to the growth velocity gradient $\mathbf{L}^g = \dot{\mathbf{F}}^g \cdot \mathbf{F}^{g-1}$. From the dissipation inequality (1.10), we obtain the definition of the second Piola Kirchhoff stress \mathbf{S} as thermodynamically conjugate quantity to the right Cauchy Green deformation tensor \mathbf{C} .

$$\mathbf{S} = 2 \rho_0 \frac{\partial \psi}{\partial \mathbf{C}} = 2 \frac{\partial \psi}{\partial \mathbf{C}^e} : \frac{\partial \mathbf{C}^e}{\partial \mathbf{C}} = \mathbf{F}^{g-1} \cdot \mathbf{S}^e \cdot \mathbf{F}^{g-t} \quad (1.11)$$

According to this definition, the first derivative of the Helmholtz free energy ψ with respect to the elastic right Cauchy Green tensor \mathbf{C}^e introduces the elastic second Piola Kirchhoff stress \mathbf{S}^e , while the second derivative defines the elastic constitutive moduli \mathbf{L}^e .

$$\mathbf{S}^e = 2 \rho_0 \frac{\partial \psi}{\partial \mathbf{C}^e} \quad \text{and} \quad \mathbf{L}^e = 2 \frac{\partial \mathbf{S}^e}{\partial \mathbf{C}^e} = 4 \rho_0 \frac{\partial^2 \psi}{\partial \mathbf{C}^e \otimes \partial \mathbf{C}^e} \quad (1.12)$$

To focus on the impact of growth, rather than adopting a sophisticated anisotropic material model for skin [37, 116], we assume a classical Neo-Hookean free energy $\rho_0 \psi = \frac{1}{2} \lambda \ln^2(J^e) + \frac{1}{2} \mu [\mathbf{C}^e : \mathbf{I} - 3 - 2 \ln(J^e)]$, introducing the elastic second Piola Kirchhoff stress $\mathbf{S}^e = [\lambda \ln(J^e) - \mu] \mathbf{C}^{e-1} + \mu \mathbf{I}$, and the elastic constitutive moduli $\mathbf{L}^e = \lambda \mathbf{C}^{e-1} \otimes \mathbf{C}^{e-1} + [\mu - \lambda \ln(J^e)] [\mathbf{C}^{e-1} \otimes \mathbf{C}^e + \mathbf{C}^e \otimes \mathbf{C}^{e-1}]$. Motivated by clinical observations [181], we classify skin growth as a strain-driven, transversely isotropic, irreversible process. It is characterized through one single growth multiplier ϑ^g that reflects the irreversible area increase perpendicular to the skin normal \mathbf{n}_0 .

$$\mathbf{F}^g = \sqrt{\vartheta^g} \mathbf{I} + [1 - \sqrt{\vartheta^g}] \mathbf{n}_0 \otimes \mathbf{n}_0 \quad (1.13)$$

For this particular type of transversely isotropic growth, for which all thickness changes are reversibly elastic [210], area growth is identical to volume growth, i.e., $\vartheta^g = \det(\mathbf{F}^g) = J^g$. Because of the simple rank-one update structure in (1.13), we can invert the growth tensor explicitly, $\mathbf{F}^{g-1} = 1/\sqrt{\vartheta^g} \mathbf{I} + [1 - 1/\sqrt{\vartheta^g}] \mathbf{n}_0 \otimes \mathbf{n}_0$, using the Sherman-Morrison formula. This explicit representation introduces the following simple expression for the growth velocity gradient,

$$\mathbf{L}^g = \sqrt{\dot{\vartheta}^g}/\sqrt{\vartheta^g} \mathbf{I} + [1 - \sqrt{\dot{\vartheta}^g}/\sqrt{\vartheta^g}] \mathbf{n}_0 \otimes \mathbf{n}_0 \quad (1.14)$$

which proves convenient to explicitly evaluate the mass source in equation (1.9) as $\mathcal{R}_0 = \rho_0 [1 + 2\sqrt{\dot{\vartheta}^g}/\sqrt{\vartheta^g}]$. Motivated by physiological observations of stretch-induced skin expansion [83], we adopt the following evolution equation for the growth multiplier,

$$\dot{\vartheta}^g = k^g(\vartheta^g) \phi^g(\vartheta^e) \quad (1.15)$$

which follows a well-established functional form [139], but is now rephrased in a strain-driven format [72]. To control unbounded growth, we introduce the weighting function

$$k^g = \frac{1}{\tau} \left[\frac{\vartheta^{\max} - \vartheta^g}{\vartheta^{\max} - 1} \right]^\gamma \quad (1.16)$$

where $1/\tau$ controls the adaptation speed, the exponent γ calibrates the shape of the growth curve, and $\vartheta^{\max} > 1$ is the maximum area growth [87, 139]. The growth criterion

$$\phi^g = \langle \vartheta^e - \vartheta^{\text{crit}} \rangle = \langle \vartheta/\vartheta^g - \vartheta^{\text{crit}} \rangle \quad (1.17)$$

is driven by the elastic area stretch $\vartheta^e = \vartheta/\vartheta^g$, such that growth is activated only if the elastic area stretch exceeds a critical physiological stretch limit ϑ^{crit} . Here, $\langle \circ \rangle$ denote the Macaulay brackets. Figure 1.4 displays the constitutive response of the four-parameter growth model in equi-biaxial stretch. At a prescribed piecewise constant total stretch ϑ , the growth stretch ϑ^g increases gradually while the elastic stretch ϑ^e decreases. This induces stress relaxation. Horizontal dashed lines

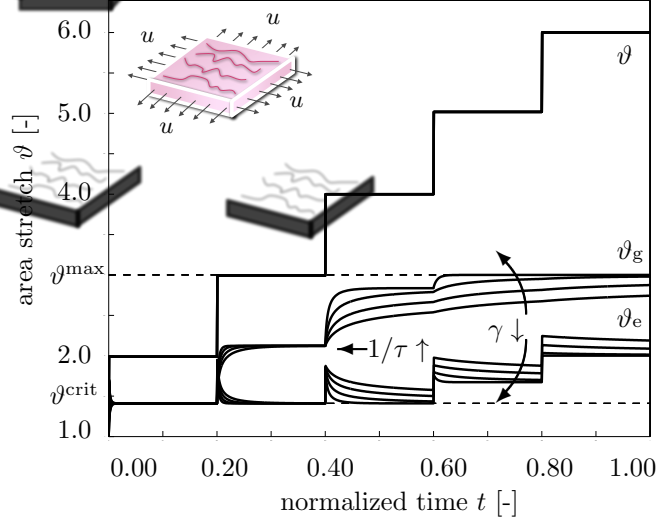


Figure 1.4: Tissue expansion in equi-biaxial stretch. Temporal evolution of total, elastic, and growth area stretch ϑ , ϑ^e , and ϑ^g for displacement driven skin expansion at varying growth exponents γ . At a piecewise constant total stretch, the growth stretch increases gradually while the elastic stretch decreases. This induces stress relaxation. Horizontal dashed lines represent the elastic stretch limit beyond which skin growth is activated ϑ^{crit} , and the maximum area growth ϑ^{max} .

represent the elastic stretch limit beyond which skin growth is activated ϑ^{crit} and the maximum area growth ϑ^{max} . Increased adaptation speeds $1/\tau \uparrow$ and decreased growth exponents $\gamma \downarrow$ both accelerate convergence towards the biological equilibrium [87], but do not affect the final equilibrium state [176, 186]. At all times, the multiplicative decomposition of the deformation gradient $\mathbf{F} = \mathbf{F}^e \cdot \mathbf{F}^g$ introduced in equation (1.1) carries over to the multiplicative decomposition of the total area stretch $\vartheta = \vartheta^e \vartheta^g$ of equation (1.3).

1.2.2 Computational modeling of skin growth

We solve the coupled biological and mechanical equilibrium for skin growth within an incremental iterative finite element setting [207]. To characterize the growth process at each instant in time, we introduce the growth multiplier ϑ^g as an internal variable, and solve the biological equilibrium (1.15) locally at the integration point level. For the temporal discretization, we partition the time interval of interest \mathcal{T} into n_{stp} subintervals, $\mathcal{T} = \mathbf{U}_{n=1}^{n_{\text{stp}}} [t_n, t_{n+1}]$ and focus on the interval $[t_n, t_{n+1}]$ for which $\Delta t = t_{n+1} - t_n > 0$ denotes the current time increment. Our goal is to determine the current growth multiplier ϑ^g for a given deformation state \mathbf{F} at time t , and a given growth multiplier ϑ_n^g at the end of the previous time step t_n . For the sake of compactness, we omit the index $(\circ)_{n+1}$ for all quantities at the end of the current time step t_{n+1} . We evaluate the material time derivative of the growth multiplier $\dot{\vartheta}^g = [\vartheta^g - \vartheta_n^g] / \Delta t$ using a finite difference approximation. In the spirit of implicit time integration schemes, we now reformulate the evolution equation (1.15), introducing

the discrete residual \mathbf{R}^ϑ in terms of the unknown growth multiplier $\vartheta^\mathfrak{g}$.

$$\mathbf{R}^\vartheta = \vartheta^\mathfrak{g} - \vartheta_n^\mathfrak{g} - k^\mathfrak{g} \phi^\mathfrak{g} \Delta t \doteq 0 \quad (1.18)$$

We solve this nonlinear residual equation using a local Newton iteration. Within each iteration step, we calculate the linearization of the residual \mathbf{R}^ϑ with respect to the growth multiplier $\vartheta^\mathfrak{g}$,

$$\mathbf{K}^\vartheta = \frac{\partial \mathbf{R}^\vartheta}{\partial \vartheta^\mathfrak{g}} = 1 - \left[\frac{\partial k^\mathfrak{g}}{\partial \vartheta^\mathfrak{g}} \phi^\mathfrak{g} + k^\mathfrak{g} \frac{\partial \phi^\mathfrak{g}}{\partial \vartheta^\mathfrak{g}} \right] \Delta t \quad (1.19)$$

with the derivatives of the weighting function $\partial k^\mathfrak{g} / \partial \vartheta^\mathfrak{g} = -\gamma k / [\vartheta^{\max} - \vartheta^\mathfrak{g}]$ and the growth criterion $\partial \phi^\mathfrak{g} / \partial \vartheta^\mathfrak{g} = -\vartheta / \vartheta^{\mathfrak{g}2}$ introduced in equations (1.16) and (1.17). Within each iteration step, we iteratively update the unknown growth multiplier $\vartheta^\mathfrak{g} \leftarrow \vartheta^\mathfrak{g} - \mathbf{R}^\vartheta / \mathbf{K}^\vartheta$ until convergence is achieved, i.e., until the local growth update $\Delta \vartheta^\mathfrak{g} = -\mathbf{R}^\vartheta / \mathbf{K}^\vartheta$ reaches a user-defined tolerance.

To explore the interplay between growth and mechanics, we discretize the deformation map $\boldsymbol{\varphi}$ as nodal degree of freedom, and solve the mechanical equilibrium (1.7) globally at the node point level. To solve the quasi-static mechanical equilibrium, $\text{Div}(\mathbf{F} \cdot \mathbf{S}) = \mathbf{0}$, we cast it into its weak form, $\int_{\mathcal{B}_0} \nabla \delta \boldsymbol{\varphi} : [\mathbf{F} \cdot \mathbf{S}] \, dV = 0$, through multiplication with the test function $\delta \boldsymbol{\varphi}$ and integration over the domain of interest \mathcal{B}_0 . For the spatial discretization, we partition the domain of interest $\mathcal{B}_0 = \mathbf{U}_{e=1}^{\text{nel}} \mathcal{B}_0^e$ into n_{el} finite elements \mathcal{B}_0^e . Our goal is to determine the deformation state $\boldsymbol{\varphi}$ for a given load at time t . To approximate the test function $\delta \boldsymbol{\varphi} = \sum_{i=1}^{n_{\text{en}}} N^i \delta \boldsymbol{\varphi}_i$, the unknown deformation $\boldsymbol{\varphi} = \sum_{j=1}^{n_{\text{en}}} N^j \delta \boldsymbol{\varphi}_j$, and their gradients $\nabla \delta \boldsymbol{\varphi} = \sum_{i=1}^{n_{\text{en}}} \delta \boldsymbol{\varphi}_i \otimes \nabla N^i$ and $\nabla \boldsymbol{\varphi} = \sum_{j=1}^{n_{\text{en}}} \boldsymbol{\varphi}_j \otimes \nabla N^j$, we apply an isoparametric Bubnov-Galerkin based finite element interpolation, where N^i and N^j are the element shape functions and $i, j = 1, \dots, n_{\text{en}}$ are the element nodes. We now reformulate the weak form of the balance of linear momentum (1.7) with the help of these finite element approximations, introducing the discrete residual \mathbf{R}_I^φ in terms of the unknown nodal deformation $\boldsymbol{\varphi}_J$.

$$\mathbf{R}_I^\varphi = \mathbf{A} \int_{e=1}^{n_{\text{el}}} \nabla N_\varphi^i \cdot [\mathbf{F} \cdot \mathbf{S}] \, dV_e \doteq \mathbf{0} \quad (1.20)$$

Here, the operator \mathbf{A} symbolizes the assembly of all element residuals at the $j = 1, \dots, n_{\text{en}}$ element nodes to the global residual at the global node points $J = 1, \dots, n_{\text{el}}$. We evaluate the global discrete residual (1.20), once we have iteratively determined the growth multiplier $\vartheta^\mathfrak{g}$ for the given deformation state \mathbf{F} and the given history $\vartheta_n^\mathfrak{g}$ as described in the previous section. Then we successively determine the growth tensor $\mathbf{F}^\mathfrak{g}$ from equation (1.13), the elastic tensor $\mathbf{F}^e = \mathbf{F} \cdot \mathbf{F}^\mathfrak{g}^{-1}$ from equation (1.1), the elastic stress \mathbf{S}^e from equation (1.12), and lastly, the second Piola Kirchhoff stress \mathbf{S} from equation (1.11). Again, we suggest an incremental iterative Newton algorithm to solve the nonlinear residual equation for the unknown deformation (1.20). The consistent linearization of the

residual \mathbf{R}_I^φ with respect to the nodal vector of unknowns φ_J introduces the global stiffness matrix.

$$\begin{aligned} \mathbf{K}_{IJ}^\varphi &= \frac{\partial \mathbf{R}_I^\varphi}{\partial \varphi_J} = \mathbf{A} \int_{\mathcal{B}_e} \nabla N_\varphi^i \cdot \mathbf{S} \cdot \nabla N_\varphi^j \mathbf{I} \\ &\quad + [\nabla N_\varphi^i \cdot \mathbf{F}]^{\text{sym}} \cdot \mathbf{L} \cdot [\mathbf{F}^t \cdot \nabla N_\varphi^j]^{\text{sym}} dV_e \end{aligned} \quad (1.21)$$

The fourth order tensor \mathbf{L} denotes the Lagrangian constitutive moduli which, we can determine directly from the linearization of the Piola Kirchhoff stress \mathbf{S} with respect to the total right Cauchy Green tensor \mathbf{C} [71].

$$\mathbf{L} = 2 \frac{d\mathbf{S}}{d\mathbf{C}} = 2 \left. \frac{\partial \mathbf{S}}{\partial \mathbf{C}} \right|_{\mathbf{F}^g} + 2 \left[\frac{\partial \mathbf{S}}{\partial \mathbf{F}^g} : \frac{\partial \mathbf{F}^g}{\partial \vartheta^g} \right] \otimes \left. \frac{\partial \vartheta^g}{\partial \mathbf{C}} \right|_{\mathbf{F}} \quad (1.22)$$

The first term

$$2 \frac{\partial \mathbf{S}}{\partial \mathbf{C}} = [\mathbf{F}^{g-1} \otimes \overline{\mathbf{F}^{g-1}}] : \mathbf{L}^e : [\mathbf{F}^{g-t} \otimes \overline{\mathbf{F}^{g-t}}] \quad (1.23)$$

represents the pull back of the elastic moduli \mathbf{L}^e introduced in equation (1.12) onto the reference configuration. Here we have used the abbreviations $\{\bullet \otimes \circ\}_{ijkl} = \{\bullet\}_{ik} \{\circ\}_{jl}$ and $\{\bullet \otimes \circ\}_{ijkl} = \{\bullet\}_{il} \{\circ\}_{jk}$ for the non-standard fourth order products. The second term

$$\begin{aligned} \frac{\partial \mathbf{S}}{\partial \mathbf{F}^g} &= -[\mathbf{F}^{g-1} \otimes \overline{\mathbf{S}} + \mathbf{S} \otimes \overline{\mathbf{F}^{g-1}}] \\ &\quad - [\mathbf{F}^{g-1} \otimes \overline{\mathbf{F}^{g-1}}] : \frac{1}{2} \mathbf{L}^e : [\mathbf{F}^{g-t} \otimes \overline{\mathbf{C}^e} + \mathbf{C}^e \otimes \overline{\mathbf{F}^{g-t}}] \end{aligned} \quad (1.24)$$

consists of two terms that resemble a geometric and a material stiffness in nonlinear continuum mechanics. The third term

$$\frac{\partial \mathbf{F}^g}{\partial \vartheta^g} = \frac{1}{2\sqrt{\vartheta^g}} [\mathbf{I} - \mathbf{n}_0 \otimes \mathbf{n}_0] \quad (1.25)$$

and the fourth term

$$\begin{aligned} \frac{\partial \vartheta^g}{\partial \mathbf{C}} &= \frac{1}{\tau} \frac{1}{\vartheta^g} \left[\frac{\vartheta^{\text{max}} - \vartheta^g}{\vartheta^{\text{max}} - 1} \right]^\gamma \frac{1}{K^g} \Delta t \\ &\quad \frac{1}{2} \vartheta \mathbf{C}^{-1} - \frac{1}{2} \frac{J^2}{\vartheta} [\mathbf{C}^{-1} \cdot \mathbf{n}_0] \otimes [\mathbf{C}^{-1} \cdot \mathbf{n}_0] \end{aligned} \quad (1.26)$$

depend on the particular choice for the growth tensor \mathbf{F}^g in equation (1.13) and on the evolution equation for the growth multiplier ϑ^g in equation (1.15), respectively. For each global Newton iteration step, we iteratively update the current deformation state $\varphi \leftarrow \varphi - \mathbf{K}_{IJ}^{\varphi^{-1}} \cdot \mathbf{R}_I^\varphi$ until we achieve algorithmic convergence. Upon convergence, we store the corresponding growth multipliers ϑ^g at the integration point level. Table 1.1 summarizes the algorithmic treatment of skin growth at the integration point level.

Table 1.1: Algorithmic flowchart for strain-driven transversely isotropic area growth.

given \mathbf{F} and ϑ_n^g
initialize $\vartheta^g \leftarrow \vartheta_n^g$
local Newton iteration
check growth criterion $\phi^g = \vartheta^e - \vartheta^{\text{crit}} \geq 0$? (1.17)
calculate residual $\mathbf{R} = \vartheta^g - \vartheta_n^g - k^g \phi^g \Delta t$ (1.18)
calculate tangent $\mathbf{K} = \partial \mathbf{R} / \partial \vartheta^g$ (1.19)
update growth stretch $\vartheta^g \leftarrow \vartheta^g - \mathbf{R} / \mathbf{K}$
check convergence $\mathbf{R} \leq \text{tol}$?
calculate growth tensor \mathbf{F}^g (1.13)
calculate elastic tensor $\mathbf{F}^e = \mathbf{F} \cdot \mathbf{F}^g^{-1}$ (1.1)
calculate elastic right Cauchy Green tensor \mathbf{C}^e (1.4)
calculate elastic second Piola Kirchhoff stress \mathbf{S}^e (1.12)
calculate second Piola Kirchhoff stress \mathbf{S} (1.11)
calculate Lagrangian moduli \mathbf{L} (1.22)

1.2.3 Geometric modeling of skin growth

To simulate skin growth on an anatomically exact geometry, we create a finite element mesh on the basis of three-dimensional computer tomography images shown in Figure 1.5. Figure 1.6 summarizes the sequence of steps to generate our patient-specific geometric model. First, we identify the skin region by a distinct grey scale value in the computer tomography scans and extract point cloud data of its boundary. Figure 1.6, left, mimics the discrete nature of the extracted point cloud, with high point densities in the scanning plane and low point densities between the distinct planes. To smoothen the data and decreases the overall number of points, we homogenize the point

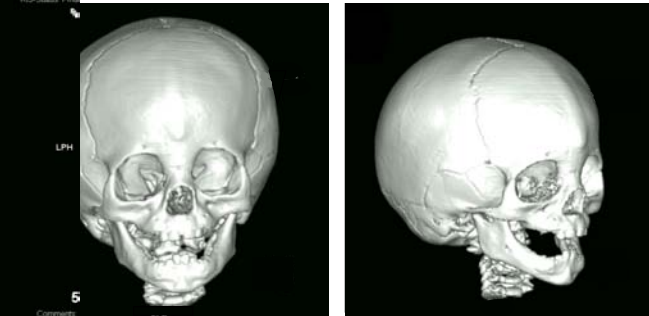


Figure 1.5: Three-dimensional computer tomography scans from the skull of a one-year old child. We create a patient-specific geometric model using discrete boundary points extracted from sliced image sections across the skull.

cloud using a median filter. Next, we create a triangular surface mesh from the smoothed point cloud by applying a ball-pivoting algorithm [23]. Ball-pivoting algorithms are particularly suited for surface reconstruction of large data sets. After placing an initial seed element, the ball-pivoting algorithm rotates a sphere over the edges of this element and sequentially creates new elements whenever the sphere touches three data points. However, since our data are based on plane-wise computer tomography scans, ball-pivoting algorithms typically fail to automatically create smooth surfaces. Unfortunately, other fully automated meshing strategies such as convex hull or shrink wrap algorithms are not suitable for non-convex geometries like the face, which possesses several non-convexities in the eye, nose, mouth, and ear regions [106]. Accordingly, we smoothen the triangular surface mesh semi-manually, as illustrated in Figure 1.6, middle.

From the smoothed surface mesh, we finally create a one-element thick volume mesh of the pediatric skull, discretized with 61,228 nodes, 183,684 degrees of freedom, and 30,889 tri-linear brick elements. As a first approximation, we assume that all eight integration points within each element possess the same skin plane normal \mathbf{n}_0 , corresponding to the normal from the initial surface mesh. We virtually implant three tissue expanders as shown in Figure 1.6, right, motivated by the tissue expansion case illustrated in Figure 1.1. First, we implant an expander in the scalp, discretized with 4,356 nodes, 13,068 degrees of freedom, and 2,088 tri-linear brick elements, covering an initial area of 50.4 cm^2 , shown in red. Second, we implant an expander in the cheek, discretized with 2,542 nodes, 7,626 degrees of freedom, and 1,200 tri-linear brick elements, covering an initial area of 29.3 cm^2 , shown in yellow. Third, we implant an expander in the forehead, discretized with 3,782 nodes, 11,346 degrees of freedom, and 1,800 tri-linear brick elements, covering an initial area of 48.5 cm^2 , shown in blue. To simulate tissue expansion, we fix all nodes and release only the expander degrees of freedom, which we then pressurize from underneath.

1.3 Results

We illustrate the impact of tissue expansion at three characteristic locations of the skull, in the scalp, the forehead, and the cheek. For the elastic model, we assume Lamé constants of $\lambda = 0.7141 \text{ MPa}$ and $\mu = 0.1785 \text{ MPa}$, which would correspond to a Poisson's ratio of $\nu = 0.4$ and a Young's modulus of $E = 0.5 \text{ MPa}$ in the linear regime [3, 188]. For the growth model, we assume a critical threshold of $\vartheta^{\text{crit}} = 1.1$, a maximum area growth of $\vartheta^{\text{max}} = 4.0$, a growth exponent of $\gamma = 3.0$, and an adaptation speed of $1/\tau = 12$. We gradually pressurize the tissue expanders, $0.0 < t \leq 0.125$, then hold the pressure constant to allow the tissue to grow, $0.125 < t \leq 0.75$, and finally remove the pressure to visualize the grown area, $0.75 < t \leq 1.0$.

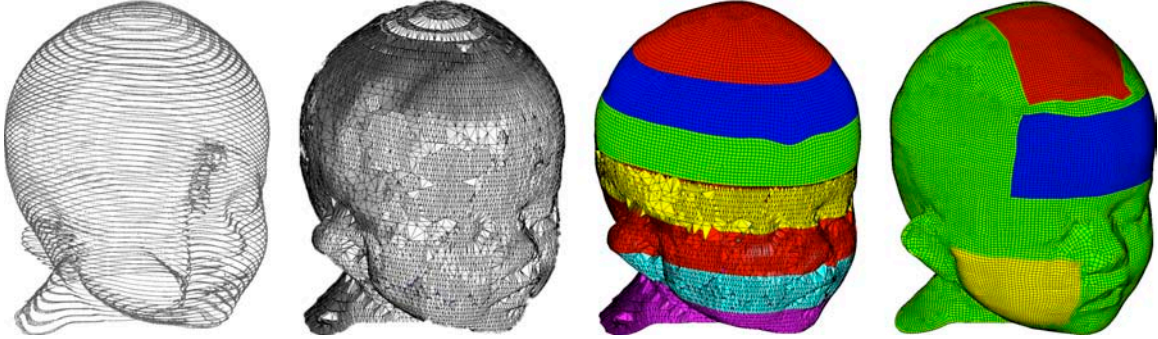


Figure 1.6: Mesh generation from clinical images. From the computer tomography scans, we extract discrete point cloud data (left), which we filter and mesh using a ball-pivoting algorithm. This generates a triangular surface mesh, which is further smoothed (middle) and turned into a final volume mesh (right). The final discretization of the skull consists of 61,228 nodes, 183,684 degrees of freedom, and 30,889 tri-linear brick elements. We virtually implant three tissue expanders, one in the scalp, discretized with 4,356 nodes, 13,068 degrees of freedom, and 2,088 brick elements (red), one in the cheek, discretized with 2,542 nodes, 7,626 degrees of freedom, and 1,200 brick elements (yellow), and one in the forehead, discretized with 3,782 nodes, 11,346 degrees of freedom, and 1,800 brick elements (blue).

1.3.1 Tissue expansion in the scalp

Figures 1.7, 1.8, and 1.9 illustrate the tissue expansion process in the scalp. Figure 1.7 displays the temporal evolution of the normalized total area, elastic area, and growth area upon subsequent expander inflation, constant pressure, and expander removal. Once the elastic area stretch reaches the critical threshold of $\vartheta^{\text{crit}} = 1.1$, slightly before the total pressure is applied, at $t = 0.125$, the tissue starts to grow. As the expander pressure is held constant, growth increases gradually causing the total area to increase as well. Then, at $t = 0.75$, the pressure is decreased to remove the expander. The elastic area retracts gradually, while the grown area remains constant. The vertical dashed lines correspond to the discrete time points, $t = 0.225$, $t = 0.300$, $t = 0.375$ and $t = 0.750$, displayed in Figure 1.8. Figure 1.8 illustrates the spatio-temporal evolution of area growth ϑ^{g} . Growth is first initiated at the center of the expander, where the elastic stretch is largest. As growth spreads throughout the entire expanded area, the initial area of 50.4 cm^2 increases gradually as the grown skin area increases from 70.07 cm^2 , to 84.25 cm^2 , to 95.73 cm^2 , and finally to 121.87 cm^2 , from left to right. Figure 1.9 summarizes the final outcome of the expansion in the scalp in terms of the remaining deformation upon expander removal. The elastic area strain of $0.95 \leq \vartheta^{\text{e}} \leq 1.05$ indicates an area change of $\pm 5\%$ giving rise to residual stresses, left. The area growth of $1.0 \leq \vartheta^{\text{g}} \leq 3.5$ shows that skin has more than doubled its initial area, right. This is in agreement with the final fractional

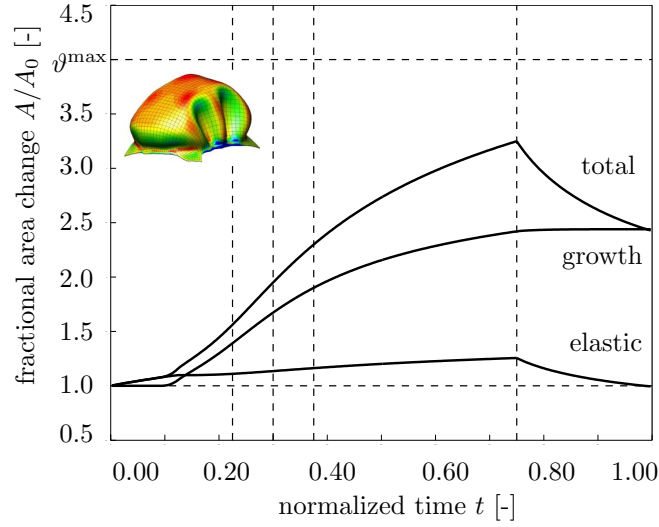


Figure 1.7: Tissue expansion in the scalp. Temporal evolution of normalized total area, elastic area, and growth area upon gradual expander inflation, $0.0 < t \leq 0.125$, constant pressure $0.125 < t \leq 0.75$, and deflation $0.75 < t \leq 1.0$. The final fractional area gain is 2.44, corresponding to 122.8 cm^2 . Vertical dashed lines correspond to the time points displayed in Figure 1.8.

area gain of 2.44, corresponding to an area growth in the scalp of 122.8 cm^2 .

1.3.2 Tissue expansion in the forehead

Figures 1.10, 1.11, and 1.12 summarize the tissue expansion process in the forehead. Figure 1.10 displays the temporal evolution of the normalized total area, elastic area, and growth area upon gradual expander inflation, constant pressure, and gradual expander removal. Similar to the expansion in the scalp, growth begins at stretches beyond the critical threshold level, then increases gradually upon constant pressure, and remains constant upon expander removal. Figure 1.11 illustrates the spatio-temporal evolution of area growth ϑ^g at four characteristic time points indicated through the vertical dashed lines in figure 1.10. The growth process starts in the center of the forehead and spreads out throughout the entire forehead area. As it does, the initial area of 48.5 cm^2 increases gradually as the grown skin area increases from 66.56 cm^2 , to 76.54 cm^2 , to 85.96 cm^2 , and finally to 116.55 cm^2 , from left to right. Figure 1.12 displays the remaining deformation upon expander removal. The final fractional area gain during forehead expansion is 2.44, corresponding to an area growth of 118.1 cm^2 .

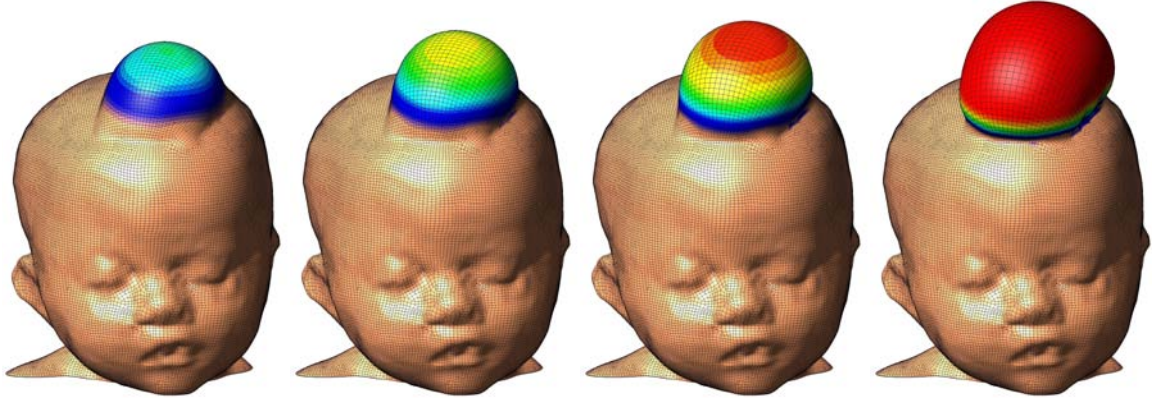


Figure 1.8: Tissue expansion in the scalp. Spatio-temporal evolution of area growth displayed at $t = 0.225$, $t = 0.300$, $t = 0.375$ and $t = 0.750$. The initial area of 50.4 cm^2 increases gradually as the grown skin area increases from 70.07 cm^2 , to 84.25 cm^2 , to 95.73 cm^2 , and finally to 121.87 cm^2 , from left to right.

1.3.3 Tissue expansion in the cheek

Figures 1.13, 1.14, and 1.15 document the tissue expansion process in the cheek. Figure 1.13 summarizes the temporal evolution of the normalized total area, elastic area, and growth area upon gradual expander inflation, constant pressure, and gradual expander removal. Again, the growth process is initiated once the stretches reach the critical threshold of $\vartheta^{\text{crit}} = 1.1$. Upon constant pressure, growth increases gradually. Upon pressure removal, growth remains constant displaying the irreversible nature of the growth process. Figure 1.14 illustrates the spatio-temporal evolution of area growth ϑ^{g} in the cheek. Again, growth begins in center of cheek, where the elastic area stretch is largest. As the growth process spreads out throughout the entire cheek area, the initial area of 29.3 cm^2 increases gradually as the grown skin area increases from 42.74 cm^2 , to 52.03 cm^2 , to 59.39 cm^2 , and finally to 76.86 cm^2 , from left to right. Figure 1.15 summarizes the outcome of the expansion in the cheek with a final fractional area gain of 2.64, corresponding to an area growth of 77.4 cm^2 .

1.4 Discussion

Tissue expansion is one of the basic treatment modalities in modern reconstructive surgery. Inducing controlled tissue growth through well-defined overstretch, it creates skin that matches the color, texture, hair bearance, and thickness of the surrounding healthy skin, while minimizing scars and risk of rejection [83]. Despite its widespread use, the choice of the appropriate tissue expander is almost

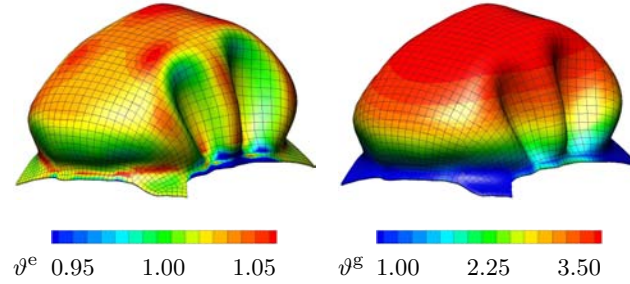


Figure 1.9: Tissue expansion in the scalp. Remaining deformation upon expander removal. The elastic area strain of $0.95 \leq \vartheta^e \leq 1.05$ indicates an area change of $\pm 5\%$ giving rise to residual stresses (left). The area growth of $1.0 \leq \vartheta^g \leq 3.5$ shows that skin has more than doubled its initial area (right). The final fractional area gain is 2.44, corresponding to 122.8 cm^2 .

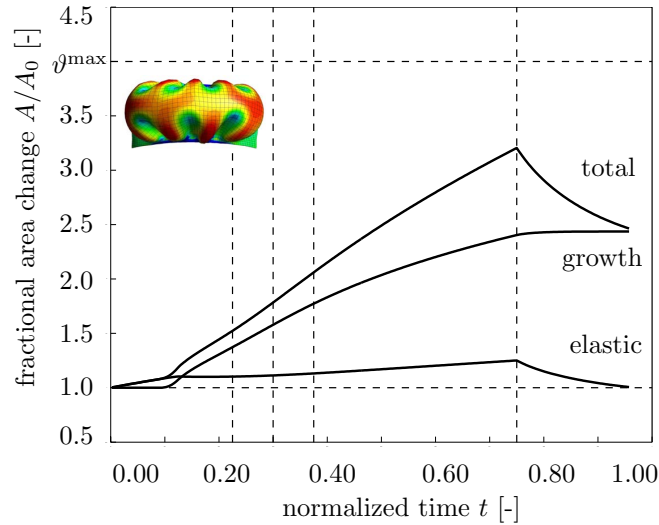


Figure 1.10: Tissue expansion in the forehead. Temporal evolution of normalized total area, elastic area, and growth area upon gradual expander inflation, $0.0 < t \leq 0.125$, constant pressure $0.125 < t \leq 0.75$, and deflation $0.75 < t \leq 1.0$. The final fractional area gain is 2.44, corresponding to 118.1 cm^2 . Vertical dashed lines correspond to the time points displayed in Figure 1.11.

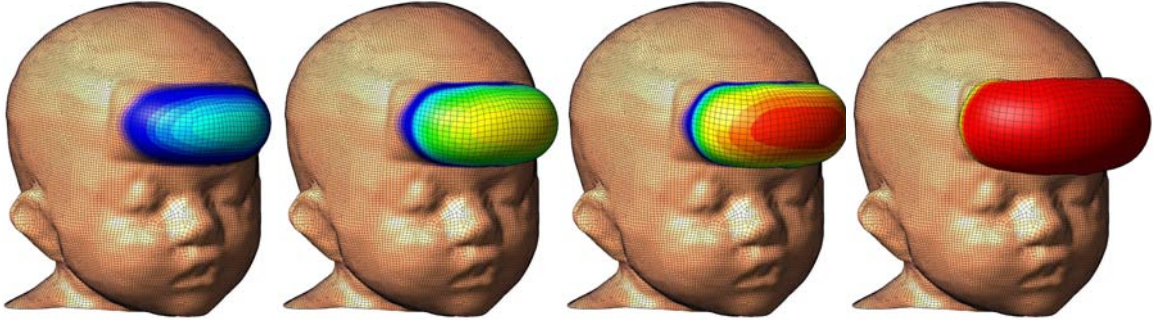


Figure 1.11: Tissue expansion in the forehead. Spatio-temporal evolution of area growth displayed at $t = 0.225$, $t = 0.300$, $t = 0.375$ and $t = 0.750$. The initial area of 48.5 cm^2 increases gradually as the grown skin area increases from 66.56 cm^2 , to 76.54 cm^2 , to 85.96 cm^2 , and finally to 116.55 cm^2 , from left to right.

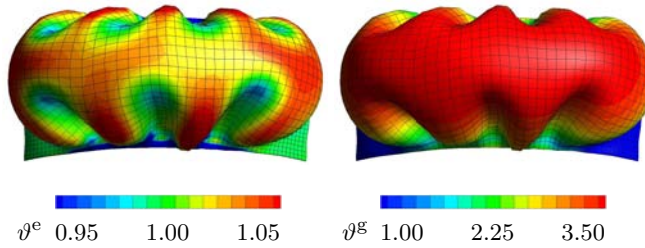


Figure 1.12: Tissue expansion in the forehead. Remaining deformation upon expander removal. The elastic area strain of $0.95 \leq \vartheta^e \leq 1.05$ indicates an area change of $\pm 5\%$ giving rise to residual stresses (left). The area growth of $1.0 \leq \vartheta^g \leq 3.5$ shows that skin has more than doubled its initial area (right). The final fractional area gain is 2.44, corresponding to 118.1 cm^2 .

exclusively based on the surgeon's personal preference, and the discrepancy between recommended shapes, sizes, and volumes remains enormous [137]. The current gold standard for expander selection is to predict tissue growth by calculating the difference between the inflated and non-inflated expander surface [58, 189]. From an engineering point of view, it is quite intuitive, that this purely kinematic approach severely overestimates the net gain in surface area [212]. With a discrepancy of up to a factor four, these models assume that the entire deformation can be attributed to irreversible growth, completely neglecting the elastic deformation, which is reversible upon expander removal [137]. In an attempt to account for this error, empirical correction factors of 6.00, 3.75, and 4.50 have been proposed for circular, rectangular, and crescent-shaped expanders [212]. This demonstrates the vital need to rationalize criteria for a standardized device selection.

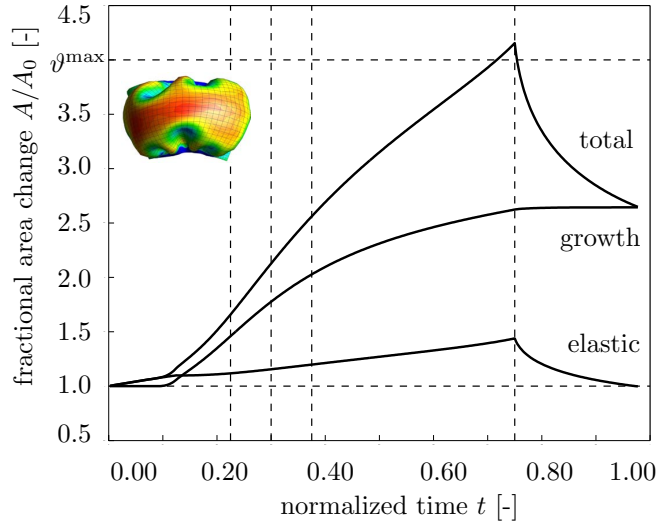


Figure 1.13: Tissue expansion in the cheek. Temporal evolution of normalized total area, elastic area, and growth area upon gradual expander inflation, $0.0 < t \leq 0.125$, constant pressure $0.125 < t \leq 0.75$, and deflation $0.75 < t \leq 1.0$. The final fractional area gain is 2.64, corresponding to 77.4 cm^2 . Vertical dashed lines correspond to the time points displayed in Figure 1.14.

Motivated by a first study on axisymmetric skin growth [193], we have recently established a prototype model for growing membranes to simulate tissue expansion in a general three-dimensional setting [36]. We have applied our model to quantitatively compare four commonly available tissue expander geometries, round, square, rectangular, and crescent [37], however, only on initially flat geometries. Here, for the first time, we demonstrate the potential of the model during tissue expansion in pediatric forehead reconstruction using a real patient-specific model. To embed the solution into a nonlinear finite element environment, we discretize the governing equations for in-plane area growth in time and space. To solve the nonlinear set of equations, we apply an incremental iterative Newton-Raphson solution strategy based on the consistent algorithmic linearization. The resulting algorithm is remarkably efficient, stable, and robust. It is capable of predicting tissue expander inflation, tissue growth, and expander deflation at different locations of a human skull within the order of minutes on a standard laptop computer. Because of its geometric flexibility, our general algorithm could also be adapted to predict tissue expansion in the trunk [10] or in the upper and lower extremities [81].

Although the proposed model for skin growth represents a significant advancement over the axisymmetric growth model previously proposed [193], we would like to point out that some limitations remain. First, motivated by experimental observations, which report normal cell differentiation upon tissue expansion [218], we have assumed that the material microstructure remains unaffected by the growth process, $\mathbf{F}^g = \sqrt{\vartheta^g} \mathbf{I} + [1 - \sqrt{\vartheta^g}] \mathbf{n}_0 \otimes \mathbf{n}_0$. Here, for the sake of simplicity, we have

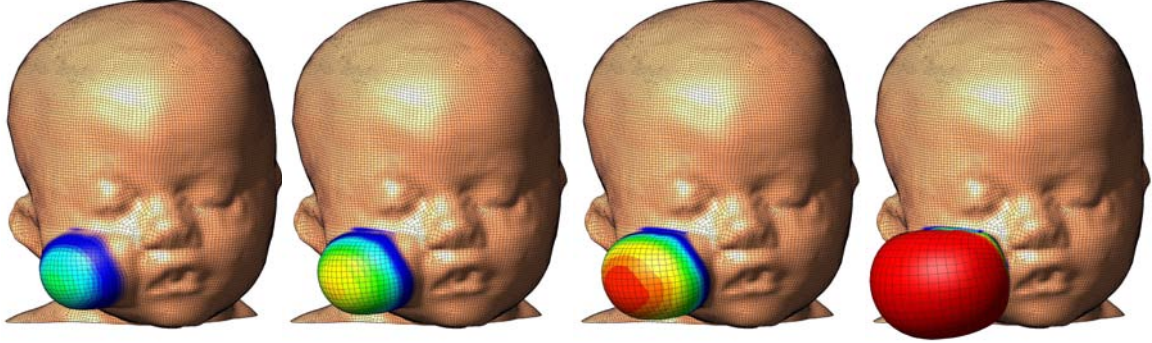


Figure 1.14: Tissue expansion in the cheek. Spatio-temporal evolution of area growth displayed at $t = 0.225$, $t = 0.300$, $t = 0.375$ and $t = 0.750$. The initial area of 29.3 cm^2 increases gradually as the grown skin area increases from 42.74 cm^2 , to 52.03 cm^2 , to 59.39 cm^2 , and finally to 76.86 cm^2 , from left to right.

modeled this microstructure as isotropic and elastic. We have recently shown that it is straightforward to combine our growth model with in-plane anisotropy, introduced through pronounced stiffness along Langer's lines [37, 116]. It might also be interesting to elaborate out-of-plane anisotropy and model the different skin layers individually [145]. We have demonstrated how to model the growth process itself as anisotropic as well [71]. This could imply growth ϑ^{\parallel} exclusively along specific microstructural directions such as Langer's lines, $\mathbf{F}^g = \mathbf{I} + [\vartheta^{\parallel} - 1]\boldsymbol{\nu}_0^{\parallel} \otimes \boldsymbol{\nu}_0^{\parallel}$, or major in-plane growth ϑ^{\parallel} along Langer's lines combined with minor in-plane growth ϑ^{\perp} orthogonal to Langer's lines, $\mathbf{F}^g = \vartheta^{\parallel} \boldsymbol{\nu}_0^{\parallel} \otimes \boldsymbol{\nu}_0^{\parallel} + \vartheta^{\perp} \boldsymbol{\nu}_0^{\perp} \otimes \boldsymbol{\nu}_0^{\perp} + \mathbf{n}_0 \otimes \mathbf{n}_0$. Similarly, we could even introduce a progressive reorientation of the collagen network to allow for the material to align with the maximum principal strains [119, 150]. Ideally, the growth law would be tied to the underlying mechanobiology [55]. Comparative tissue histology of grown and ungrown tissue samples could help to identify the mechanisms that trigger skin growth to validate or, if necessary, refine our evolution equation (1.13) for the growth tensor.

Second, for the sake of simplicity, our finite element mesh consists of one single brick element with two integration points across the skin thickness. We have previously studied the sensitivity of growth with respect to thickness refinement using a higher resolution across the thickness [36, 37]. However, our results were rather insensitive to mesh refinement. This insensitivity might be explained by the fact that, upon expander inflation, the skin is almost in a pure membrane state. During deflation, however, we observe buckling associated with strain gradients across the skin thickness, which might play a critical role in the development of residual stresses. To explore these residual stresses further, we are currently refining our model utilizing a shell kinematics [175] with a higher resolution across the thickness direction. This will also allow us to simulate the individual skin layers [130, 191] and

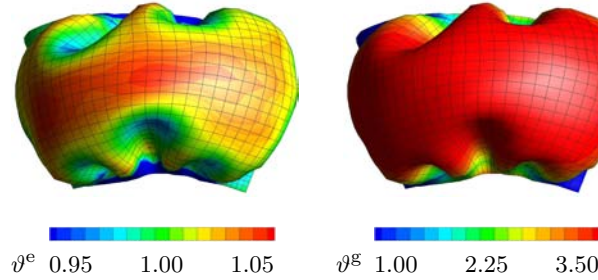


Figure 1.15: Tissue expansion in the cheek. Remaining deformation upon expander removal. The elastic area strain of $0.95 \leq \vartheta^e \leq 1.05$ indicates an area change of $\pm 5\%$ giving rise to residual stresses (left). The area growth of $1.0 \leq \vartheta^g \leq 3.5$ shows that skin has more than doubled its initial area (right). The final fractional area gain is 2.64, corresponding to 77.4 cm^2 .

their interaction during the expansion process, which we believe to be a major source of residual stress in real tissue expansion cases [149, 220].

Third, for the sake of simplicity, we have modeled tissue expansion only implicitly through controlling the applied pressure. In real tissue expansion, the external control parameter is the expander volume [137]. This implies that our virtual tissue expansion displays creep under constant loading, while clinical tissue expansion might rather display relaxation under constant deformation [37], similar to our parameter study in Figure 1.4.

Fourth, here, we have assumed that the expander is connected tightly to the expanded tissue, neglecting effects of interface sliding and shear [193]. This seems to be a reasonable first assumption though, since most current expanders have well-designed textures to promote mild tissue in-growth, primarily to prevent expander migration [21]. To address these potential limitations, we are currently refining the elastic model, the growth model, and the boundary conditions, to render our future simulations more realistic.

Last, while our computational model seems well suited to provide qualitative guidelines and trends, at its present state, it is not recommended for quantitative statements. We will need to perform acute and chronic in vitro and in vivo experiments to truly calibrate the underlying material parameters, to potentially refine and fully validate our model, to eventually make it applicable for clinical practice. Nevertheless, we believe that using the equations on nonlinear continuum mechanics represents a significant advancement over the current gold standard to predict tissue growth exclusively in terms of kinematic quantities [189, 212].

Conclusion

We have presented a novel computational model to predict the chronic adaptation of thin biological membranes when stretched beyond their physiological limit. Here, to illustrate the features of this model, we have demonstrated its performance during tissue expansion in pediatric forehead reconstruction. We have quantified reversibly elastic and irreversibly grown area changes in response to skin expansion in the scalp, the forehead, and the cheek of a one-year-old child. In general, our generic computational model is applicable to arbitrary skin geometries, and has the potential to predict area gain in skin expansion during various common procedures in reconstructive surgery. A comprehensive understanding of the gradually evolving stress and strain fields in growing skin may help the surgeon to prevent tissue damage and optimize clinical process parameters such as expander geometry, expander size, expander placement, and inflation timing. Ultimately, through inverse modeling, computational tools like ours have the potential to rationalize these parameters to create skin flaps of desired size and shape. Overall, we believe that predictive computational modeling might open new avenues in reconstructive surgery and enhance treatment for patients with birth defects, burn injuries, or breast tumor removal.

Acknowledgements

This work was supported by the Claudio X. Gonzalez Fellowship CVU 358668 and the Stanford Graduate Fellowship to Adrián Buganza Tepole and by the National Science Foundation CAREER award CMMI-0952021 and the National Institutes of Health Grant U54 GM072970 to Ellen Kuhl.

Chapter 2

Tissue expansion in Eulerian formulation

Abstract

Skin displays an impressive functional plasticity, which allows it to adapt gradually to environmental changes. Tissue expansion takes advantage of this adaptation, and induces a controlled in situ skin growth for defect correction in plastic and reconstructive surgery. Stretches beyond the skin's physiological limit invoke several mechanotransduction pathways, which increase mitotic activity and collagen synthesis, ultimately resulting in a net gain in skin surface area. However, the interplay between mechanics and biology during tissue expansion remains unquantified. Here we present a continuum model for skin growth that summarizes the underlying mechanotransduction pathways collectively in a single phenomenological variable, the strain-driven area growth. We illustrate the governing equations for growing biological membranes, and demonstrate their computational solution within a nonlinear finite element setting. In displacement-controlled equi-biaxial extension tests, the model accurately predicts the experimentally observed histological, mechanical, and structural features of growing skin, both qualitatively and quantitatively. Acute and chronic elastic uniaxial stretches are 25% and 10%, compared to 36% and 10% reported in the literature. Acute and chronic thickness changes are -28% and -12%, compared to -22% and -7% reported in the literature. Chronic fractional weight gain is 3.3, compared to 2.7 for wet weight and 3.3 for dry weight reported in the literature. In two clinical cases of skin expansion in pediatric forehead reconstruction, the model captures the clinically observed mechanical and structural responses, both acutely and chronically. Our results demonstrate that the field theories of continuum mechanics can reliably predict the mechanical manipulation of thin biological membranes by controlling their mechanotransduction pathways through mechanical overstretch. We anticipate that the proposed skin growth model can be generalized to arbitrary biological membranes, and that it can serve as a valuable tool to virtually manipulate living tissues, simply by means of changes in the mechanical environment.

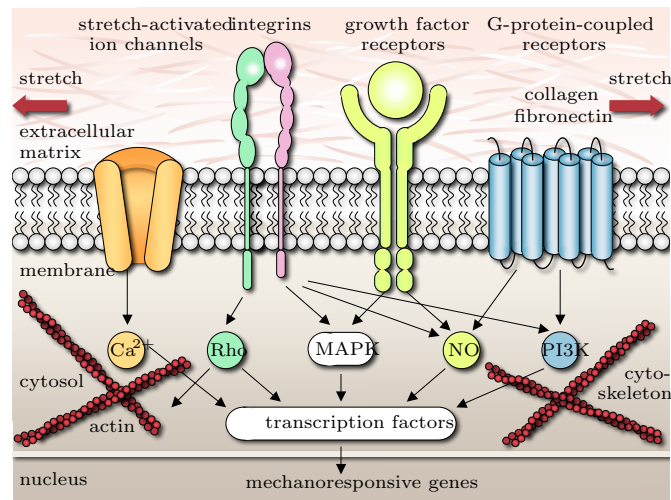


Figure 2.1: Mechanotransduction of growing skin. Transmembrane mechanosensors in the form of stretch-activated ion channels, integrins, growth factor receptors, and G-protein-coupled receptors translate extracellular signals into intracellular events, which activate a cascade of interconnected signaling pathways. Biomechanical and biochemical signals converge in the activation of transcription factors, activating gene expression. Mechanotransduction triggers increased mitotic activity and increased collagen synthesis, resulting in an increase in skin surface area to restore the homeostatic equilibrium state [94, 138].

2.1 Motivation

Human skin is a remarkable organ that can be stretched to manyfold its original size, while remaining phenotypically similar to its initial state, without any reported malignant transformation [22, 55]. To enable this incredible expansion, skin is a highly specialized mechanoresponsive interface, characterized through a network of interrelated cascades involving extracellular, membrane, cytosolic, cytoskeletal, and nuclear mechanisms [191]. When skin is stretched beyond its physiological limit, these mechanisms act in concert to restore the homeostatic equilibrium state. In this regulatory process, transmembrane mechanosensors in the form of stretch-activated ion channels, integrins, growth factor receptors, and G-protein-coupled receptors play a key role in translating extracellular events into intracellular signals [94, 138], see Figure 2.1.

Stretch-activated ion channels open in response to elevated membrane strains, allowing positively charged calcium ions (Ca^{2+}) and other cations to enter the cell. Changes in the intracellular calcium concentration are known to regulate intracellular signaling and cytoskeletal remodeling [191]. Integrins are receptors that mediate attachment between a cell and the extracellular matrix [192]. They play a central role in force transmis-

sion across the cell membrane, triggering targets such as nitric oxide (NO) signaling, mitogen-associated protein kinases (MAPK), Rho GTPases, and phosphoinositol-3-kinase (PI3K). Growth factor receptors bind to growth factors outside the cell, thereby turning on several receptor mediated pathways inside the cell, such as nitric oxide (NO) signaling and mitogen-associated protein kinases (MAPK) [94]. Mitogen-associated protein kinase signaling pathways convey information to effectors, coordinate incoming information from other signaling cascades, amplify signals, and initiate a variety of response patterns. G protein-coupled receptors are seven-transmembrane proteins, which can potentially be activated by mechanical stretch outside the cell to initiate mechanotransduction pathways inside the cell through second messengers such as nitric oxide (NO) signaling and phosphoinositol-3-kinase (PI3K). Last, intracellular strain can induce conformational changes in the cytoskeleton itself. These changes may affect the binding affinities to specific molecules and thereby activate additional signaling pathways [124].

In summary, mechanical activation initiates multiple signaling pathways, which can have a substantial overlap and crosstalk. However, since mechanically-induced signaling pathways may be shared with classical receptor-mediated pathways, they are typically difficult to study in isolation. It is clear, however, that all these signaling pathways converge to activate transcription factors, which stimulate gene expression and other nuclear events [138]. Overall, the underlying principle is that stretch invokes a cascade of events that trigger increased mitotic activity and increased collagen synthesis, which ultimately result in increased skin surface area to restore the homeostatic equilibrium state [203].

Taking advantage of mechanotransduction is a powerful approach to endogenously engineer new skin. Since it was first introduced in the mid 1950s [154], the controlled mechanical manipulation of skin has opened a whole new frontier in reconstructive surgery. Today tissue expansion is widely used to repair birth defects [11], correct burn injuries [9], and reconstruct breasts after tumor removal [173]. It is the ideal strategy to grow skin that matches the color, texture, hair bearance, and thickness of the surrounding healthy skin, while minimizing scars and risk of rejection [181].

Tissue expansion is an iterative procedure of controlled overstretch, progressive skin growth, and gradual restoration of the homeostatic equilibrium state, repeated in several weekly intervals [81]. To grow skin in a desired location, the surgeon dissects a subcutaneous pocket between the dermis and the hypodermis [83], in which he places the expander. The expander is successively filled with saline solution by a remote injection port, see Figure 2.2. By visual inspection of skin color, capillary refill, and palpation of the expanded skin, the surgeon heuristically determines the amount of filling [181]. Once enough new skin is produced, typically after a period of multiple weeks, the device is removed, and the new skin is used to repair the adjacent defect zone. Although tissue expansion is a common surgical procedure today, there are no scientific guidelines for optimal device selection. Accordingly, the appropriate choice of expander shape, expander size, expander location, filling volume, and filling timing remains almost exclusively based on the surgeon's experience and

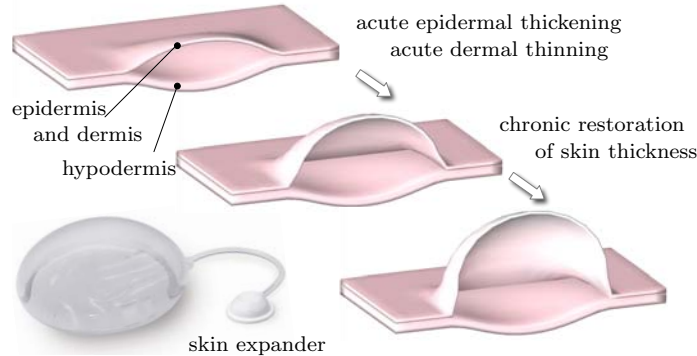


Figure 2.2: Biomechanics of growing skin. At biological equilibrium, the skin is in a homeostatic state of resting tension. To grow skin for defect repair, a tissue expander is placed in a subcutaneous pocket underneath the epidermis and the dermis, above the hypodermis. When the expander is inflated, the skin is stretched, associated with an acute dermal thinning attributed to the Poisson effect. Stretches beyond a critical level trigger a series of signaling pathways leading to the creation of new skin. Skin restores its homeostatic state, associated with the chronic restoration of the original thickness. Upon expander removal, elastic deformations retract and inelastic deformations remain.

personal preference [137].

The first quantitative model for growing skin was proposed only a few years ago, and has unfortunately not received a lot of attention to date [193]. Motivated by this first study on axisymmetric skin growth, conceptually similar to an axisymmetric model for growing cell walls [78], we have recently established a prototype model for growing biological membranes to predict skin growth in a general three-dimensional setting [36]. The model is based on the continuum framework of finite growth [183], originally developed for the isotropic volumetric growth of biological solids [4, 62, 139]. Its key kinematic feature is the multiplicative decomposition of the deformation gradient into a reversible elastic part and an irreversible growth part [67, 140], a concept that was adopted from finite plasticity [125]. Over the past decade, continuum growth theories have been rapidly developed and intensely refined to characterize isotropic [47, 79, 118], transversely isotropic [176, 197], orthotropic [72, 198], and generally anisotropic [5, 150] growth phenomena, both compressibly [148] and incompressibly [91, 186].

Recent trends focus on the computational modeling of finite growth [6, 87], typically by introducing the growth tensor as an internal variable within a nonlinear finite element framework [71, 110], a strategy that we also adopt here. To predict the biomechanics and mechanobiology of growing skin and their impact on stress, strain, and area gain, we adopt a transversely isotropic growth model [36, 37], in which all cellular and molecular mechanisms are collectively summarized in a single phenomenological internal variable, the in-plane area growth. Here, in contrast to our previous model formulated in the material frame of reference [224], we introduce a spatial formulation, which lends itself to a computationally elegant and highly efficient algorithm. To simulate heterogeneous

growth phenomena on anatomically realistic geometries, we integrate the growth model into a multi-purpose nonlinear finite element program [205]. We illustrate its features by means of the simple model problem of equi-biaxial extension and through two clinical cases of skin expansion in pediatric forehead reconstruction.

2.2 Methods

2.2.1 Continuum model of growing skin

To accurately represent the finite deformations during skin expansion, we adopt the kinematics of finite growth, and introduce the deformation map φ , which, at any given time t , maps the material placement \mathbf{X} of a physical particle onto its spatial placement $\mathbf{x} = \varphi(\mathbf{X}, t)$. We then introduce the multiplicative decomposition of the deformation gradient [183],

$$\mathbf{F} = \nabla_{\mathbf{X}} \varphi = \mathbf{F}^e \cdot \mathbf{F}^g \quad (2.1)$$

into a reversible elastic part \mathbf{F}^e and an irreversible growth part \mathbf{F}^g , in agreement with experimental findings [212]. Here, $\nabla\{\circ\} = \partial_{\mathbf{X}}\{\circ\}|_t$ denotes the gradient of a field $\{\circ\}(\mathbf{X}, t)$ with respect to the material placement \mathbf{X} at fixed time t . Its Jacobian defines the overall change in tissue volume,

$$J = \det(\mathbf{F}) = J^e J^g \quad (2.2)$$

which we can equivalently decompose into a reversibly elastic volume change $J^e = \det(\mathbf{F}^e)$ and an irreversibly grown volume change $J^g = \det(\mathbf{F}^g)$. Skin is a composite material consisting of a 0.1-1.0 mm thick, waterproof, protective outer layer, the epidermis, and a 1.0-4.0 mm thick, load bearing inner layer, the dermis [191], which we idealize jointly as a single layer. We characterize its area stretch through Nanson's formula

$$\vartheta = \|\text{cof}(\mathbf{F}) \cdot \mathbf{n}_0\| = \vartheta^e \vartheta^g \quad (2.3)$$

in terms of the skin plane normal \mathbf{n}_0 in the undeformed reference configuration, where $\text{cof}(\circ) = \det(\circ)(\circ)^{-t}$ denotes the cofactor of a second order tensor (\circ) . The area stretch obeys the multiplicative decomposition into a reversibly elastic area stretch ϑ^e and an irreversibly grown area stretch $\vartheta^g = \|\text{cof}(\mathbf{F}^g) \cdot \mathbf{n}_0\|$. To model stretch-induced skin growth, we collectively summarize the effects of mechanotransduction in a single scalar-valued variable ϑ^g , which characterizes the evolution of the in-plane area growth, while the response in the thickness direction \mathbf{n}_0 is assumed to be purely elastic [22]. Accordingly, we can express the growth tensor \mathbf{F}^g in the following simple format.

$$\mathbf{F}^g = \sqrt{\vartheta^g} \mathbf{I} + [1 - \sqrt{\vartheta^g}] \mathbf{n}_0 \otimes \mathbf{n}_0 \quad (2.4)$$

Since the material is not assumed to grow in the thickness direction \mathbf{n}_0 [181, 210], its area growth is identical to its volume growth, i.e., $\vartheta^g = \det(\mathbf{F}^g) = J^g$. Using the simple rank-one update structure of \mathbf{F}^g , we can apply the Sherman-Morrison formula to invert the growth tensor explicitly,

$$\mathbf{F}^{g-1} = \frac{1}{\sqrt{\vartheta^g}} \mathbf{I} + \left[1 - \frac{1}{\sqrt{\vartheta^g}} \right] \mathbf{n}_0 \otimes \mathbf{n}_0 \quad (2.5)$$

and obtain an explicit representation of the elastic tensor \mathbf{F}^e ,

$$\mathbf{F}^e = \frac{1}{\sqrt{\vartheta^g}} \mathbf{F} + \left[1 - \frac{1}{\sqrt{\vartheta^g}} \right] \mathbf{n} \otimes \mathbf{n}_0 \quad (2.6)$$

in terms of the spatial normal $\mathbf{n} = \mathbf{F} \cdot \mathbf{n}_0$. From the push forward of the contravariant material and intermediate metric tensors \mathbf{G}^{-1} and \mathbf{G}^{g-1} , we obtain the left Cauchy Green tensor $\mathbf{b} = \mathbf{F} \cdot \mathbf{G}^{-1} \cdot \mathbf{F}^t$ and its counterpart \mathbf{b}^e in the deformed, current configuration.

$$\mathbf{b}^e = \mathbf{F}^e \cdot \mathbf{G}^{g-1} \cdot \mathbf{F}^{et} = \frac{1}{\vartheta^g} \mathbf{b} + \left[1 - \frac{1}{\vartheta^g} \right] \mathbf{n} \otimes \mathbf{n} \quad (2.7)$$

To focus on the impact of growth, we assume skin to behave isotropically elastic within the *in vivo* loading range of interest. Accordingly, we introduce the following Helmholtz free energy

$$\psi = \frac{1}{2} \lambda \ln^2(J^e) + \frac{1}{2} \mu [\mathbf{g} : \mathbf{b}^e - 3 - 2 \ln(J^e)] \quad (2.8)$$

to evaluate the standard dissipation inequality, which defines the Kirchhoff stress $\boldsymbol{\tau}$ as thermodynamically conjugate to covariant spatial metric \mathbf{g} .

$$\boldsymbol{\tau} = 2 \frac{\partial \psi}{\partial \mathbf{g}} = [\lambda \ln(J^e) - \mu] \mathbf{g}^{-1} + \mu \mathbf{b}^e \quad (2.9)$$

This implies that the newly created skin will have the same microstructure, density, and stiffness, as the original, native tissue [22, 36]. We model skin growth as a strain-driven process [83], and introduce the following evolution equation for the area growth,

$$\dot{\vartheta}^g = k^g(\vartheta^g) \phi^g(\vartheta^e) \quad (2.10)$$

in which $k^g(\vartheta^g)$ is a weighting function and $\phi^g(\vartheta^e)$ is a growth criterion similar to a yield function in the theory of plasticity. For the weighting function, we adopt a well-established functional form [139], which we rephrase here in a strain-driven format [71, 72], to control unbounded growth.

$$k^g = \frac{1}{\tau} \left[\frac{\vartheta^{\max} - \vartheta^g}{\vartheta^{\max} - 1} \right]^\gamma \quad (2.11)$$

The adaptation speed τ and the shape parameter for the adaptation curve γ control the speed of adaptation, whereas the maximum area growth ϑ^{\max} defines the biological equilibrium state [87, 139]. For the growth criterion, we assume that growth is driven by the elastic area stretch ϑ^e ,

$$\phi^g = \langle \vartheta^e - \vartheta^{\text{crit}} \rangle = \langle \vartheta / \vartheta^g - \vartheta^{\text{crit}} \rangle \quad (2.12)$$

and that it is activated only if the elastic area stretch exceeds a critical physiological limit ϑ^{crit} , where $\langle \circ \rangle$ denote the Macaulay brackets.

2.2.2 Computational model of growing skin

To solve the nonlinear finite element equations of stretch-induced skin growth, we implement the growth model in a custom-designed version of the multipurpose nonlinear finite element program FEAP [205]. To characterize the growth process at each instant in time, we introduce the area growth ϑ^g as an internal variable, and solve the biological equilibrium equation (2.10) locally at the integration point level. At each discrete time step t , we determine the current area growth ϑ^g for a given current deformation state \mathbf{F} and a given area growth ϑ_n^g from the previous time step t_n . Accordingly, we introduce the following finite difference approximation for the material time derivative of the area growth,

$$\dot{\vartheta}^g = [\vartheta^g - \vartheta_n^g] / \Delta t \quad (2.13)$$

where $\Delta t = t - t_n$ denotes the current time increment. In the spirit of implicit time stepping schemes, we now reformulate the evolution equation (2.10) with the help of equation (2.13), introducing the discrete residual \mathbf{R}^ϑ in terms of the unknown area growth ϑ^g .

$$\mathbf{R}^\vartheta = \vartheta^g - \vartheta_n^g - k^g \phi^g \Delta t \doteq 0 \quad (2.14)$$

We solve this nonlinear equation using a local Newton iteration. Within each iteration step, we calculate the linearization of the residual \mathbf{R}^ϑ with respect to the area growth ϑ^g ,

$$\mathbf{K}^\vartheta = \frac{\partial \mathbf{R}^\vartheta}{\partial \vartheta^g} = 1 - \left[\frac{\partial k^g}{\partial \vartheta^g} \phi^g + k^g \frac{\partial \phi^g}{\partial \vartheta^g} \right] \Delta t \quad (2.15)$$

in terms of the linearizations of the weighting function $\partial k^g / \partial \vartheta^g = -\gamma k^g / [\vartheta^{\max} - \vartheta^g]$ and the growth criterion $\partial \phi^g / \partial \vartheta^g = -\vartheta / \vartheta^{g2}$ introduced in equations (2.11) and (2.12). We update the unknown area growth iteratively,

$$\vartheta^g \leftarrow \vartheta^g - \mathbf{R}^\vartheta / \mathbf{K}^\vartheta \quad (2.16)$$

until we achieve convergence, i.e., until the absolute value of the local growth update $\Delta \vartheta^g = -\mathbf{R}^\vartheta / \mathbf{K}^\vartheta$ is below a user-defined threshold value. Once we have iteratively determined the current area growth ϑ^g , we can successively determine the growth tensor \mathbf{F}^g from equation (2.4), the elastic tensor

$\mathbf{F}^e = \mathbf{F} \cdot \mathbf{F}^g^{-1}$ from equation (2.6), the Kirchhoff stress $\boldsymbol{\tau}$ from equation (2.9), and, finally, the fourth order tensor \mathbf{e} of the Eulerian constitutive moduli.

$$\mathbf{e} = 2 \frac{d\boldsymbol{\tau}}{d\mathbf{g}} = \mathbf{e}^e + \mathbf{e}^g = 2 \left. \frac{\partial \boldsymbol{\tau}}{\partial \mathbf{g}} \right|_{\mathbf{F}^g} + \frac{\partial \boldsymbol{\tau}}{\partial \vartheta^g} \otimes 2 \left. \frac{\partial \vartheta^g}{\partial \mathbf{g}} \right|_{\mathbf{F}} \quad (2.17)$$

The first term, the partial derivative of the Kirchhoff stress $\boldsymbol{\tau}$ with respect to the covariant spatial metric \mathbf{g} , defines elastic constitutive moduli $\mathbf{e}^e = 2 \partial \boldsymbol{\tau} / \partial \mathbf{g}$,

$$2 \frac{\partial \boldsymbol{\tau}}{\partial \mathbf{g}} = \lambda \mathbf{g}^{-1} \otimes \mathbf{g}^{-1} + [\mu - \lambda \ln(J^e)] [\mathbf{g}^{-1} \bar{\otimes} \mathbf{g}^{-1} + \mathbf{g}^{-1} \underline{\otimes} \mathbf{g}^{-1}] \quad (2.18)$$

where we have used the common abbreviations, $\{\bullet \bar{\otimes} \circ\}_{ijkl} = \{\bullet\}_{ik} \{\circ\}_{jl}$ and $\{\bullet \underline{\otimes} \circ\}_{ijkl} = \{\bullet\}_{il} \{\circ\}_{jk}$, for the non-standard fourth order products. The second term

$$\frac{\partial \boldsymbol{\tau}}{\partial \vartheta^g} = -\frac{1}{\vartheta^{g^2}} [\lambda \vartheta^g \mathbf{g}^{-1} + \mu [\mathbf{b} - \mathbf{n} \otimes \mathbf{n}]] \quad (2.19)$$

depends directly on the constitutive formulation for the Kirchhoff stress $\boldsymbol{\tau}$ in equation (2.9) and indirectly on the particular format of the growth tensor \mathbf{F}^g in equation (2.4). The third term

$$2 \frac{\partial \vartheta^g}{\partial \mathbf{g}} = \frac{1}{\tau} \frac{1}{\vartheta^g} \left[\frac{\vartheta^{\max} - \vartheta^g}{\vartheta^{\max} - 1} \right]^\gamma \frac{1}{\mathbf{K}^g} \Delta t \left[\vartheta \mathbf{g}^{-1} - \frac{J^2}{\vartheta} [\mathbf{F}^{-t} \cdot \mathbf{n}_0] \otimes [\mathbf{F}^{-t} \cdot \mathbf{n}_0] \right] \quad (2.20)$$

consists of the algorithmic linearization of the time discrete evolution equation for the area growth $\partial \vartheta^g / \partial \vartheta$ in equation (2.16) and of the linearization of the area stretch $2 \partial \vartheta / \partial \mathbf{g}$ in equation (2.3). The local stress of equation (2.9) and the local consistent tangent of equation (2.17) enter the global righthand side vector and the global iteration matrix of the global Newton iteration. Upon its convergence, we store the corresponding area growth ϑ^g locally at the integration point level.

2.3 Results

We illustrate the features of the proposed growth model for the simple model problem of displacement driven equi-biaxial extension and for the clinical case of tissue expansion in pediatric forehead reconstruction. For the elastic model, we assume Lamé constants of $\lambda = 0.7141$ MPa and $\mu = 0.1785$ MPa, which would correspond to a Young's modulus of $E = 0.5$ MPa and Poisson's ratio of $\nu = 0.4$ in the linear regime [3, 188]. For the growth model, we assume that growth takes place above the critical threshold of $\vartheta^{\text{crit}} = 1.21$, corresponding to uniaxial stretches of 10% [22]. We restrict the maximum area growth to $\vartheta^{\max} = 4.0$, and assume an adaptation speed of $\tau = 1/12$ and growth exponents of $\gamma = 2.0$ and $\gamma = 12.0$ in examples 2.3.1 and 2.3.2. Sensitivity analyses demonstrate

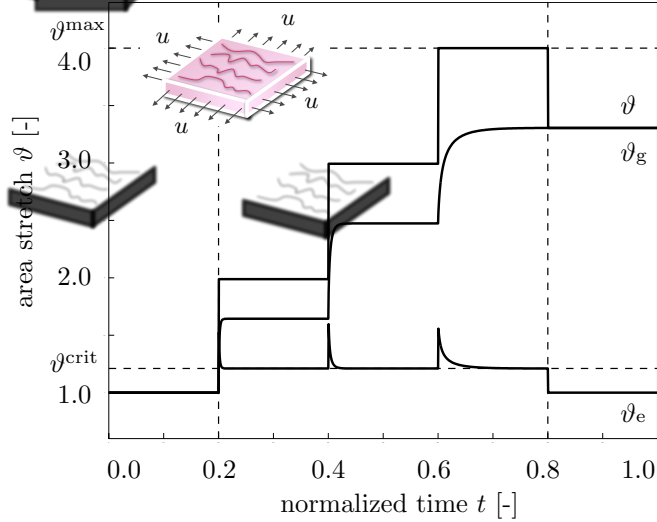


Figure 2.3: Temporal evolution of total area stretch ϑ , reversible elastic area stretch ϑ^e , and irreversible growth area stretch ϑ^g for displacement driven skin expansion. Displacements are increased and then held constant in three intervals between the vertical dashed lines, and then relaxed. Displacement control induces relaxation indicated through the gradual decrease in elastic stretch ϑ^e and stress, while the growth stretch ϑ^g increases at a constant total stretch ϑ . Horizontal dashed lines represent the elastic stretch limit beyond which skin growth is activated ϑ^{crit} , and the maximum area growth ϑ^{max} .

that the parameters τ and γ influence the adaptation time and the shape of the adaptation curve, but not the final state of biological equilibrium [87, 224].

2.3.1 Model problem - Skin growth in equi-biaxial extension

We illustrate the conceptual features of our growth model by exploring the simple model problem of displacement-driven skin expansion of a square $1.0 \times 1.0 \times 0.2$ sheet. In an equi-biaxial setting, we increase the prescribed displacements such that the in-plane area stretch is increased from $\vartheta = 1.0$ to 2.0, 3.0, and 4.0, indicated through the vertical dashed lines in Figure 2.3. This implies that the skin sheet is gradually stretched to a final size of 2.0×2.0 , i.e., to four times its original size. After applying the deformation, we allow the tissue to adapt, and recover its homeostatic equilibrium state. After three load increments, we remove the applied stretch and allow the tissue to relax.

Figure 2.3 illustrates the resulting temporal evolution of the total area stretch ϑ , the reversible elastic area stretch ϑ^e , and the irreversible area growth ϑ^g . The horizontal dashed lines represent the elastic stretch limit ϑ^{crit} beyond which skin growth is activated, and the maximum area growth ϑ^{max} . The curves confirm, that, at all times, the multiplicative decomposition of the deformation gradient $\mathbf{F} = \mathbf{F}^e \cdot \mathbf{F}^g$ introduced in equation (2.1) carries over to the multiplicative decomposition

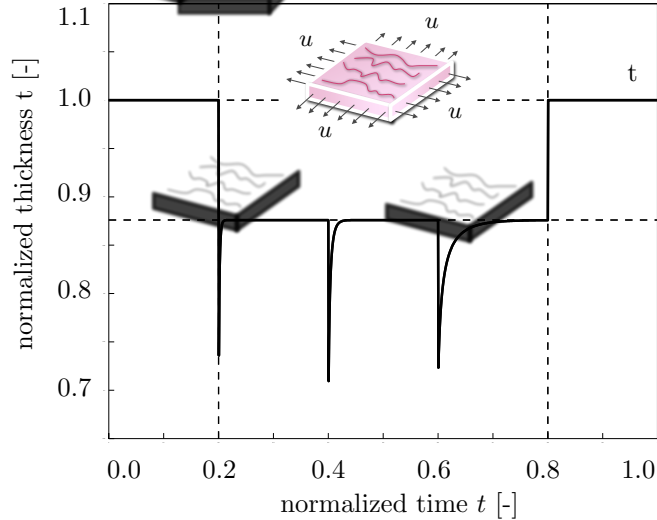


Figure 2.4: Temporal evolution of skin thickness t for displacement driven skin expansion. Displacements are increased and then held constant in three intervals between the vertical dashed lines, and then relaxed. Upon stretching, the skin thickness decreases acutely to 0.72, but then returns chronically to the homeostatic equilibrium thickness of 0.88 indicated through the lower horizontal line. This value is smaller than the original thickness because of the Poisson effect. Upon displacement relaxation, however, the skin thickness immediately returns to its original value of 1.0, indicated through the upper horizontal line.

of the total area stretch $\vartheta = \vartheta^e \vartheta^g$ of equation (2.3). Convergence towards the homeostatic state manifests itself through a gradual increase of growth ϑ^g at a constant total stretch ϑ , while the elastic stretch ϑ^e , and, accordingly the stresses, decrease. Upon removal of the applied displacements, the elastic stretch instantaneously returns to its baseline value of one, $\vartheta^e = 1$. Since the growth process is assumed to be irreversible, the growth stretch remains constant, $\vartheta^g = \text{const}$. The total stretch instantaneously adapts the value of the growth stretch, $\vartheta = \vartheta^g$.

Figure 2.4 shows the temporal evolution of the skin thickness. Upon loading, the thickness decreases acutely from 1.0 to 0.72, but then returns chronically to its loaded baseline value of 0.88. This value, indicated through the lower horizontal line, is slightly smaller than the original thickness because of the Poisson effect. Upon removal of the applied displacements, the skin thickness immediately returns to its original value of $t = 1.0$, indicated through the upper horizontal line. Since the model assumes no growth in thickness direction, $t^g = 1.0$, all thickness changes are fully reversible, $t^e = t$.

2.3.2 Clinical problem - Skin growth in pediatric forehead reconstruction

To illustrate the full potential of our model, we simulate skin expansion in pediatric forehead reconstruction for two clinical cases, a one-year old girl in case study I [82], and a one-year old boy in case study II [83], both born with giant congenital nevi affecting almost half of their foreheads,

see Figure 2.5. Because giant congenital nevi place the child at an increased risk of skin cancer, the nevus is typically removed in the early childhood [81]. To reconstruct the defect, preserve function, and maintain aesthetic appearance, both children underwent controlled tissue expansion [137]. To simulate the process of tissue expansion in an anatomically exact geometry, we create a finite element mesh from three-dimensional computer tomography images of a child of similar age following the procedure outlined in [224]. We identify the skin region by its distinct grey scale value in the computer tomography scans to create a triangular surface mesh, which we further smoothen semi-manually. From the smoothened surface mesh, we create a volume mesh of the skin layer, discretized with 61,228 nodes, 183,684 degrees of freedom, and 30,889 tri-linear brick elements. Last, we assign each element a skin plane normal \mathbf{n}_0 , corresponding to the normal of the initial surface mesh.

Case study I:

Simultaneous forehead, anterior and posterior scalp expansion

The first case study mimics the case of a one-year old girl, whose nevus covered her left posterior forehead [82]. To grow extra skin to cover the defect area, she underwent simultaneous tissue expansion in the forehead and in the anterior and posterior scalp as shown in Figure 2.5, top row. To model her case, we virtually implant three expanders. First, we implant an expander in the posterior scalp, discretized with 4,726 nodes, 14,178 degrees of freedom, and 2,270 tri-linear brick elements, covering an initial area of 53.1 cm^2 . Second, we implant two closely connected expanders in the forehead and in the scalp, discretized together with 7,954 nodes, 23,862 degrees of freedom, and 3,820 tri-linear brick elements, covering an initial area of 96.3 cm^2 . To simulate tissue expansion, we fix all nodes and release only the expander degrees of freedom, which we then pressurize from underneath. We assume that the adjacent dermis and hypodermis remain closely connected [193]. Figure 2.6 displays the temporal evolution of the normalized total area, elastic area, and growth area upon gradual expander inflation, constant pressure, and gradual expander removal. Once the elastic area stretch reaches the critical threshold of $\vartheta^{\text{crit}} = 1.21$, slightly before the total pressure is applied, at $t = 0.125$, the tissue starts to grow. As the expander pressure is held constant, growth increases gradually causing the total area to increase. Then, at $t = 0.75$, the pressure is decreased to remove the expander. The elastic area retracts gradually, while the grown area remains constant. The vertical dashed lines correspond to the discrete time points, $t = 0.24$, $t = 0.33$, $t = 0.42$ and $t = 0.75$, displayed in Figure 2.7.

Figure 2.7 illustrates the spatio-temporal evolution of the area growth ϑ^g . Growth is first initiated at the center of the expanders, where the elastic stretch is largest. As growth spreads throughout the entire expanded areas, the initial area of 149.4 cm^2 increases gradually as the grown skin area increases to 190.2 cm^2 , 207.4 cm^2 , 220.4 cm^2 , and finally 251.2 cm^2 , displayed from left to right. In detail, we observe that the final area in the posterior scalp region is 91.5 cm^2 , corresponding to a fractional area gain of 1.73. In the combined forehead and anterior scalp regions, the final area is 159.6 cm^2 , corresponding to a slightly lower fractional area gain of 1.66. Area growth displays



Figure 2.5: Skin expansion in pediatric forehead reconstruction. The patients, a one-year old girl, case study I shown in the top row [82], and a one-year old boy, case study II shown in the bottom row [83], both presented with a giant congenital nevus. Three forehead, scalp, and cheek expanders were implanted simultaneously for *in situ* skin growth. After enough skin is grown, the nevus is removed and the new skin is pulled over the wound to close it.

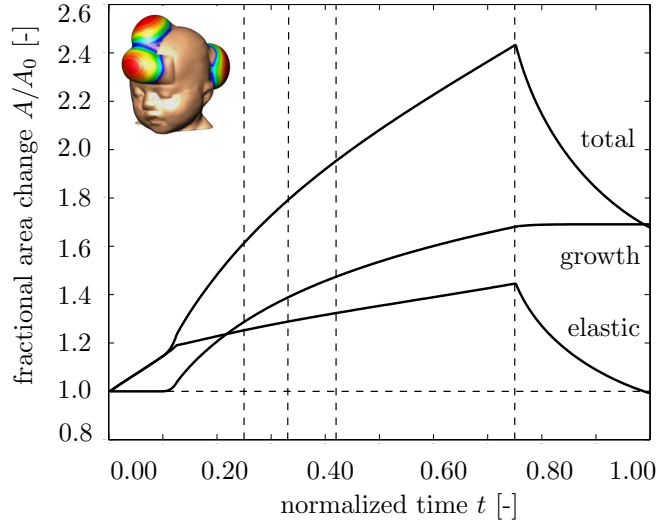


Figure 2.6: Skin expansion in pediatric forehead reconstruction. Case study I: Simultaneous forehead, anterior and posterior scalp expansion. Temporal evolution of normalized total area, elastic area, and growth area upon gradual expander inflation, $0.0 < t \leq 0.125$, constant pressure $0.125 < t \leq 0.75$, and deflation $0.75 < t \leq 1.0$. The expanded area increases from 149.4 cm^2 to 251.2 cm^2 , corresponding to a final fractional area gain of 1.68. Vertical dashed lines correspond to the time points displayed in Figure 2.7.

regional variations within $1.0 \leq \vartheta^g \leq 2.0$, i.e., in some regions, the skin has doubled its initial area. Area growth is largest in the center regions and smallest in the peripheries.

Case study II:

Simultaneous forehead, scalp, and cheek expansion

The second example mimics the case of a one-year old boy whose nevus covered his right anterior forehead [83]. We simulate his simultaneous tissue expansion with expanders in the forehead, scalp, and cheek as shown in Figure 2.5, bottom row. First, we virtually implant an expander in the scalp, discretized with 4,356 nodes, 13,068 degrees of freedom, and 2,088 tri-linear brick elements, covering an initial area of 50.5 cm^2 . Second, we implant an expander in the cheek, discretized with 2,542 nodes, 7,626 degrees of freedom, and 1,200 tri-linear brick elements, covering an initial area of 29.3 cm^2 . Third, we implant an expander in the forehead, discretized with 3,782 nodes, 11,346 degrees of freedom, and 1,800 tri-linear brick elements, covering an initial area of 48.8 cm^2 . Again, we fix all nodes and release only the expander degrees of freedom, which we then pressurize from underneath, assuming that the adjacent skin remains unaffected.

Figure 2.8 displays the temporal evolution of the normalized total area, elastic area, and growth area upon gradual expander inflation, constant pressure, and gradual expander removal. Similar to Figure 2.6, the tissue begins to grow once the elastic area stretch reaches the critical threshold of

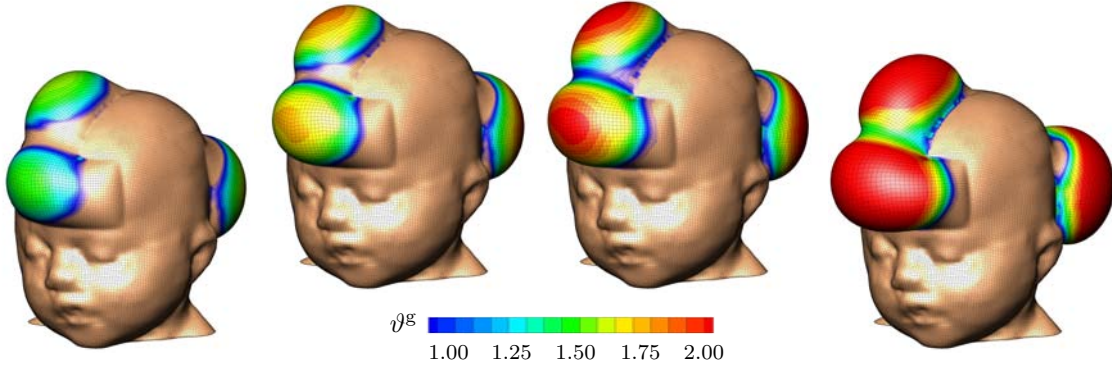


Figure 2.7: Skin expansion in pediatric forehead reconstruction. Case study I: Simultaneous forehead, anterior and posterior scalp expansion. Spatio-temporal evolution of area growth displayed at $t = 0.24$, $t = 0.33$, $t = 0.42$ and $t = 0.75$. The initial area of 149.4 cm^2 increases gradually as the grown skin area increases to 190.2 cm^2 , 207.4 cm^2 , 220.4 cm^2 , and finally 251.2 cm^2 , from left to right.

$\vartheta^{\text{crit}} = 1.21$. Slightly after, at $t = 0.125$, the total pressure is held constant. Similar to the first case study, the skin grows gradually in all three expanded regions. When the pressure is gradually decreased at $t = 0.75$, the elastic area retracts, while the grown area remains constant. The vertical dashed lines correspond to the discrete time points, $t = 0.24$, $t = 0.33$, $t = 0.42$ and $t = 0.75$, displayed in Figure 2.9.

Figure 2.9 illustrates the spatio-temporal evolution of the area growth ϑ^g . Since area stretches are largest at the center of the expander, growth is first initiated in this region, spreading gradually throughout the entire expanded areas. During the growth process, the initial area of 128.7 cm^2 increases to 176.0 cm^2 , 191.3 cm^2 , 202.1 cm^2 , and finally 227.1 cm^2 , displayed from left to right. In detail, we observe that the new area in the scalp is 87.9 cm^2 with a fractional area gain of 1.74, in the cheek it is 50.6 cm^2 with a fractional area gain of 1.72, and in the forehead it is 88.6 cm^2 with the largest fractional area gain of 1.82. The area growth varies locally within the range of $1.0 \leq \vartheta^g \leq 2.0$ with largest values in the center regions, where skin typically more than doubles its initial area.

2.4 Discussion

Motivated by the mechanotransduction pathways outlined in Section 2.1, we have introduced a continuum model for growing skin in response to chronic mechanical overstretch. From a kinematic point of view, the model is based on the multiplicative decomposition of the deformation gradient into an elastic part and a growth part [183]. From a constitutive point of view, it introduces four material parameters with a clear physiological interpretation [139, 224], the critical physiological stretch limit ϑ^{crit} , the maximum area growth ϑ^{max} , the adaptation speed τ , and the shape of the adaptation curve γ . From a computational point of view, the model is embedded in a standard nonlinear finite

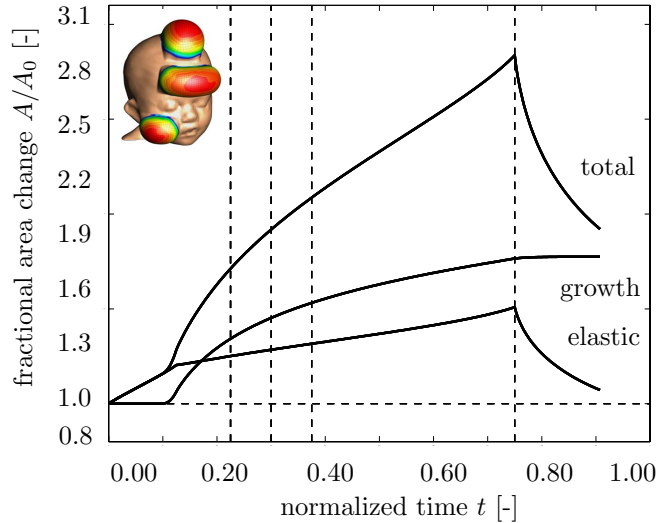


Figure 2.8: Skin expansion in pediatric forehead reconstruction. Case study II: Simultaneous forehead, scalp, and cheek expansion. Temporal evolution of normalized total area, elastic area, and growth area upon gradual expander inflation, $0.0 < t \leq 0.125$, constant pressure $0.125 < t \leq 0.75$, and deflation $0.75 < t \leq 1.0$. The expanded area increases from 128.7 cm^2 to 227.1 cm^2 , corresponding to a final fractional area gain of 1.77. Vertical dashed lines correspond to the time points displayed in Figure 2.9.

element framework, in which the area growth ϑ^g is introduced locally as an internal variable on the integration point level [87, 118]. From an algorithmic point of view, the biological equilibrium problem for this internal variable is solved using a local Newton iteration embedded in a global Newton iteration to solve the mechanical equilibrium problem [71, 176]. Overall, our growth model is unconditionally stable, robust, efficient, conceptually modular, and easily portable. In contrast to the only other skin growth model by other authors, which is based on a rotationally symmetric formulation [193], our model is conceptually generic, and can handle arbitrary skin geometries. In contrast to our own first prototype of the model, which is based on a material formulation [36, 224], the new realization based on a spatial formulation is computationally elegant and efficient, reducing simulation times by approximately factor five.

In Section 2.3.1, we have demonstrated the conceptual characteristics of our growth model by means of a simple model problem of successive equi-biaxial extension. Upon displacement control, the model predicts the following features: (i) an acute increase in the elastic area stretch ϑ^e , (ii) an acute decrease in thickness t , (iii) a chronic increase in area growth ϑ^g , (iv) a chronic restoration of the homeostatic elastic area stretch $\vartheta^e \rightarrow \vartheta^{\text{crit}}$, and (v) a chronic restoration of the homeostatic equilibrium thickness t . Upon displacement relaxation, the model predicts the following features: (vi) an acute retraction of the elastic area stretch back to its baseline value of $\vartheta^e = 1.0$ and (vii) an acute arrest of further growth with $\vartheta = \vartheta^g = \text{const}$, see Figures 2.3 and 2.4.

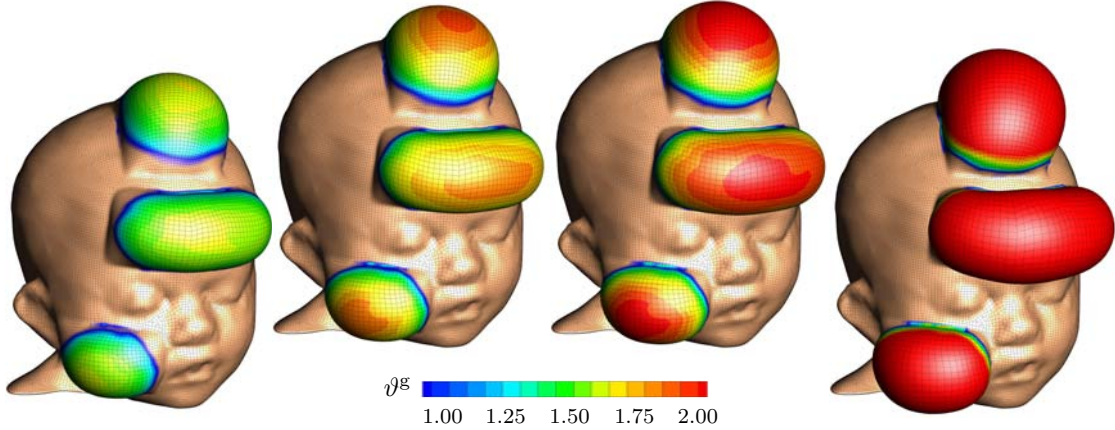


Figure 2.9: Skin expansion in pediatric forehead reconstruction. Case study II: Simultaneous forehead, scalp, and cheek expansion. Spatio-temporal evolution of area growth displayed at $t = 0.24$, $t = 0.33$, $t = 0.42$ and $t = 0.75$. The initial area of 128.7 cm^2 increases gradually as the grown skin area increases to 176.0 cm^2 , 191.3 cm^2 , 202.1 cm^2 , and finally 227.1 cm^2 , from left to right.

Our *in silico* predictions are in excellent agreement with the *in vivo* findings reported in the literature. More than three decades ago, the first experimental studies confirmed a net gain in skin area upon tissue expansion [15, 16]. Unexpectedly, this area gain was found to take place upon conservation of cellular morphology, preservation of phenotype, and maintenance of functionality, without an inflammatory response, and without evidence of malignant degeneration [22]. This suggested that the increase in tissue surface area is a result of new tissue being regenerated, instead of being recruited from neighboring regions [55]. It supports our fundamental model assumption that skin is capable to chronically increase its area, represented through equation (2.3), upon mechanical overstretch, incorporated through equation (2.12), see Figure 2.3.

In what follows, we will compare the response of our model to skin growth experiments in the literature [16, 19, 22, 210, 212, 218]. Unfortunately, almost all existing data are based on *in vivo* tissue expansion studies. For the lack of experimental data, we assume that the *in vivo* strain state of a pressurized thin membrane is close to our *in silico* state of equi-biaxial extension. Alternatively, we could simulate the true state of tissue expansion using finite element models [36, 37]. However, since this would introduce additional discretization and modeling errors, we will assume a homogeneous strain state here, and focus on comparing the constitutive, material point response.

2.4.1 Discussion of acute elastic response

Acutely, tissue expansion has been associated with slight epidermal thickening and significant dermal thinning [16], resulting in an overall thinning and a reduced tensile strength [19]. Mechanically, a study in rodents reported an acute increase in uniaxial stretch of approximately 36% [22]. This is in nice agreement with our model, which predicts an acute elastic area stretch of 1.52, 1.60, and

1.56, corresponding to an average increase in uniaxial stretch of 25%, see Figure 2.3. Structurally, the same study identified an initial acute decrease in skin thickness from $407 \pm 3 \mu\text{m}$ to $317 \pm 4 \mu\text{m}$ corresponding to an acute thickness reduction of 22% [22]. Again, this is in good quantitative agreement with our model, which predicts an acute average normalized thickness of 0.74, 0.71, and 0.72 corresponding to an acute average thickness decrease of 28%, see Figure 2.4. Since these acute thickness changes can be attributed primarily to the Poisson effect, they can be utilized to calibrate the elastic material parameters, in particular Poisson's ratio.

2.4.2 Discussion of chronic growth response

Chronically, tissue expansion is associated with the gradual restoration of baseline histology, baseline mechanics, and baseline structure [19]. Histologically, a comparison of piglet tissue in expanded and non-expanded regions demonstrated a chronic restoration of the number of epidermal cell layers and a chronic restoration of the epidermal thickness [210]. In addition, immunocytochemistry confirmed that the expanded tissue maintains its phenotypical characteristics and native program of cellular differentiation [218]. Mechanically, in a multiple time-point study in rodents, an acutely increased uniaxial stretch of 36% was reduced chronically to approximately 10% 32 days post expansion [22]. This is in excellent agreement with our model, which predicts an acutely increased uniaxial stretch of 25% and a chronic reduction to 10%, see Figure 2.3. A uniaxial stretch of 10% would correspond to an area stretch of $\vartheta^{\text{crit}} = 1.21$. In our model, the model parameter ϑ^{crit} takes the interpretation of the physiological threshold value, to which the elastic area stretch tends to return during adaptive skin growth, see equation (2.12). Structurally, after an initial acute thickness decrease of 22%, the same study reports a chronic restoration of the homeostatic equilibrium thickness from initially $425 \pm 4 \mu\text{m}$ to $398 \pm 3 \mu\text{m}$, corresponding to a chronic thickness reduction of 7% [22]. This agrees well with our model, which predicts a normalized homeostatic equilibrium thickness of 0.88, corresponding to a chronic thickness reduction 12%, see Figure 2.4. The chronic rodent study also reported that the overall weight of the tissue sample almost tripled, with a fractional weight gain of approximately 2.7 for wet weight and 3.3 for dry weight [22]. In our model, the fractional weight gain is directly proportional to the fractional area gain of $\vartheta^{\text{g}} = 3.3$ which agrees nicely with these experimental findings, see Figure 2.3. Finally, the study found a conservation of the mechanical properties, for example, a constant breaking strength acutely right after expansion and chronically long term [22]. These findings support our model assumption that ultimately, the newly created skin will have the same microstructure, density, and stiffness, as the original, native tissue [36, 37].

2.4.3 Discussion of elastic retraction

Acutely, upon expander removal, an instantaneous retraction of the elastic deformation significantly reduces the overall skin area. In controlled in vivo experiments in pigs, the ratio between the reversible elastic deformation to irreversible growth was almost 2:1 [212]. Since our model assumes

that the overall deformation gradient can be multiplicatively decomposed into an elastic and growth part, represented through equation (2.1), it is perfectly capable of reproducing the effect of elastic retraction upon expander removal, see Figures 2.3, 2.6, and 2.8.

2.4.4 Discussion of growth heterogeneity

Figures 2.7 and 2.9 clearly indicate the heterogeneity of the growth process with larger values in the center region and smaller values in the periphery. This is in agreement with *in vivo* studies, which report a fractional area gain of 3.14, i.e., 50% above average, in the center region, and 2.06, i.e., 25% below average, in the periphery [22]. The authors hypothesized that larger strains in the center region would trigger larger growth. This is in agreement with our model in equation (2.10), where the evolution of area growth is directly correlated to the amount of overstretch through the growth criterion defined in equation (2.12).

2.4.5 Limitations

Although we have presented both qualitative and quantitative comparisons of the proposed model with acute and chronic tissue expansion experiments from the literature, several limitations remain. First and foremost, the most challenging aspect would be to tie the growth law in equation (2.4) more closely to the underlying mechanobiology described in detail in the introduction section. Comparative gene expression assays and immunohistochemistry of grown versus ungrown tissue samples could help to identify the mechanisms that trigger skin growth on the molecular and cellular level. Similar approaches have been proposed for amelogenesis [49] and tumorigenesis [14, 170] in the past and could also be adopted here. Ideally, this would help to specify our evolution equation for the growth tensor (2.4) in terms of discrete mechanotransduction cascades through selected extracellular and intracellular events. To this end, we are currently designing a test setup to stretch and grow explanted tissue samples *ex vivo*. Since most existing data sets on skin growth are based on *in vivo* measurements of inflated membranes, an *ex vivo* setting will allow us to create well-defined geometries and boundary conditions such as the equi-biaxial extension test suggested here.

Second, since our goal was to focus primarily on the kinematic characterization of the growth process, the constitutive modeling of the elastic baseline properties of skin has played a minor role. However, the proposed model is inherently modular and the incorporation of more sophisticated constitutive models [213] is relatively straightforward. A typical candidate is a multiple-constituent anisotropic skin model with in-plane anisotropy introduced through a pronounced stiffness along Langer's lines [116, 117], which we have successfully combined with the proposed growth model in the past [37]. In addition, the growth process itself could be modeled as anisotropic [72], e.g., attributed to a pronounced growth along specific microstructural directions. Similarly, through the deposition of large bundles of compacted immature collagen [19, 109], the underlying collagen network could reorient itself, e.g., to align with the maximum principal strains [88, 119]. Here, we model

growth as a strain driven process. This implies that the elastic material parameters, or, accordingly, the corresponding stresses, play a less important role than in stress-driven growth, e.g., in hypertension [118,176]. In other words, when using the same model with different Lamé constants or different constitutive models, we would require different expander pressures to obtain the same deformation pattern, but the growth process itself would still be affected by kinematical quantities only. Along the same lines, we have assumed that the effects of resting tension and residual stress are negligible. Both play a critical role when studying instabilities and buckling [77,211]. In a previous study, we have explored these phenomena in more detail [36]. Within the context of finite deformations, resting tension and residual stress could be incorporated through another second order tensor, which would mimic the mapping to a pre-strained or residually stressed configuration [150,200].

Third, for the sake of simplicity, we have modeled skin as homogeneous across the thickness, neglecting its individual layers and their potential interaction. We are currently refining our model utilizing shell kinematics with a higher resolution across the thickness direction. This will facilitate to model the individual skin layers [191], which we believe to be a major source of heterogeneities and residual stresses in real tissue expansion cases [149]. Alternatively, to explore the biomechanical interaction between the growing dermis and the underlying hypodermis during tissue expansion, we could even model growing skin through its own boundary energy [95].

Fourth, at this stage, the chronic response of our model is not yet calibrated in time. We have assumed that chronic growth takes place within a normalized time interval from zero to one. In reality, growth periods range from the order of days in rodents [22] to weeks in pigs [212] and humans [83]. However, with the appropriate experimental data, the duration of the adaptation process can be calibrated easily through the adaptation speed τ [224].

Fifth, we have modeled the tissue expander only implicitly through controlling the expander pressure. In real tissue expansion, the external control parameter is the expander volume [137]. This implies that our simulation displays creep under constant loading, while clinical tissue expansion might rather display relaxation under constant deformation [37]. Moreover, we have assumed that the expander is connected tightly to the expanded tissue, neglecting effects of interface sliding and shear [193]. However, this seems to be a reasonable first assumption, since most current expanders have well-designed textures to promote mild tissue in-growth, primarily to prevent expander migration [21].

Last, while our computational model seems well suited to provide qualitative guidelines and trends, in its present state, it is not recommended for quantitative statements. We will need to perform acute and chronic *in vitro* and *in vivo* experiments to truly identify the underlying mechanisms which have, up until now, only been represented phenomenologically. Nevertheless, we believe that using the equations of nonlinear continuum mechanics to characterize skin growth represents a significant advancement over the current gold standard to predict tissue growth exclusively in terms of areas, volumes, and empiric correction factors [189,212].

2.5 Conclusion

We have presented a continuum model for growing biological membranes in which the underlying mechanobiology is collectively summarized in a single phenomenological internal variable, the in-plane area growth. The model can reliably predict the characteristic histological, mechanical, and structural features of controlled overstretch-induced skin growth, both acutely and chronically. We anticipate that the proposed skin growth model can be generalized to arbitrary biological membranes, and that it can serve as a valuable tool to virtually manipulate membrane area simply by means of changes in the mechanical environment.

Acknowledgements

We acknowledge the support by Professor Arun K. Gosain, Department of Plastic Surgery, Case Western Reserve University, Cleveland, Ohio, for stimulating discussions, and for providing the computer tomography images of the pediatric skulls. This work was supported by the Stanford Graduate Fellowship to Adrián Buganza Tepole and by the National Science Foundation CAREER award CMMI-0952021 and the National Institutes of Health Grant U54 GM072970 to Ellen Kuhl.

Chapter 3

Realistic, volume controlled skin expander model

Abstract

Skin is a highly dynamic, autoregulated, living system that responds to mechanical stretch through a net gain in skin surface area. Tissue expansion uses the concept of controlled overstretch to grow extra skin for defect repair in situ. While the short-term mechanics of stretched skin have been studied intensely by testing explanted tissue samples *ex vivo*, we know very little about the long-term biomechanics and mechanobiology of living skin *in vivo*. Here we explore the long-term effects of mechanical stretch on the characteristics of living skin using a mathematical model for skin growth. We review the molecular mechanisms by which skin responds to mechanical loading and model their effects collectively in a single scalar-valued internal variable, the surface area growth. This allows us to adopt a continuum model for growing skin based on the multiplicative decomposition of the deformation gradient into a reversible elastic and an irreversible growth part. To demonstrate the inherent modularity of this approach, we implement growth as a user-defined constitutive subroutine into the general purpose implicit finite element program Abaqus/Standard. To illustrate the features of the model, we simulate the controlled area growth of skin in response to tissue expansion with multiple filling points in time. Our results demonstrate that the field theories of continuum mechanics can reliably predict the manipulation of thin biological membranes through mechanical overstretch. Our model could serve as a valuable tool to rationalize clinical process parameters such as expander geometry, expander size, filling volume, filling pressure, and inflation timing to minimize tissue necrosis and maximize patient comfort in plastic and reconstructive surgery. While initially developed for growing skin, our model can easily be generalized to arbitrary biological structures to explore the physiology and pathology of stretch-induced growth of other living systems such as hearts, arteries, bladders, intestines, ureters, muscles, and nerves.



Figure 3.1: Skin expansion in pediatric scalp reconstruction. The patient, a one year-old boy, presented with a giant congenital nevus, left. To grow extra skin for defect repair in situ, tissue expanders are implanted in the frontoparietal and occipital regions of his scalp, middle left. The expanders are gradually filled with saline solution to apply mechanical overstretch and trigger controlled skin growth, middle right. Four months post implantation, the tissue expanders are removed, the nevus is excised, and the defect area is covered by tissue flaps created from the newly grown skin, right.

3.1 Mechanobiology Of Growing Skin

3.1.1 At the organ level, mechanical stretch induces skin growth

Skin is the largest mechanoreceptive interface of our body and protects our muscles, bones, ligaments, and all our internal organs from chemical, biological, thermal, and mechanical influences of our environment [147]. Remarkably, skin is highly responsive to mechanical loading and can easily double its initial area when subject to mechanical stretch [19]. Plastic and reconstructive surgery capitalize on this dynamic adaptation of skin through the concept of tissue expansion, a controlled application of overstretch to grow new skin in situ [181]. Figure 3.1 illustrates a clinical case of tissue expansion in pediatric scalp reconstruction. The patient, a one year-old boy, presented with a giant congenital nevus [11]. To grow extra skin for defect repair in situ, tissue expanders were implanted in the frontoparietal and occipital regions of his scalp. The expanders were gradually filled with saline

solution to create mechanical overstretch and initiate controlled skin growth [81]. Four months post implantation, the tissue expanders were removed, the nevus was excised, and the defect area was covered by tissue flaps created from the newly grown skin [83]. When the concept of tissue expansion was first introduced, the stretched skin was believed to simply redistribute its mass by increasing its area while reducing its thickness [16]. We now know that skin actually grows in mass; it increases its area while its thickness remains virtually unchanged [168]. Macroscopically, the newly grown skin not only has the same thickness, but also the same mechanical properties as the native tissue [22]. Microscopically, it displays the same surface waviness and possesses a similar cell-to-matrix volume fraction as the original tissue [203]. While tissue expansion has become a widely used procedure in plastic and reconstructive surgery since it was first introduced more than half a century ago [154], there are still no quantitative, mechanistic criteria for the appropriate selection of the relevant clinical process parameters such as expander geometry, expander size, filling volume, filling pressure, and inflation timing [212]. The success of the procedure almost exclusively relies on the skills and experience of the surgeon and on his personal judgement [81]. A common complication associated with the lack of experience is overinflation, which causes skin thinning, necrosis, sloughing, and trauma through excessive tissue tension and compromised vascularization [137]. While it is virtually impossible to measure tissue tension in the living skin *in vivo*, mathematical modeling provides a safe and cheap alternative to estimate stress, strain, and area gain and avoid overstretch [36]. Personalized computational simulations have the potential to optimize the set of clinical process parameters with the ultimate goal of maximizing surface area gain while minimizing stress, tissue necrosis, inflation timing, and patient discomfort [225].

3.1.2 At the tissue level, mechanical stretch initiates cell-cell and cell-matrix signaling

Skin is a composite microstructural material consisting of two distinct layers, the epidermis and the dermis [47], see Figure 3.2. The epidermis, shown in dark purple in Figure 3.2, is the 0.1-1.0 mm-thick, waterproof, protective, outer layer. It consists of an approximately four-cell-thick layer of densely packed keratinocytes, which constitute 95% of all cells in the epidermis [147]. Cells of the innermost epidermis, the basal keratinocytes, have a brick-type shape and are joined together tightly by desmosomal junctions. Basal keratinocytes are attached to the basement membrane, the 200 μm -thick divider between the epidermis and the dermis, via a complex network of proteins and glycoproteins including hemidesmosomes and integrin receptors [191]. Mechanical continuity at the basement membrane is key for appropriate force transfer between the epidermis and the dermis. The dermis, shown in pink in Figure 3.2, is the 0.5-5.0 mm-thick, load-bearing inner layer. In contrast to the epidermis, the dermis is largely acellular and consists of 60% water. Of its remaining dry weight, 80-85% consists of loosely interwoven, wavy, randomly oriented collagen fibers, supplemented by 2-4% of elastin [147]. At low mechanical strains, the elastin fibers are stretched out, while the wavy

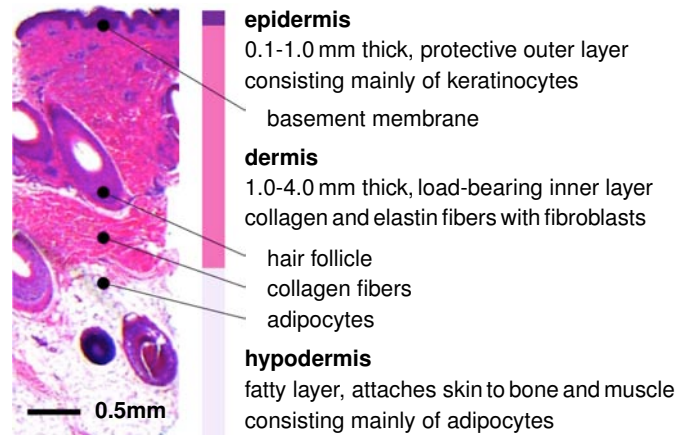


Figure 3.2: Histological cross section of human skin. Skin is a composite material of multiple layers: The epidermis, the thin outer layer, has a protective barrier function. It consists primarily of densely packed keratinocytes. The dermis, the inner layer, is the main load-bearing element of skin. Its extracellular matrix consists of loosely interwoven collagen and elastin fibers; its major cells are fibroblasts. The hypodermis, the subcutaneous layer, connects skin to bone and muscle. It consists primarily of adipocytes.

collagen fibers uncrimp and do not contribute markedly to the overall skin stiffness [133]. At higher strains, the stretched, crosslinked collagen network is the main load-carrying element responsible for the characteristic strain locking [116]. Fibroblasts, the major cell type in the dermis, are responsible for the synthesis of extracellular matrix proteins and regulate the collagen content. From below, the dermis is demarcated by the hypodermis, shown in white in Figure 3.2, a subcutaneous fatty layer that connects skin to bone and muscle. The hypodermis consists primarily of adipocytes. Its major functions are to provide insulation, mechanical cushioning, and energy storage [147]. When exposed to tension, for example internally-generated during wound healing [39] or externally-applied during tissue expansion [55], forces need to be transferred between the different layers of skin [191]. In the epidermis, stretching of keratinocyte-keratinocyte junctions and of the keratinocyte-basement-membrane interface initiates active cell-cell crosstalk and cell-matrix interaction. In the dermis, stretching of fibroblast-fibroblast junctions and of the fibroblast-collagen interface triggers active cell-cell crosstalk and cell-matrix interaction. In the following two subsections, we review both the mechanisms and the associated mechanotransduction pathways in epidermal keratinocytes and dermal fibroblasts.

3.1.3 At the cellular level, epidermal tension upregulates keratinocyte mitosis

Epidermal tension initiates substantial changes in keratinocyte morphology [166], which manifest themselves in basal keratinocytes flattening [15], and in shape changes from columnar to cuboidal [98]. These configurational changes may directly impact the keratinocyte cytoskeleton and induce a reorientation of F-actin perpendicular to the direction of stretch [202]. These morphological alterations activate biochemical signaling cascades through the initiation of mitogen-activated protein kinase and extracellular signal-regulated kinase pathways [203]. Mitogen-associated protein kinase signaling pathways convey information to effectors, coordinate incoming information from other signaling cascades, amplify signals, and initiate a variety of response patterns [191]. In particular, they trigger the activation of growth factor pathways that affect gene expression and protein synthesis. These mechanisms jointly converge in an upregulated mitotic activity [15,166]. However, this increase is not associated with epidermal hyperplasia [65]. Ultimately, epidermal tension results in an increase in the total number of epidermal keratinocytes and a net gain in epidermal surface area. While epidermal stretch causes an acute thickening of the epidermal layer [166], after several months, the epidermal thickness chronically returns to its baseline value [168].

3.1.4 At the cellular level, dermal tension upregulates fibroblast mitosis and synthesis of extracellular matrix proteins

Dermal tension is sensed by dermal fibroblasts as a stretch in the extracellular matrix, see Figure 3.3. Transmembrane mechanosensors in the form of stretch-activated ion channels, integrins, growth factor receptors, and G-protein-coupled receptors translate these extracellular strains into intracellular signals [94,138]. Stretch-activated ion channels, shown in orange in Figure 3.3, open in response to elevated membrane strains, allowing positively charged calcium ions and other cations to enter the cell. Changes in the intracellular calcium concentration regulate intracellular signaling, alter actin polymerization, and trigger cytoskeletal remodeling [203]. Integrins are heterodimeric transmembrane receptors composed of a regulatory α -unit and a signal transducing β -unit, shown in pink and blue in Figure 3.3. They play a critical role in force transmission across the cell membrane by connecting extracellular collagen to intracellular actin filaments via focal adhesion complexes, talin, and vinculin [192]. Integrins initiate cytoskeletal rearrangement and trigger targets such as nitric oxide signaling, mitogen-associated protein kinases, Rho GTPases, and phosphoinositol-3-kinase. Fibroblast-collagen tension mediated by integrins is an important mechanism to maintain dermal structure and function [191]. Growth factor receptors, shown in yellow in Figure 3.3, bind to growth factors outside the cell and turn on several receptor-mediated pathways inside the cell, such as nitric oxide signaling and mitogen-associated protein kinases [94]. G-protein-coupled receptors, shown in blue in Figure 3.3, are seven-transmembrane proteins, which can potentially be

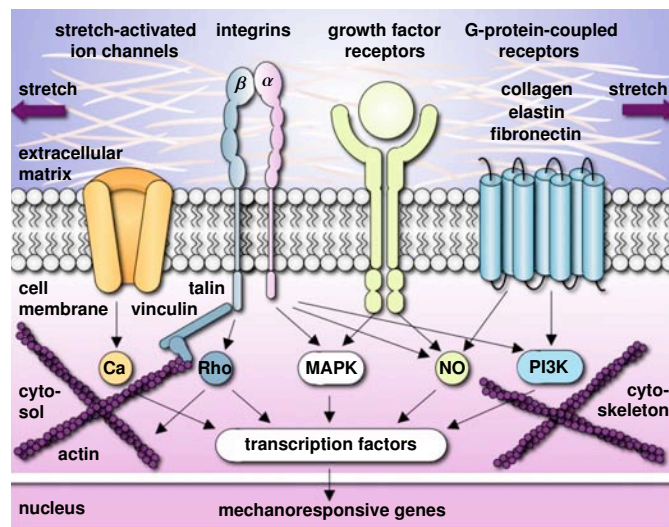


Figure 3.3: Mechanotransduction of growing skin. Transmembrane mechanosensors in the form of stretch-activated ion channels, integrins, growth factor receptors, and G-protein-coupled receptors translate extracellular signals into intracellular signaling pathways involving calcium (Ca), nitric oxide (NO), mitogen-associated protein kinases (MAPK), Rho GTPases (Rho) and phosphoinositol-3-kinase (PI3K). Biomechanical and biochemical signals converge in the activation of transcription factors that translocate the nucleus and activate mechanoresponsive genes. Increased mitotic activity and increased protein synthesis increase the skin surface area to restore the homeostatic equilibrium state.

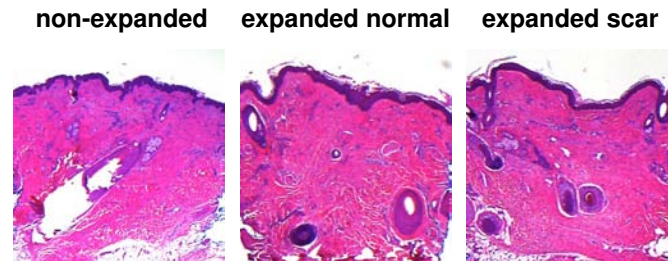


Figure 3.4: Histological sections of non-expanded control, left, expanded normal skin, middle, and expanded scar, left, from pediatric scalp. Skin expansion creates new skin with the same histological appearance as the native skin: The epidermis of the expanded skin displays a similar wrinkling pattern and thickness as the non-expanded skin. The dermis of the expanded skin displays the same thickness as the non-expanded skin. Expanded and non-expanded samples are histologically similar with similar cell-to-matrix volume ratios and a similar collagenous microstructure.

activated by mechanical stretch outside the cell to initiate mechanotransduction pathways inside the cell. Their stretch-induced conformational changes initiate second messenger cascades such as nitric oxide signaling and phosphoinositol-3-kinase [203]. Last, the cytoskeleton itself serves as an important internal signaling mechanism. It undergoes highly dynamic conformational changes induced by intracellular strain. These changes may affect the binding affinities to specific molecules and activate additional signaling pathways involving the protein kinase family, second messengers, and nuclear proteins [124]. In summary, dermal tension initiates multiple signaling pathways, which can have a substantial overlap and crosstalk. Since biomechanical signaling pathways are typically shared with biochemical receptor-mediated pathways, it is virtually impossible to study individual pathways in complete isolation. We know, however, that all these signaling pathways converge in the activation of transcription factors, which stimulate gene expression and other nuclear events [94,138]. Ultimately, dermal tension causes an increase in extracellular matrix proteins and in the total number of dermal fibroblasts, which jointly result in a net gain in dermal surface area. While dermal stretch causes an acute thinning of the dermal layer [166], after several months, the dermal thickness chronically returns to its baseline value [168].

3.2 Histology Of Growing Skin

To explore structural changes upon tissue expansion, we collected skin samples from non-expanded and expanded regions of a pediatric human scalp. Figure 3.4 shows histological sections of a non-expanded control sample, left, an expanded normal skin sample, middle, and an expanded scar sample, right.

The epidermis, stained in purple in Figure 3.4, does not change markedly upon expansion. It displays a similar wrinkling pattern in all three samples [134]. The thickness of the expanded

epidermis is similar to the non-expanded epidermis. The expanded epidermis shows no evidence of necrosis, inflammation, or epidermal hyperplasia. Overall, we conclude that tissue expansion initiates an increase in epidermal surface area at constant epidermal thickness through increased keratinocyte mitosis. These observations are in excellent agreement with findings reported in the literature [15, 65, 168]. Histological analyses in the literature report that, long-term, neither the epidermal thickness nor the number of epidermal layers undergo statistically significant changes after tissue expansion [210, 218].

Similar to the epidermis, the dermis, stained in pink in Figure 3.4, does not change noticeably upon tissue expansion. The average dermal thickness is 2.0 mm in the non-expanded sample and 2.05 mm in the expanded samples. However, the expanded dermal thickness varies locally depending on the presence of subcutaneous adipocytes. The expanded dermis is histologically similar to the non-expanded dermis with similar cell-to-matrix volume ratios and a similar loosely interwoven, wavy, randomly-oriented collagenous microstructure. It shows no evidence of inflammation, no evidence of malignant degeneration, and no loss of microstructural organization. Overall, we conclude that tissue expansion initiates an increase in dermal surface area at constant dermal thickness through increased fibroblast mitosis and increased collagen synthesis. These observations are in agreement with findings reported in the literature both in animals [15, 166] and in humans [181].

Unlike the epidermis and the dermis, the subcutaneous hypodermis undergoes significant changes upon tissue expansion. Subcutaneous adipocytes are compressed and diminished in size. This results in a significant net thinning of the subcutaneous layer. The expanded region itself undergoes subcutaneous fibrosis with a host inflammatory response. Subcutaneous collagen fibers and fibroblasts reorient themselves parallel to the expander, which becomes surrounded by a thin layer of histiocytes. These observations agree nicely with findings in the literature [15, 65, 166]. Histological analyses in the literature report flattening, shrinkage, and atrophy of adipocytes as well as an acute thinning of the subcutaneous layer, which gradually returns to its baseline thickness within two years after completion of the procedure [167].

These histological observations have important consequences when modeling skin growth: First, we can confidently assume that the thickness of the epidermal and dermal layers does not change when skin is subjected to controlled chronic overstretch. Second, we can assume that the newly grown skin has the same microstructure and the same mechanical properties as the original native tissue. Third, since the skin area increases and the thickness remains constant, skin undergoes significant changes in mass and can be modeled thermodynamically as an open system.

3.3 Continuum Modeling Of Growing Skin

Motivated by the mechanobiology of growing skin summarized in Section 3.1 and by our histological study in Section 3.2, we now formulate a continuum model for controlled stretch-induced skin growth.

To characterize the large deformations when stretching skin, we introduce the deformation map $\boldsymbol{\varphi}$, which maps points \mathbf{X} from the undeformed configuration to their new positions $\mathbf{x} = \boldsymbol{\varphi}(\mathbf{X}, t)$ in the deformed configuration. We can then characterize changes of infinitesimal line elements through the deformation gradient,

$$\mathbf{F} = \nabla_{\mathbf{X}} \boldsymbol{\varphi} = \mathbf{F}^e \cdot \mathbf{F}^g, \quad (3.1)$$

which we decompose multiplicatively into an elastic part \mathbf{F}^e and a growth part \mathbf{F}^g [67,183]. Similarly, we can characterize changes in skin volume through the Jacobian,

$$J = \det(\mathbf{F}) = J^e J^g, \quad (3.2)$$

which we decompose into a reversibly elastic volume change $J^e = \det(\mathbf{F}^e)$ and an irreversibly grown volume change $J^g = \det(\mathbf{F}^g)$. Motivated by our histological analysis in Section 3.2, we assume that the response in the thickness direction \mathbf{n}_0 is purely reversible and elastic. In the skin plane, orthogonal to \mathbf{n}_0 , we characterize skin growth through a single scalar-valued variable, the surface area growth ϑ^g . This allows us to characterize changes in skin area through the area stretch,

$$\vartheta = \|J \mathbf{F}^{-t} \cdot \mathbf{n}_0\| = \vartheta^e \vartheta^g, \quad (3.3)$$

which we decompose into a reversibly elastic area change ϑ^e and an irreversibly grown area change ϑ^g , where \mathbf{n}_0 denotes the skin plane unit normal in the undeformed reference configuration [36]. With the assumptions above, the growth tensor \mathbf{F}^g takes the following simple format [226],

$$\mathbf{F}^g = \sqrt{\vartheta^g} \mathbf{I} + [1 - \sqrt{\vartheta^g}] \mathbf{n}_0 \otimes \mathbf{n}_0. \quad (3.4)$$

Since we assume that skin does not grow in the thickness direction, its area growth is identical to its volume growth, i.e., $\vartheta^g = \|J^g \mathbf{F}^{g-t} \cdot \mathbf{n}_0\| = \det(\mathbf{F}^g) = J^g$. Using the simple rank-one update structure of \mathbf{F}^g , we can explicitly invert the growth tensor with the help of the Sherman-Morrison formula [151],

$$\mathbf{F}^{g-1} = \frac{1}{\sqrt{\vartheta^g}} \mathbf{I} + \left[1 - \frac{1}{\sqrt{\vartheta^g}}\right] \mathbf{n}_0 \otimes \mathbf{n}_0. \quad (3.5)$$

From the multiplicative decomposition (3.1), we then obtain an explicit representation of the elastic tensor $\mathbf{F}^e = \mathbf{F} \cdot \mathbf{F}^{g-1}$,

$$\mathbf{F}^e = \frac{1}{\sqrt{\vartheta^g}} \mathbf{F} + \left[1 - \frac{1}{\sqrt{\vartheta^g}}\right] \mathbf{n} \otimes \mathbf{n}_0, \quad (3.6)$$

and of the elastic left Cauchy-Green tensor $\mathbf{b}^e = \mathbf{F}^e \cdot \mathbf{F}^{e t}$,

$$\mathbf{b}^e = \frac{1}{\vartheta^g} \mathbf{b} + \left[1 - \frac{1}{\vartheta^g}\right] \mathbf{n} \otimes \mathbf{n}. \quad (3.7)$$

Here, $\mathbf{b} = \mathbf{F} \cdot \mathbf{F}^t$ is the total left Cauchy-Green tensor and $\mathbf{n} = \mathbf{F} \cdot \mathbf{n}_0$ is the deformed skin normal, which is no longer a unit vector. To focus on the effect of growth, we neglect the skin's collagenous microstructure and the associated anisotropy [38, 116]. Accordingly, we approximate its constitutive response as isotropically elastic, and characterize it through the following Helmholtz free energy function parameterized exclusively in terms of the reversible elastic part of the deformation,

$$\psi = \frac{1}{2} \lambda \ln^2(J^e) + \frac{1}{2} \mu [\mathbf{b}^e : \mathbf{i} - 3 - 2 \ln(J^e)]. \quad (3.8)$$

Here, \mathbf{i} denotes the spatial unit tensor. Motivated by our histological analysis in Section 3.2, we assume that the newly grown skin has the same microstructure, density, and stiffness, as the original native tissue [22, 36]. This implies that we can derive the Kirchhoff stress $\boldsymbol{\tau}$ from the standard Coleman-Noll evaluation of the dissipation inequality for open systems [72, 112],

$$\boldsymbol{\tau} = 2 \frac{\partial \psi}{\partial \mathbf{b}^e} \cdot \mathbf{b}^e = [\lambda \ln(J^e) - \mu] \mathbf{i} + \mu \mathbf{b}^e. \quad (3.9)$$

Next, we specify the evolution of area growth ϑ^g , which we model as a strain-driven process [83] using the following equation,

$$\dot{\vartheta}^g = k^g \phi^g. \quad (3.10)$$

Here we have introduced the weighting function

$$k^g = \frac{1}{\tau} \left[\frac{\vartheta^{\max} - \vartheta^g}{\vartheta^{\max} - 1} \right]^\gamma \quad (3.11)$$

to control unbounded growth [71, 139]. It has three well-defined material parameters, the maximum possible area growth ϑ^{\max} , the growth speed τ , and the nonlinearity parameter γ [87, 226]. In addition, we have introduced the growth criterion ϕ^g driven by the elastic area stretch ϑ^e ,

$$\phi^g = \langle \vartheta^e - \vartheta^{\text{crit}} \rangle = \langle \vartheta / \vartheta^g - \vartheta^{\text{crit}} \rangle. \quad (3.12)$$

The Macaulay brackets $\langle \circ \rangle$ ensure that growth is only activated if the elastic area stretch $\vartheta^e = \vartheta / \vartheta^g$ exceeds a critical physiological limit ϑ^{crit} . Here we have adopted a phenomenological approach to introduce a stretch-driven evolution equation for the growth tensor \mathbf{F}^g based on clinical observations [22]. Alternatively, we could have used thermodynamical considerations to formulate evolution equations for growth with the Mandel stress [62] or higher order gradients [48] as driving forces.

3.4 Computational Modeling Of Growing Skin

To solve the nonlinear finite element equations for stretch-induced membrane growth, we implement the growth model as a user subroutine into the commercial implicit finite element solver

Abaqus/Standard Version 6.12 [1]. We introduce the area growth ϑ^g as an internal variable, and solve its evolution equation (3.10) locally at the integration point level. We approximate the growth rate $\dot{\vartheta}^g$ through a finite difference approximation,

$$\dot{\vartheta}^g = [\vartheta^g - \vartheta_n^g] / \Delta t, \quad (3.13)$$

where $\Delta t = t - t_n$ denotes the current time increment. We apply an implicit time integration scheme and reformulate the evolution equation (3.10) with the help of equation (3.13), introducing the discrete residual R^ϑ in terms of the unknown area growth ϑ^g ,

$$R^\vartheta = \vartheta^g - \vartheta_n^g - k^g \phi^g \Delta t \doteq 0. \quad (3.14)$$

To solve this nonlinear equation we apply a local Newton iteration. Within each iteration step, we calculate the linearization of the residual R^ϑ with respect to the current area growth ϑ^g ,

$$K^\vartheta = \frac{\partial R^\vartheta}{\partial \vartheta^g} = 1 - \left[\frac{\partial k^g}{\partial \vartheta^g} \phi^g + k^g \frac{\partial \phi^g}{\partial \vartheta^g} \right] \Delta t. \quad (3.15)$$

Here, $\partial k^g / \partial \vartheta^g = -\gamma k^g / [\vartheta^{\max} - \vartheta^g]$ and $\partial \phi^g / \partial \vartheta^g = -\vartheta / \vartheta^{g2}$ denote the linearizations of the weighting function and of the growth criterion introduced in equations (3.11) and (3.12). Within each Newton iteration, we update the unknown area growth

$$\vartheta^g \leftarrow \vartheta^g - R^\vartheta / K^\vartheta, \quad (3.16)$$

until we achieve local convergence, i.e., until the absolute value of the growth update $\Delta \vartheta^g = -R^\vartheta / K^\vartheta$ reaches a user-defined threshold value. Once we have determined the current area growth ϑ^g from equation (3.16), we can successively determine the growth tensor \mathbf{F}^g from equation (3.4), the elastic tensor $\mathbf{F}^e = \mathbf{F} \cdot \mathbf{F}^g^{-1}$ from equation (3.6), the elastic left Cauchy-Green tensor $\mathbf{b}^e = \mathbf{F}^e \cdot \mathbf{F}^{e\text{t}}$ from equation (3.7), the Kirchhoff stress $\boldsymbol{\tau}$ from equation (3.9), and, finally, the fourth-order tensor of the Eulerian constitutive moduli [176],

$$\mathbf{c} = 4 \mathbf{b}^e \cdot \frac{\partial^2 \psi}{\partial \mathbf{b}^e \otimes \mathbf{b}^e} \cdot \mathbf{b}^e = \mathbf{c}^e + \mathbf{c}^g. \quad (3.17)$$

The first term, the Hessian of the free energy function at constant growth \mathbf{F}^g , defines the standard elastic constitutive moduli,

$$\begin{aligned} \mathbf{c}^e &= 4 \mathbf{b}^e \cdot \frac{\partial^2 \psi}{\partial \mathbf{b}^e \otimes \mathbf{b}^e} \cdot \mathbf{b}^e \Big|_{\mathbf{F}^g = \text{const}} \\ &= \lambda \mathbf{i} \otimes \mathbf{i} + [\mu - \lambda \ln(J^e)] [\mathbf{i} \otimes \mathbf{i} + \mathbf{i} \otimes \mathbf{i}]. \end{aligned} \quad (3.18)$$

Here we have used the common abbreviations, $\{\bullet\bar{\otimes}\circ\}_{ijkl} = \{\bullet\}_{ik} \{\circ\}_{jl}$ and $\{\bullet\otimes\circ\}_{ijkl} = \{\bullet\}_{il} \{\circ\}_{jk}$, for the non-standard fourth order products. The second term, the Hessian of the free energy function at constant deformation \mathbf{F} , defines the correction of the constitutive moduli due to growth [225],

$$\begin{aligned} \mathbf{c}^g &= 4 \mathbf{b}^e \cdot \frac{\partial^2 \psi}{\partial \mathbf{b}^e \otimes \mathbf{b}^e} \cdot \mathbf{b}^e \Big|_{\mathbf{F}=\text{const}} \\ &= -\frac{1}{\vartheta^g} \frac{k^g}{3K^g} \Delta t [\lambda \vartheta^g \mathbf{i} + \mu [\mathbf{b} - \mathbf{n} \otimes \mathbf{n}]] \\ &\quad \otimes [\vartheta \mathbf{i} - J^2 / \vartheta [\mathbf{F}^{-t} \cdot \mathbf{n}_0] \otimes [\mathbf{F}^{-t} \cdot \mathbf{n}_0]]. \end{aligned} \quad (3.19)$$

Rather than working directly with the Kirchhoff stress (3.9) and with the constitutive moduli (3.17), the user-defined subroutine in Abaqus/Standard utilizes the Cauchy or true stress, $\boldsymbol{\sigma} = \boldsymbol{\tau} / J$,

$$\boldsymbol{\sigma}^{\text{abaqus}} = [[\lambda \ln(J^e) - \mu] \mathbf{i} + \mu \mathbf{b}^e] / J, \quad (3.20)$$

and the Jauman rate of the Kirchhoff stress divided by the Jacobian, which requires the following modification of the tangent moduli [1, 171],

$$\mathbf{c}^{\text{abaqus}} = [\mathbf{c} + \frac{1}{2} [\boldsymbol{\tau} \bar{\otimes} \mathbf{i} + \mathbf{i} \bar{\otimes} \boldsymbol{\tau} + \boldsymbol{\tau} \otimes \mathbf{i} + \mathbf{i} \otimes \boldsymbol{\tau}]] / J. \quad (3.21)$$

The local stress $\boldsymbol{\sigma}^{\text{abaqus}}$ of equation (3.20) and the local tangent moduli $\mathbf{c}^{\text{abaqus}}$ of equation (3.21) enter the righthand side vector and the iteration matrix of the global Newton iteration. Upon its convergence, we store the current area growth ϑ^g locally at the integration point level.

3.5 Simulation Of Growing Skin

To explore the effects of skin growth, we simulate the process of controlled tissue expansion with multiple filling points in time, first in an idealized square skin sample and then in a patient-specific pediatric scalp.

3.5.1 Skin growth of an idealized square skin sample

For the first problem, we virtually implant expanders with four different shapes in the subcutaneous pocket underneath the dermis. We systematically increase the tissue stretch by gradually increasing the filling volume of all four expanders. To model the epidermis and the dermis, we discretize a $10 \times 10 \text{ cm}^2$ flat sheet, 0.2 cm thick, with $33 \times 33 \times 2 = 2,178$ C3D8 eight-noded linear brick elements, corresponding to a total of 3,468 nodes and 10,404 degrees of freedom. We model the elastic response as Neo-Hookean according to equations (3.8) and (3.9) with Lamé parameters $\lambda = 0.5440 \text{ MPa}$ and $\mu = 0.1785 \text{ MPa}$ [161], and the growth response as transversely isotropic and strain driven according to equations (3.10), (3.11), and (3.12) with a maximum growth of $\vartheta^{\text{max}} = 2.4$, a growth speed of

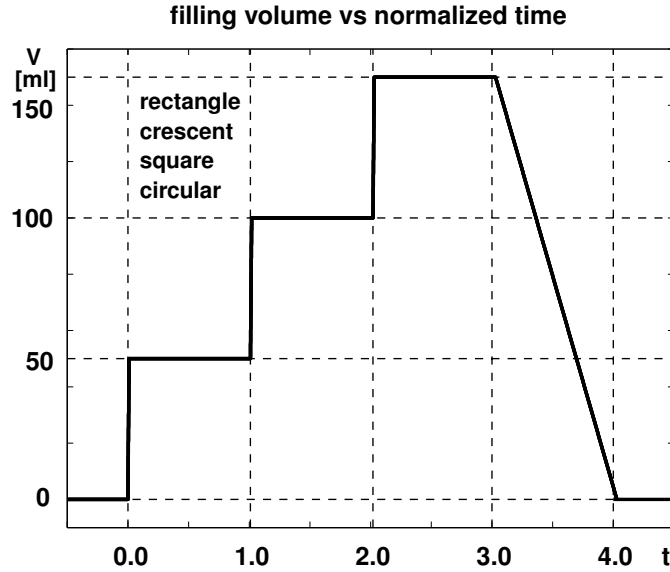


Figure 3.5: Skin growth upon tissue expansion. The filling volume of all four expanders, rectangular, crescent-shaped, square, and circular, is gradually increased by 150 ml in three steps of 50 ml each, and then gradually removed.

$\tau = 10$, a growth nonlinearity of $\gamma = 2$, and a critical growth threshold of $\vartheta^{\text{crit}} = 1.1$ [225]. To model the tissue expander itself, we introduce a fluid-filled cavity with a base area of 36 cm^2 , discretized with S3R and S4R shell elements. We model its elastic response using the material parameters of silicone [143] and discretize the fluid cavity with the same nodes and connectivity, but with F3D3 and F3D4 fluid elements. To allow the skin to slide freely along the expander we model their interaction as frictionless contact. We apply homogeneous Dirichlet boundary conditions to all neighboring nodes not involved in the expansion procedure.

Figure 3.5 displays the loading history for all four expanders: rectangular, crescent-shaped, square, and circular. We inflate each expander by gradually increasing its filling volume in three steps of 50 ml. After each filling step, we allow the skin to grow and establish a new equilibrium state before applying the next filling step. After three steps, we gradually release the entire filling volume to remove the expander.

Figure 3.6 displays the evolution of the fractional area gain, i.e., the net integral of skin growth, scaled by the initial base surface area, for all four expanders. Upon increasing the expander volume, the skin stretch exceeds the critical physiological threshold ϑ^{crit} and triggers the skin area to grow. The area increases gradually until growth has converged towards the biological equilibrium state. At this point, the elastic area stretch $\vartheta^e = \vartheta/\vartheta^g$ has gradually returned to its physiological threshold value ϑ^{crit} . When subject to a new filling increment, the procedure repeats itself accordingly. The skin area above the four expanders increases on average by $\sim 31\%$ in the first step, $\sim 46\%$ in the

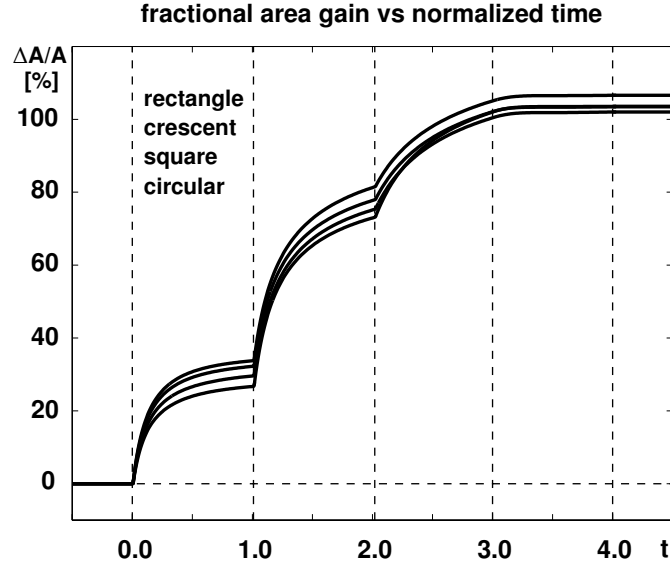


Figure 3.6: Skin growth upon tissue expansion. The area above all four expanders increases by $\sim 31\%$ in the first step, by $\sim 46\%$ in the second step, by $\sim 25\%$ in the third step, and remains constant upon expander removal. The rectangular expander initiates the largest amount of growth, followed by the crescent-shaped, square, and circular expanders.

second step, and $\sim 25\%$ in the third step. This illustrates the nonlinear nature of the growth process. When the filling volume is removed, the fractional area gain remains constant. This illustrates the irreversible nature of the growth process. At the end of the procedure, the rectangular expander has initiated the largest amount of fractional area growth with 1.0659, followed by the crescent-shaped expander with 1.0355, the square expander with 1.0201, and the circular expander with 1.0343. For all four expanders, skin has more than doubled its initial area, i.e., it has grown by more than 36 cm^2 .

Figure 3.7 displays the evolution of the expander pressure for all four expanders. The increase in expander volume at the beginning of each filling step is associated with an instant increase in expander pressure and a gradual relaxation towards the homeostatic equilibrium state. Since we fill the expander with a constant volume, the total skin area stretch $\vartheta = \vartheta^e \vartheta^g$ remains constant within each step. As the skin flap grows, the area growth ϑ^g increases and the elastic area stretch ϑ^e decreases. Since the stresses in the growing skin are a function of the elastic strains alone, the skin stresses decrease accordingly. This implies that the pressure induced by a constant filling volume decreases over time converging towards an equilibrium state. This equilibrium pressure increases nonlinearly with the filling volume taking average values of $0.654 p^{\max}$ in the first step, $0.816 p^{\max}$ in the second step, and $0.828 p^{\max}$ in the third step, before returning back to $0.000 p^{\max}$ after expander removal. Because the filling pressure is not only equilibrated by the stresses in the skin, but also by the stresses in the expander, which increase with increased filling volume, the equilibrium

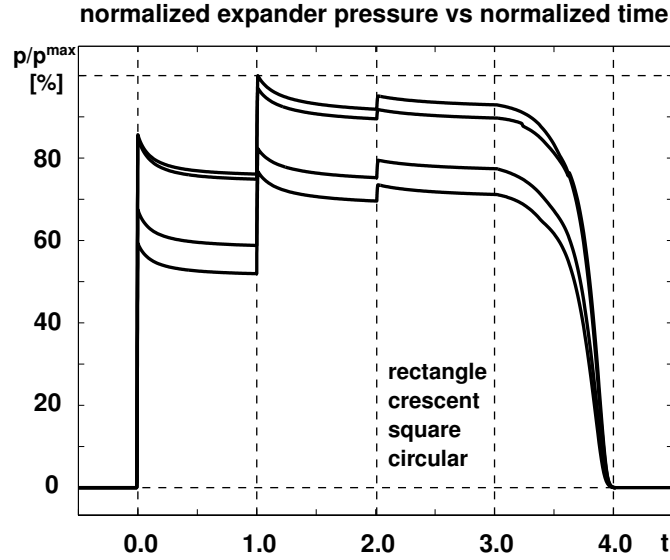


Figure 3.7: Skin growth upon tissue expansion. The expander pressure of all four expanders increases instantly upon inflation and relaxes gradually as skin grows in area and the elastic strain decreases. The rectangular expander is subject to the largest pressured, followed by the crescent-shaped, square, and circular expanders.

pressure increases with volume. The rectangular expander is subject to the largest pressure with a maximum value of 0.3752 MPa, followed by the crescent-shaped expander with 0.3637 MPa, the square expander with 0.3087 MPa, and circular expander with 0.2879 MPa.

Figure 3.8 displays the spatio-temporal evolution of the growth multiplier ϑ^g for the rectangular, crescent-shaped, square, and circular expanders, from top to bottom. The individual snapshots correspond to the converged equilibrium states for filling volumes of 50 ml, 100 ml, and 150 ml, and to the deflated state with the filling volume reduced to 0 ml, from left to right. Skin growth displays significant regional variations. Largest growth takes place in the center region with values up to $\vartheta^g = 2.25$, shown in red, indicating that the initial area has more than doubled in size. Smallest growth takes place along the expander edges with values of $\vartheta^g = 1.00$, shown in blue, indicating that no growth has taken place at all.

Figure 3.9 displays the spatio-temporal evolution of the normalized von Mises stress σ/σ^{\max} for the rectangular, crescent-shaped, square, and circular expanders, from top to bottom. The individual snapshots correspond to the converged equilibrium states for filling volumes of 50 ml, 100 ml, and 150 ml, and to the deflated state with the filling volume reduced to 0 ml, from left to right. To illustrate the individual skin expanders, we have virtually removed the lower corner of the skin patch. For the same filling volume and the same base surface area, the rectangular expander initiates the largest stresses, followed by the crescent-shaped, square, and circular expanders. Stresses display

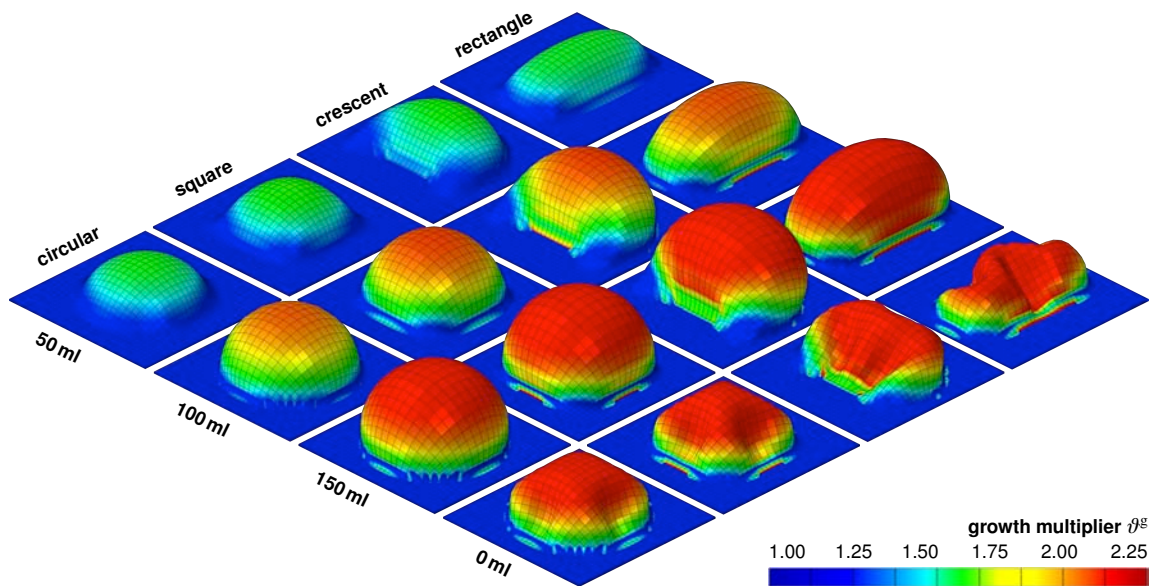


Figure 3.8: Skin growth upon tissue expansion. Spatio-temporal evolution of growth multiplier ϑ^g for rectangular, crescent-shaped, square, and circular expanders, from top to bottom. Snapshots correspond to converged equilibrium states for filling volumes of 50 ml, 100 ml, and 150 ml, and to deflated state with filling volume of 0 ml, from left to right. The color code illustrates the evolution of the growth multiplier ϑ^g , ranging from $\vartheta^g = 1.00$ for the initial ungrown skin, shown in blue, to $\vartheta^g = 2.25$ for the fully grown state, shown in red. Skin growth displays significant regional variations with largest values in the center region and smallest values along the expander edges.

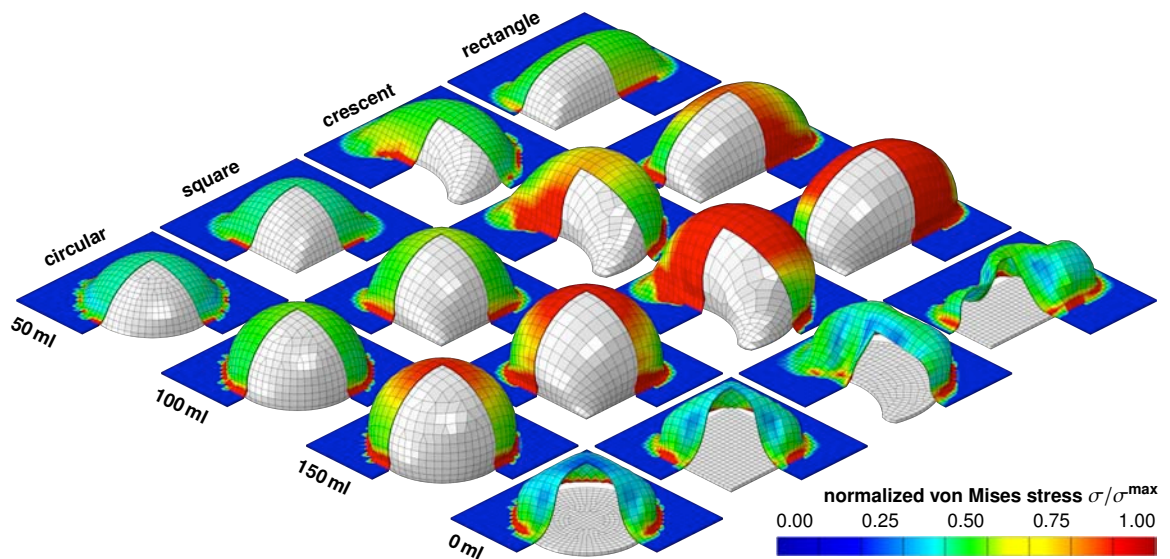


Figure 3.9: Skin growth upon tissue expansion. Spatio-temporal evolution of normalized von Mises stress σ/σ^{\max} for rectangular, crescent-shaped, square, and circular expanders, from top to bottom. Snapshots correspond to converged equilibrium states for filling volumes of 50 ml, 100 ml, and 150 ml, and to deflated state with filling volume of 0 ml, from left to right. Under the same filling volume and the same base surface area, the rectangular expander initiates the largest stresses, followed by the crescent-shaped, square, and circular expanders. The color code illustrates the evolution of the normalized stress σ/σ^{\max} , ranging from $\sigma/\sigma^{\max} = 0.00$ for the initial ungrown skin, shown in blue, to $\sigma/\sigma^{\max} = 1.00$ for the fully grown state, shown in red.

significant regional variations. Largest stresses are located in the center region and along the expander edges, shown in red. Moderate stresses are located at the expander sides, shown in green. No stresses occur in the unexpanded regions, shown in blue.

3.5.2 Skin growth of a pediatric scalp

For the second problem, we closely follow a clinical tissue expansion protocol and simulate skin growth in the scalp of the pediatric patient shown in Figure 3.1. We virtually insert a rectangular expander with a base surface area of $14 \times 10 \text{ cm}^2$ in a subcutaneous pocket of the frontoparietal scalp. The expander has a filling capacity of 450 ml, which we reach gradually by increasing the filling volume in three consecutive steps of 150 ml each. To model the epidermis and the dermis, we discretize the skin on top of the expander as a $14 \times 10 \text{ cm}^2$ large, 0.2cm thick layer with $45 \times 32 \times 2 = 2,880$ C3D8 eight-noded linear brick elements, corresponding to a total of 4,554 nodes and 13,662 degrees of freedom. Similar to the idealized square skin sample in Section 3.5.1, we model the elastic response as Neo-Hookean according to equations (3.8) and (3.9) with Lamé parameters $\lambda = 0.5440 \text{ MPa}$ and $\mu = 0.1785 \text{ MPa}$ citepamplona09, and the growth response as transversely isotropic and strain driven according to equations (3.10), (3.11), and (3.12) with a maximum growth of $\vartheta^{\max} = 2.4$, a growth speed of $\tau = 10$, a growth nonlinearity of $\gamma = 2$, and a critical growth threshold of $\vartheta^{\text{crit}} = 1.1$ [225]. We model the skin expander as a fluid-filled cavity with a base area of $14 \times 10 \text{ cm}^2$, discretized with 638 S4R shell elements, corresponding to a total of 640 nodes and 1,920 degrees of freedom. We model its elastic response using the material parameters of silicone [143] and discretize the fluid cavity with the same nodes and connectivity, but with F3D4 fluid elements. We allow the skin to slide freely along the expander and model the skin-expander interaction as frictionless contact. We fix all nodes that are not involved in the expansion procedure using homogeneous Dirichlet boundary conditions.

Figure 3.10 displays the spatio-temporal evolution of the growth multiplier $\vartheta^{\mathcal{E}}$ immediately after filling, bottom row, and after converged growth, top row. The individual snapshots correspond to the initial filled states and the converged homeostatic equilibrium states for filling volumes of 150 ml, 300 ml, and 450 ml, and to deflated state with filling volume of 0 ml, from left to right. Similar to the idealized square skin sample in Section 3.5.1, skin growth displays regional variations in magnitude with largest values in the center region, shown in red, and smallest values along the expander edges, shown in blue.

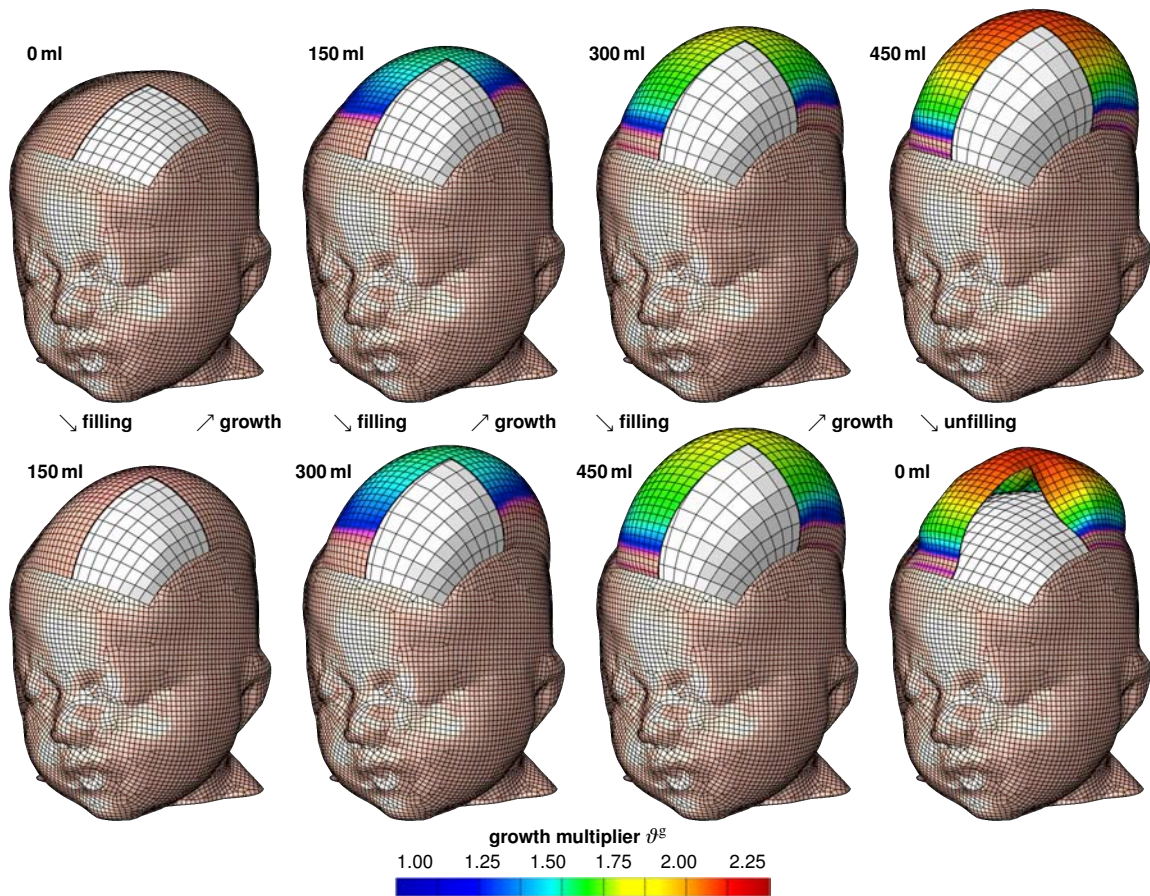


Figure 3.10: Skin growth upon tissue expansion in pediatric scalp reconstruction. Spatio-temporal evolution of growth multiplier ϑ^g immediately after filling, bottom row, and after converged growth, top row. Snapshots correspond to filling volumes of 150 ml, 300 ml, and 450 ml, and to deflated state with filling volume of 0 ml, from left to right. The color code illustrates the evolution of the growth multiplier ϑ^g , ranging from $\vartheta^g = 1.00$ for the initial ungrown skin, shown in blue, to $\vartheta^g = 2.25$ for the fully grown state, shown in red. Skin growth displays significant regional variations with largest values in the center region and smallest values along the expander edges.

3.6 Discussion

3.6.1 Discussion of results

We have presented a constitutive model for overstretch-induced skin growth, which allows us to predict chronic changes in stress, strain, and area gain in thin biological membranes. Upon expander inflation, our model predicts an acute increase in the total area stretch $\vartheta = \vartheta^e \vartheta^g$, associated with an acute decrease in skin thickness. Initially, in the absence of growth $\vartheta^g = 0$, the total stretch is carried exclusively by the elastic stretch $\vartheta^e = \vartheta$, which increases acutely. Since the skin stress $\boldsymbol{\tau}(\mathbf{b}^e)$ is a function of the elastic part of the deformation only, the acute increase in elastic stretch induces an acute increase in tissue stress, and accordingly, an acute increase in the expander pressure, see Figure 3.7.

Over time, our model predicts a chronic increase in area growth ϑ^g , see Figures 3.6, 3.9, and 3.10. Since we drive expander inflation by controlling the filling volume, as shown in Figure 3.5, the total area stretch $\vartheta = \vartheta^e \vartheta^g$ remains constant between two filling sessions. Accordingly, a chronic increase of the area growth $\vartheta^g \uparrow$ implies a chronic decrease of the elastic area stretch $\vartheta^e \downarrow$, which gradually returns to its homeostatic equilibrium value $\vartheta^e \rightarrow \vartheta^{\text{crit}}$. Similarly, the model predicts a gradual return of the skin thickness to its initial baseline value. The chronic decrease of the elastic stretch induces a chronic decrease in the skin stress $\boldsymbol{\tau}(\mathbf{b}^e)$, which manifests itself in a decrease in expander pressure, see Figure 3.7. Rheologically, this chronic response resembles the phenomenon of relaxation. However, the expander pressure p/p^{max} never fully returns to zero because of the inherent resistance of the silicone expander itself.

Upon expander deflation, the elastic strain decreases below the critical threshold value $\vartheta^e < \vartheta^{\text{crit}}$ associated with an acute arrest of further growth $\vartheta^g = \text{const}$, see Figures 3.6 and 3.10, bottom right. Deflation is associated with an acute retraction of the reversible elastic area stretch back to its initial baseline value of $\vartheta^e \rightarrow 1.0$ and an acute release of the expander pressure $p/p^{\text{max}} \rightarrow 0$, see Figure 3.7. Although the expander volume is fully released at the end of the procedure, the heterogeneity of the growth process leaves some residual elastic deformation, which manifests itself in residual stresses upon expander removal, see Figure 3.9, right, and Figure 3.10, bottom right.

In space, our model predicts regional variations in the amount of growth with larger values in the center region and smaller values in the periphery, see Figures 3.8 and 3.10. Expander inflation causes largest area strains in the center region. This triggers a heterogeneity of the growth process. In the center region, skin more than doubles its initial area with $\vartheta^g \rightarrow \vartheta^{\text{max}}$, while the amount of growth gradually decays towards the expander edges.

3.6.2 Comparison with the literature

The characteristic features predicted by our model are in excellent agreement with the observed phenomena during tissue expansion in animals [22, 34] and in humans [83, 162]. In the tissue expansion literature, our decomposition of the deformation gradient into reversible and irreversible parts $\mathbf{F} = \mathbf{F}^e \cdot \mathbf{F}^g$ is referred to as mechanical creep and biological creep [98] or, more illustratively, as loan and dividend [16]. What is referred to as stretch back in the tissue engineering literature [212] is associated with the reversible elastic part of the deformation, which is released upon expander removal. To account for this reversible deformation, empirical guidelines suggest to select an expander size with a base surface area which is 2.5 larger than the defect area to be closed [98]. A quantitative study of skin growth in pigs recommends to multiply the required surface area with an empirical correction factor. Recommended correction factors range from 6.00 to 4.50 and 3.75 for the circular, crescent shaped, and rectangular expanders, respectively [212]. In agreement with our findings in Figures 3.6 and 3.8, these correction factors suggest that the net area gain is greatest for the rectangular expander, followed by the crescent-shaped and circular expanders [34, 212]. A comparison of the fractional area gain $\Delta A/A$ revealed values ranging from 35% to 137% [98]. Our fractional area gain between 100% and 110% as displayed in Figure 3.6 is well within this range.

In one of the earliest quantitative studies of controlled tissue expansion in guinea pigs, it was argued that stretching skin stimulates cell proliferation just sufficient to relieve tension [65]. This is in agreement with the rheological analogy of stress relaxation [38], which we observed in Figure 3.7. In a chronic porcine model, the expander pressure was found to increase acutely, but returned to its homeostatic equilibrium state after a period of a few days [34]. The fact that this equilibrium state changes nonlinearly with the amount of filling was attributed to nonlinearities in the constitutive responses of both the expanded skin and the silicone expander itself [34]. This is in excellent agreement with our observations in Figure 3.7. Along the same lines, detailed thickness studies of expanded human skin revealed an initial epidermal thickening, dermal thinning, and subcutaneous thinning five months after expansion. However, the thicknesses of all three layers returned to their pre-expansion baseline values two years after the procedure had been completed [167, 168]. This is in agreement with the acute and chronic features predicted by our model, see Figure 3.7.

Controlled tissue expansion studies in rodents revealed a regional variation of skin growth with largest growth in the center region and smallest growth in the periphery [22]. The authors hypothesized that larger strains in the center region would trigger larger growth. This feature is nicely reflected by our model, in which the evolution of area growth in equation (3.10) is directly correlated to the amount of overstretch through the growth criterion in equation (3.12). Figures 3.8 and 3.10 clearly support the experimental observations of a heterogeneous growth process with larger values in the center region and smaller values in the periphery [22].

We have implemented our growth model as user-defined constitutive subroutine into the general purpose finite element program Abaqus/Standard Version 6.12 [1]. Instead of using the explicit

version Abaqus/Explicit, as previously proposed for tissue expansion in breast reconstruction [160], we have used the implicit version of the program. To ensure optimal convergence of the global Newton iteration, our implicit user subroutine not only has to provide the constitutive equation for the Cauchy stress σ^{abaqus} from equation (3.20), but also the local tangent moduli $\mathbf{c}^{\text{abaqus}}$ from equation (3.21).

While the model for breast reconstruction can only account for mechanical creep in terms of the reversible deformation [160], our model is also capable of predicting biological creep in terms of irreversible deformation in the form of growth. The very first finite element model for biological creep, or rather skin growth, was also realized within Abaqus/Explicit, however only for axisymmetric circular expander geometries and restricted to an explicit time integration [193]. While our first prototype finite element models for growth were fully three dimensional and implicit [36, 225], this manuscript documents our first implementation of the model into a commercially available finite element package. This allows us to use the entire infrastructure of a multi-purpose finite element program, including features such as the fluid filled cavity to model the expander [162], and frictionless sliding to model the expander-skin interface [1]. Our first prototype simulations did not discretize the expander explicitly, but were rather entirely pressure driven [38, 226]. The current model represents a significant advancement of our previous attempts to model skin expansion in a clinical setting, since it allows us to model expander inflation by precisely controlling filling volumes according to multi-step clinical filling protocols [189]. Driving tissue expansion through filling volume rather than filling pressure mimics the clinical procedure more closely [163, 164], and will eventually allow us to directly optimize clinical process parameters. Overall, our new model nicely captures the essential features of overstretch-induced area growth in skin, not only acutely but also chronically.

3.6.3 Future challenges

We believe that the proposed model is a successful first step towards studying the interaction of mechanics and biology during skin growth. Nevertheless, several open challenges need to be addressed in the future to turn this first prototype model into a reliable predictive tool for clinical research.

From reductionist to holistic. First and foremost, to gain a full understanding of the complex behavior skin as a living system, it is important to explore and characterize skin across different spatial and temporal scales [99]. We need to appreciate that skin, as a living system, is more than just the sum of its parts [162]. Throughout the past century, we have gained valuable insight from both biochemical assays and mechanical testing [89]. However, it has only been within the past decade that we have started to decipher the active crosstalk between biology and mechanics [138]. The biomechanics of skin, i.e., the ways in which biology influences mechanical characteristics such as stress, strain, or energy, seem relatively well understood by now. The mechanobiology of skin, i.e., the ways in which mechanical forces, stretch, or stretch rates can manipulate biological systems, are

a lot less well characterized [55]. At this point, to gain a complete picture of the complex nature of skin as a living system, it seems that our efforts have to move from a classical reductionist to a more holistic approach. Computational modeling could be a valuable tool to integrate information across the scales and, more importantly, across individual disciplines [227]. Specifically, in terms of our growth model, a more holistic approach would imply tying the growth law in equation (3.4) more closely to the underlying mechanobiology described Section 3.1. Time sequences of gene expression assays and immunohistochemistry of growing tissue samples could help to identify the mechanisms that trigger skin growth at the molecular and cellular levels [203]. Eventually, this information could help to replace the phenomenological evolution equation for the growth tensor (3.4) by a discrete network of mechanotransduction pathways of specific extracellular and intracellular events [191]. For example, a more mechanistic model could incorporate pathways from polymer synthesis to the deposition of large bundles of compacted immature collagen at the microstructural level [19], which manifest themselves macrostructurally in the reorientation of the collagen network and through a realignment the direction of maximum principal strains [88, 119].

From qualitative to quantitative. Using mathematical modeling to better understand living systems emphasizes the need to move from qualitative to quantitative biochemical assays and biomechanics testing [6]. In this endeavor, mathematical modeling could help to specify and redesign biochemical assays with well-defined quantitative readouts. Ideally, a hybrid computational-experimental approach would help to identify quantitative biochemical metrics of growth, which could directly feed into discrete mechanotransduction network models of interconnected positive and negative feedback loops. These discrete network models would replace the phenomenological evolution equation for area growth (3.10) by a biochemically-motivated mechanistic evolution law with well-defined parameters with a clear physiological interpretation [151]. Specifically, in terms of our growth model, a more quantitative approach could allow us to correlate our phenomenological material parameters, for example the growth speed τ , to metabolic pathways and limit their range by metabolic constraints [226].

From ex vivo to in vivo. To better characterize the interaction of mechanics and biology, there is an ongoing need to move from the ex vivo characterization of explanted tissue samples to the in vivo characterization of skin as a living system [3]. Specifically, in terms of our growth model, an in vivo characterization would help us to refine the constitutive equations for the elastic baseline response [121], which we simplified to be isotropic Neo-Hookean. A better candidate might be a multiple-constituent anisotropic skin model [133], with in-plane anisotropy introduced through a pronounced stiffness along Langer's lines [117, 135], which we have successfully combined with the proposed growth model in the past [38]. Calibrating our model with real in vivo data would allow us to include the effects of prestrain and residual stress [197]. Recent studies have shown that both play a critical role in collagenous thin biological membranes [7, 79]. To incorporate prestrain and residual stress within the context of finite deformations, we can introduce an additional mapping from a

relaxed ex vivo to the prestrained in vivo configuration through another second-order tensor [150]. We have recently shown that incorporating prestrain of only 20% to 30% can decrease the in vivo tissue stiffness by three to four orders of magnitude [178].

From acute to chronic. In the current model, the long-term response growing of skin is not yet calibrated in time. We have assumed that chronic growth between two filling increments takes place within a normalized time interval from zero to one. In reality, growth periods range from the order of days in rodents [22] to weeks in pigs [212] and humans [83]. In an ideal experimental setting, data would be acquired not only acutely but also chronically [177], and the relevant growth metrics would be quantified at multiple points in time [162]. Specifically, in terms of our growth model, quantitative chronic studies would allow us to calibrate the adaptation speed τ and the shape of the growth curve γ [225, 226], or the corresponding time parameters of more mechanistic biochemically driven evolution equations.

3.7 Conclusion

We have demonstrated the mathematical modeling and computational simulation of skin growth by mechanical overstretch. Previous models of skin growth have controlled overstretch by directly applying the expander pressure without discretizing the expander itself. Here, we have controlled the amount of overstretch by gradually filling a virtually implanted tissue expander. In contrast to previous models, this allows us now to predict the rheological effect of stress relaxation, i.e., a chronic increase in skin area at constant stretch, associated with a chronic decrease in elastic stretch, stress, and pressure. While it is virtually impossible to measure stresses in living biological membrane in vivo, the precise knowledge of skin stress and expander pressure is clinically critical to optimize capillary refill, minimize tissue necrosis, and maximize patient comfort. Once calibrated with long-term in vivo data, our model will be capable of predicting stress, pressure, strain, and area gain in thin biological membranes exposed to mechanical overstretch. It can serve as a valuable tool to rationalize clinical process parameters such as expander geometry, expander size, filling volume, filling pressure, and inflation timing. The proposed model for skin growth can easily be generalized to explore the physiology and pathology of stretch-induced growth in other living systems such as the bladder, intestine, ureter, blood vessels, muscles, and nerves, which display similar structural characteristics.

Acknowledgements

We gratefully acknowledge the Holland family for proofreading the manuscript. This study was supported by the National Science Foundation CAREER award CMMI 0952021, by the National Science Foundation INSPIRE grant 1233054, and by the National Institutes of Health grant U54

GM072970.

Chapter 4

Chronic muscle lengthening through sarcomerogenesis

Abstract

Skeletal muscle responds to passive overstretch through sarcomerogenesis, the creation and serial deposition of new sarcomere units. Sarcomerogenesis is critical to muscle function: It gradually re-positions the muscle back into its optimal operating regime. Animal models of immobilization, limb lengthening, and tendon transfer have provided significant insight into muscle adaptation in vivo. Yet, to date, there is no mathematical model that allows us to predict how skeletal muscle adapts to mechanical stretch in silico. Here we propose a novel mechanistic model for chronic longitudinal muscle growth in response to passive mechanical stretch. We characterize growth through a single scalar-valued internal variable, the serial sarcomere number. Sarcomerogenesis, the evolution of this variable, is driven by the elastic mechanical stretch. To analyze realistic three-dimensional muscle geometries, we embed our model into a nonlinear finite element framework. In a chronic limb lengthening study with a muscle stretch of 1.14, the model predicts an acute sarcomere lengthening from $3.09\mu\text{m}$ to $3.51\mu\text{m}$, and a chronic gradual return to the initial sarcomere length within two weeks. Compared to the experiment, the acute model error was 0.00% by design of the model; the chronic model error was 2.13%, which lies within the range of the experimental standard deviation. Our model explains, from a mechanistic point of view, why gradual multi-step muscle lengthening is less invasive than single-step lengthening. It also explains regional variations in sarcomere length, shorter close to and longer away from the muscle-tendon interface. Once calibrated with a richer data set, our model may help surgeons to prevent muscle overstretch and make informed decisions about optimal stretch increments, stretch timing, and stretch amplitudes. We anticipate our study to open new avenues in orthopedic and reconstructive surgery and enhance treatment for patients with ill proportioned limbs, tendon lengthening, tendon transfer, tendon tear, and chronically retracted muscles.

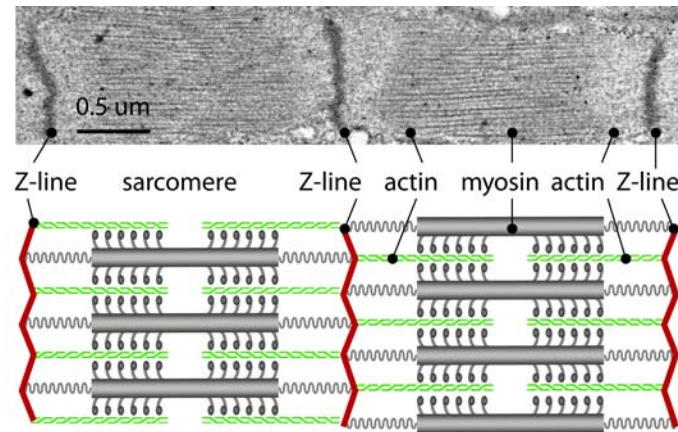


Figure 4.1: Sarcomere units in striated muscle. Sarcomeres consist of a parallel arrangement of thick filaments of myosin (gray) sliding along thin filaments of actin (green). They are embedded between Z-lines (red), which appear as dark lines under the transmission electron microscope. In healthy muscle, through the dynamic assembly and disassembly, individual sarcomere units maintain an optimal operating length. Adopted with permission from [71].

4.1 Introduction

Striated muscle displays the striking ability to rapidly adapt to changes in physiological requirements through the dynamic assembly and disassembly of its functional building blocks, the sarcomeres [33]. Sarcomeres are characterized through a parallel arrangement of thick filaments of myosin that slide along thin filaments of actin [93].

Figure 4.1 illustrates two sarcomere units embedded between neighboring Z-lines. Under the transmission electron microscope, Z-lines appear as dark lines giving the muscle its characteristic striated appearance [61]. The appropriate overlap of actin and myosin filaments is critical to active muscle contraction, and sarcomeres produce their maximum force at a characteristic optimal sarcomere length [76]. When stretched beyond the physiological limit, skeletal muscles responds through sarcomerogenesis [42], the creation and serial deposition of new sarcomere units [86], to gradually return into its optimal operating regime [216]. This dynamic adjustment is key to long-term regeneration and repair durability in orthopedic and reconstructive surgery. Typical examples are surgical limb lengthening, tendon lengthening, tendon transfer, or tendon reattachment after tendon tear.

Limb lengthening is a highly invasive surgical procedure to reconstruct or correct congenital and developmental deformities, post-traumatic injuries, regions of tumor removal, and short stature. Using the principle of distraction osteogenesis, the surgeon cuts the bone in two and gradually pulls apart the two ends, triggering new bone to form [42]. Figure 4.2 illustrates the procedure of limb lengthening through osteodistraction in the left forearm of an adult rabbit [144]. While the main

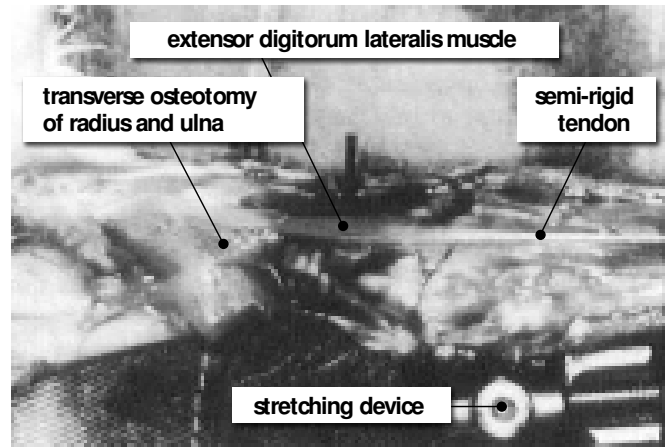


Figure 4.2: Stretching skeletal muscle. In a controlled limb lengthening model in rabbits, the radius and the ulna of the left forearm are lengthened by 4% inducing a stretch of $\lambda = 1.14$ in the extensor digitorum lateralis muscle. Chronic eccentric muscle growth through sarcomerogenesis is characterized in situ using light diffraction imaging. Adopted with permission from [144].

goal of osteodistraction is to lengthen the bone itself, it is key to the procedure that the surrounding muscle grows in parallel with the stretched bone. Contracture, the lack of appropriate muscle adaptation, is a major source of complication during limb lengthening [85]. Optimal results can be obtained by lengthening the bone at a rate of 1mm per day [42], up to no more than 20% of its initial length [85]. Although it is well accepted that mechanical factors play a limiting role in bone lengthening [41], to date, there are no mechanistic models that provide a scientific interpretation of these empirical guidelines.

In contrast to limb lengthening, tendon lengthening [12], tendon transfer [40], and tendon reattachment after tendon tear [70] are surgical procedures, which directly manipulate the muscle-tendon complex to correct posture or gait, and to improve or restore force generation. Typically, these corrections are performed in a single-step procedure, which permits the muscle to regain its original architecture [70]. Recent studies suggest that a restoration of normal architecture and physiological function might be possible through a gradual lengthening of the musculotendinous unit when stretched at a rate of 1mm per day [230]. While we can sufficiently well approximate the short-term response to these surgical procedures by kinematic models [13], we are currently unable to predict their long-term behavior through chronic muscle adaptation.

In the clinical community, the dynamic adaptation of skeletal muscle is widely known as muscle plasticity [33]. This term suggests that the deformations caused by chronic lengthening are inelastic, i.e., they do neither store energy, nor do they generate stress [71]. In the mechanics community, mathematical models for growing of soft biological tissues indeed originate from finite strain plasticity [125]. They define growth through an incompatible configuration [6], characterized through the

multiplicative decomposition of the overall deformation into a reversible elastic and an irreversible inelastic part [67, 183]. The irreversible part is represented through a second order growth tensor [151], which can be isotropic [87], transversely isotropic [36, 104], orthotropic [72], or generally anisotropic [149, 209] depending on the particular type of tissue. Its evolution can be driven by stress [118] or strain [225] again depending on the particular type of growth. Similar to cardiac muscle, skeletal muscle grows in a transversely isotropic pattern, along the fiber direction in response to passive mechanical stretch [72] and orthogonal to the fiber direction in response to active mechanical stress [176]. On the macroscopic scale, a passively stretched muscle grows eccentrically, i.e., it becomes longer, while an actively stressed muscle grows concentrically, i.e., it becomes thicker [197]. On the microscopic scale, passive stretch induces sarcomerogenesis, the serial deposition of sarcomere units, while active stress induces myofibrillogenesis, the parallel deposition of sarcomeres arranged in myofibrils [71, 101]. We have previously modeled both forms of growth in cardiac muscle [72] using generalized continuum theories with internal variables [62, 151]. However, to date, there is no mechanistic model to characterize growth in skeletal muscle using the nonlinear field theories of continuum mechanics.

Here we establish a mechanistic mathematical model for overstretch-induced eccentric skeletal muscle growth. The model is inherently multiscale, since it links macroscopic changes in elastic and inelastic muscle stretch to microscopic changes in sarcomere length and number. We illustrate the continuum theory of finite growth, adapt it to sarcomerogenesis, and embed it into a nonlinear finite element framework. We demonstrate that the model shows an excellent qualitative and quantitative agreement with experimentally measured sarcomere lengths and numbers in a chronic limb lengthening experiment.

4.2 Methods

In this section, we briefly summarize the continuum modeling of sarcomerogenesis and its computational realization within a nonlinear finite element environment.

Continuum modeling of sarcomerogenesis

To accurately represent the finite deformations during muscle stretching, we adopt the kinematics of finite growth, and introduce the deformation map φ , which, at any given time t , maps the material placement \mathbf{X} of a physical particle onto its spatial placement $\mathbf{x} = \varphi(\mathbf{X}, t)$. We then introduce the multiplicative decomposition of the deformation gradient [125],

$$\mathbf{F} = \nabla_{\mathbf{X}} \varphi = \mathbf{F}^e \cdot \mathbf{F}^g \quad (4.1)$$

into a reversible elastic part \mathbf{F}^e and an irreversible growth part \mathbf{F}^g [183]. Here, $\nabla\{\circ\} = \partial_{\mathbf{X}}\{\circ\}|_t$ denotes the gradient of a field $\{\circ\}(\mathbf{X}, t)$ with respect to the material placement \mathbf{X} at fixed time t . The Jacobian defines the overall change in tissue volume,

$$J = \det(\mathbf{F}) = J^e J^g \quad (4.2)$$

which we can equivalently decompose into a reversibly elastic volume change $J^e = \det(\mathbf{F}^e)$ and an irreversibly grown volume change $J^g = \det(\mathbf{F}^g)$. In muscle lengthening, growth is locally one dimensional, and the total muscle fiber stretch λ obeys a multiplicative decomposition similar to the deformation gradient itself [72]. We can interpret the total stretch λ as a product of the reversible elastic stretch λ^e and the irreversible growth stretch λ^g ,

$$\lambda = [\mathbf{n}_0 \cdot \mathbf{F}^t \cdot \mathbf{F} \cdot \mathbf{n}_0]^{1/2} = \lambda^e \lambda^g. \quad (4.3)$$

We can then express the growth tensor \mathbf{F}^g in terms of a single scalar-valued variable ϑ , which represents the number of sarcomeres along the fiber direction \mathbf{n}_0 in the undeformed reference configuration [71, 151],

$$\mathbf{F}^g = \mathbf{I} + [\vartheta - 1] \mathbf{n}_0 \otimes \mathbf{n}_0. \quad (4.4)$$

Since the muscle is not assumed to grow in the lateral direction, the serial sarcomere number ϑ is not only identical to the irreversible growth stretch λ^g , but also to the volume growth of the muscle, $\det(\mathbf{F}^g) = J^g$,

$$\vartheta = \lambda^g = \det(\mathbf{F}^g) = J^g. \quad (4.5)$$

Using the simple rank-one update structure of \mathbf{F}^g , we can apply the Sherman-Morrison formula to invert the growth tensor, $\mathbf{F}^{g-1} = \mathbf{I} + [1 - \vartheta] / \vartheta \mathbf{n}_0 \otimes \mathbf{n}_0$, and obtain an explicit representation of the elastic tensor, $\mathbf{F}^e = \mathbf{F} + [1 - \vartheta] / \vartheta \mathbf{n} \otimes \mathbf{n}$. Here, $\mathbf{n} = \mathbf{F} \cdot \mathbf{n}_0$ is the fiber direction in the deformed configuration. This allows us to explicitly introduce the elastic left Cauchy Green tensor

$$\mathbf{b}^e = \mathbf{F}^e \cdot \mathbf{F}^{et} = \mathbf{F} \cdot \mathbf{F}^t + \frac{1 - \vartheta^2}{\vartheta^2} \mathbf{n} \otimes \mathbf{n}. \quad (4.6)$$

To focus on the impact of growth, we assume the passive muscle to behave isotropically elastic within the loading range of interest. We introduce the following Helmholtz free energy function

$$\psi = \frac{1}{2} L \ln^2(J^e) + \frac{1}{2} G [\mathbf{b}^e : \mathbf{I} - 3 - 2 \ln(J^e)], \quad (4.7)$$

where L and G are the Lamé constants. We then evaluate the standard dissipation inequality to determine the Kirchhoff stress

$$\boldsymbol{\tau} = [L \ln(J^e) - G] \mathbf{I} + G \mathbf{b}^e. \quad (4.8)$$

This formulation implies that the newly created muscle will have the same microstructure, density, and stiffness, as the original, native tissue [230]. We model longitudinal muscle growth as a strain-driven process, and introduce the following evolution equation for the serial sarcomere number

$$\dot{\vartheta} = k(\vartheta) \phi(\lambda^e), \quad (4.9)$$

in which $k(\vartheta)$ is a weighting function and $\phi(\lambda^e)$ is a growth criterion similar to a yield function in the theory of plasticity. For the weighting function, we adopt a well-established functional form [139], which we rephrase here in a strain-driven format [71, 72] to control unbounded growth,

$$k = \frac{1}{\tau} \left[\frac{\vartheta^{\max} - \vartheta}{\vartheta^{\max} - 1} \right]^\gamma. \quad (4.10)$$

The adaptation speed τ and the shape parameter for the adaptation curve γ control the speed of adaptation [187, 225], and the maximum serial sarcomere number ϑ^{\max} limits the maximum sarcomere deposition upon growth [104]. For the growth criterion, we assume that growth is driven by the elastic muscle fiber stretch λ^e . Guided by experimental observations [42], we activate growth only if the elastic fiber stretch exceeds a critical physiological limit λ^{crit} ,

$$\phi = \langle \lambda^e - \lambda^{\text{crit}} \rangle = \langle \lambda / \vartheta - \lambda^{\text{crit}} \rangle. \quad (4.11)$$

where $\langle \circ \rangle$ denote the Macaulay brackets.

Computational modeling of sarcomerogenesis

To solve the nonlinear finite element equations of stretch-induced muscle lengthening, we implement the growth model in a custom-designed version of the multipurpose nonlinear finite element program FEAP [205]. To characterize the growth process at each instant in time, we introduce the serial sarcomere number ϑ as an internal variable, and solve the biological equilibrium equation (4.9) locally at the integration point level [87, 226]. At each discrete time step t , we determine the current serial sarcomere number ϑ for a given current deformation state \mathbf{F} and a given area growth ϑ_n from the previous time step t_n [71]. Accordingly, we introduce the following finite difference approximation for the material time derivative of the serial sarcomere number,

$$\dot{\vartheta} = [\vartheta - \vartheta_n] / \Delta t \quad (4.12)$$

where $\Delta t = t - t_n$ denotes the current time increment. In the spirit of implicit time stepping schemes, we now reformulate the evolution equation (4.9) with the help of equation (4.12) and introduce the

discrete residual R in terms of the unknown serial sarcomere number ϑ .

$$R = \vartheta - \vartheta_n - k \phi \Delta t \doteq 0 \quad (4.13)$$

We solve this nonlinear equation using a local Newton iteration [72]. Within each iteration step, we calculate the linearization of the residual R with respect to the serial sarcomere number ϑ ,

$$K = \frac{\partial R}{\partial \vartheta} = 1 - \left[\frac{\partial k}{\partial \vartheta} \phi + k \frac{\partial \phi}{\partial \vartheta} \right] \Delta t \quad (4.14)$$

in terms of the linearizations of the weighting function $\partial k / \partial \vartheta = \gamma k / [\vartheta - \vartheta^{\max}]$ and the growth criterion

$\partial \phi / \partial \vartheta = -\lambda / \vartheta^2$ introduced in equations (4.10) and (4.11), see [36, 72]. We iteratively update the unknown serial sarcomere number,

$$\vartheta \leftarrow \vartheta - R / K \quad (4.15)$$

until we achieve convergence, i.e., until the absolute value of the local growth update $\Delta \vartheta = -R / K$ is below a user-defined threshold value. Once we have iteratively determined the current serial sarcomere number ϑ , we can successively determine the growth tensor \mathbf{F}^g from equation (4.4), the elastic tensor $\mathbf{F}^e = \mathbf{F} \cdot \mathbf{F}^g^{-1}$, the Kirchhoff stress $\boldsymbol{\tau}$ from equation (4.8), and, finally, the fourth order tensor \mathbf{e} of the Eulerian constitutive moduli

$$\mathbf{e} = \mathbf{e}^e + \mathbf{e}^g. \quad (4.16)$$

The first term

$$\mathbf{e}^e = L \mathbf{I} \otimes \mathbf{I} + [G - L \ln(J^e)] [\mathbf{I} \overline{\otimes} \mathbf{I} + \mathbf{I} \underline{\otimes} \mathbf{I}] \quad (4.17)$$

defines that standard elastic constitutive moduli where we have used the common abbreviations $\{\bullet \overline{\otimes} \circ\}_{ijkl} = \{\bullet\}_{ik} \{\circ\}_{jl}$ and $\{\bullet \underline{\otimes} \circ\}_{ijkl} = \{\bullet\}_{il} \{\circ\}_{jk}$, for the non-standard fourth order products.

The second term

$$\mathbf{e}^g = -\frac{k}{\lambda \vartheta K} [L \mathbf{I} + 2G/\vartheta^2 \mathbf{n} \otimes \mathbf{n}] \otimes [\mathbf{n} \otimes \mathbf{n}] \Delta t \quad (4.18)$$

depends directly on the constitutive formulation for the Kirchhoff stress $\boldsymbol{\tau}$ in equation (4.8), indirectly on the particular format of the growth tensor \mathbf{F}^g in equation (4.4), on the algorithmic linearization of the time discrete evolution equation for the serial sarcomere number $\partial \vartheta / \partial \lambda$ in equation (4.15), and on the linearization of the determinant $2 \partial \lambda / \partial \mathbf{g}$ in equation (4.3). The local stress $\boldsymbol{\tau}$ of equation (4.8) and the local consistent tangent moduli \mathbf{e} of equation (4.16) enter the global righthand side vector and the global iteration matrix of the global Newton iteration. Upon its convergence, we store the corresponding serial sarcomere number ϑ locally at the integration point level.

Table 4.1: Material parameters for elastic model and growth model.

	interpretation	value	unit
L	Lamé parameter	0.714	N/mm ²
G	Lamé parameter	0.179	N/mm ²
γ	deposition nonlinearity	0.250	–
ϑ^{\max}	max serial sarcomere number	2.000	–
λ^{crit}	critical stretch threshold	1.000	–
τ	sarcomere deposition time	5.000	days

4.3 Results

We illustrate the features of our model by means of three examples. In the first example, we calibrated the material parameter values of the growth model and compared the simulation against experimental findings of sarcomerogenesis in a chronic rabbit model. In the second and third examples, we analyzed temporal and regional variations of the microscopic sarcomere length and number, and explored their relations to the macroscopic elastic and inelastic stretch. Throughout all computational simulations, we used the same calibrated set of material parameters summarized in Table 4.1.

Model problem of limb lengthening: Experiment vs simulation

To demonstrate the performance of the proposed model, we simulated the chronic stretching of the extensor digitorum lateralis muscle during limb lengthening, see Figure 4.2, and compared the simulation with experimental findings reported in the literature [144].

Experimentally, in a chronic limb lengthening model, the radius and the ulna of the left forearm of $n = 21$ rabbits were lengthened by 3.5mm through a transverse osteotomy, while $n = 10$ right forearms served as controls. This particular lengthening mimicked the difference between the length of the extensor digitorum lateralis muscle in full palmar wrist flexion and in full dorsiflexion. With an original ulnar length of 85mm, the lengthening of 3.5mm induced a bone stretch of $\lambda = 1.04$. With an original original extensor digitorum lateralis length of 24mm, the lengthening of 3.5mm induced a muscle stretch of $\lambda = 1.14$. The study assumed that the connecting tendon was significantly stiffer than the stretched muscle, and therefore remained virtually unstretched [144]. Sarcomere lengths were recorded in the unstretched right forearm to serve as controls ($n=10$), and in the stretched left forearm at days 0 ($n=5$), 2 ($n=4$), 5 ($n=4$), 9 ($n=4$), and 14 ($n=4$) using light diffraction imaging. Computationally, we modeled the stretched muscle as a homogeneous unit stretched by $\lambda = 1.14$. We restricted the maximum serial sarcomere number to $\vartheta^{\max} = 2.0$ and chose the critical threshold for the onset of sarcomerogenesis to $\lambda^{\text{crit}} = 1.0$. From a parameter calibration of the experimental measurements [144], we selected the sarcomere deposition time to $\tau = 5.0$ days and the sarcomere

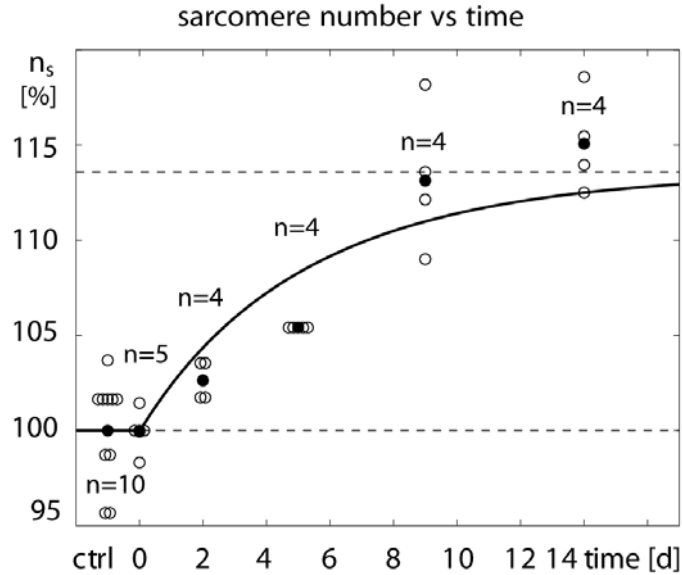


Figure 4.4: Temporal evolution of serial sarcomere number ϑ in chronically stretched skeletal muscle. Upon stretching the extensor digitorum lateralis muscle by $\lambda = 1.14$, the sarcomere number increases gradually from 1.00 to 1.14 within two weeks, bringing the sarcomere length l_s back to its initial value. Computationally predicted sarcomere numbers (solid line) agree nicely with experimentally measured sarcomere numbers (white circles) and their mean values (black circles) from [144].

Table 4.2: Sarcomere lengths in chronically stretched skeletal muscle. Computationally predicted sarcomere lengths agree nicely with experimentally measured sarcomere lengths with errors on the order of the experimental standard deviation [144].

	ctrl	d0	d2	d5	d9	d14
experiment [μm]	3.09	3.51	3.42	3.33	3.10	3.05
\pm std [μm]	0.09	0.04	0.03	0.00	0.10	0.07
simulation [μm]	3.09	3.51	3.36	3.24	3.16	3.12
\pm error [μm]	0.00	0.00	0.06	0.09	0.06	0.07
error [%]	0.00	0.00	1.65	2.66	1.93	2.30

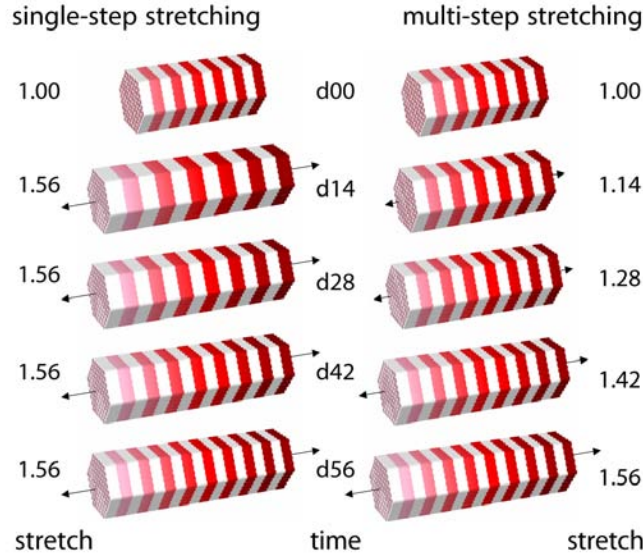


Figure 4.5: Single-step stretching vs multi-step stretching of skeletal muscle. A total stretch of $\lambda = 1.56$ is applied ad hoc (left) and gradually (right). Sarcomerogenesis is simulated for over period of eight weeks.

0.00% by model design. The average relative standard chronic error of the computational prediction, i.e., the average chronic error at days 2, 5, 9, and 14, was 2.13%. At all time points, the simulation error was of the same order of magnitude as the experimental standard deviation.

Model problem of limb lengthening: Single-step vs multi-step stretching

To illustrate a potential application of the proposed model in therapeutic protocol design, we simulated and compared the chronic stretching of the extensor digitorum lateralis muscle during a single-step and a multi-step limb lengthening procedure.

Figure 4.5 illustrates the simulated procedure with the total stretch applied in a single step of $\lambda = 1.56$, shown on the left, and applied in four steps of $\lambda = 1.14, 1.28, 1.42$ and 1.65 , shown on the right. We utilized the material parameters identified in the previous section, i.e, a maximum serial sarcomere number of $\vartheta^{\max} = 2.0$, a critical threshold for the onset of sarcomerogenesis of $\lambda^{\text{crit}} = 1.0$, a sarcomere deposition time of $\tau = 5.0$ days, a sarcomere deposition nonlinearity of $\gamma = 0.25$, and a time step size of $\Delta t = 0.2$ days. This implied that the first step of the multi-step simulation was identical to the simulation of the previous section, see Figure 4.5, top right.

Figure 4.6 illustrates the temporal evolution of the macroscopic quantities, muscle stretch and muscle stress, and of the microscopic quantities, serial sarcomere number and sarcomere length. The single-step stretching procedure indicated through the dashed lines induced a drastic change in stretch,

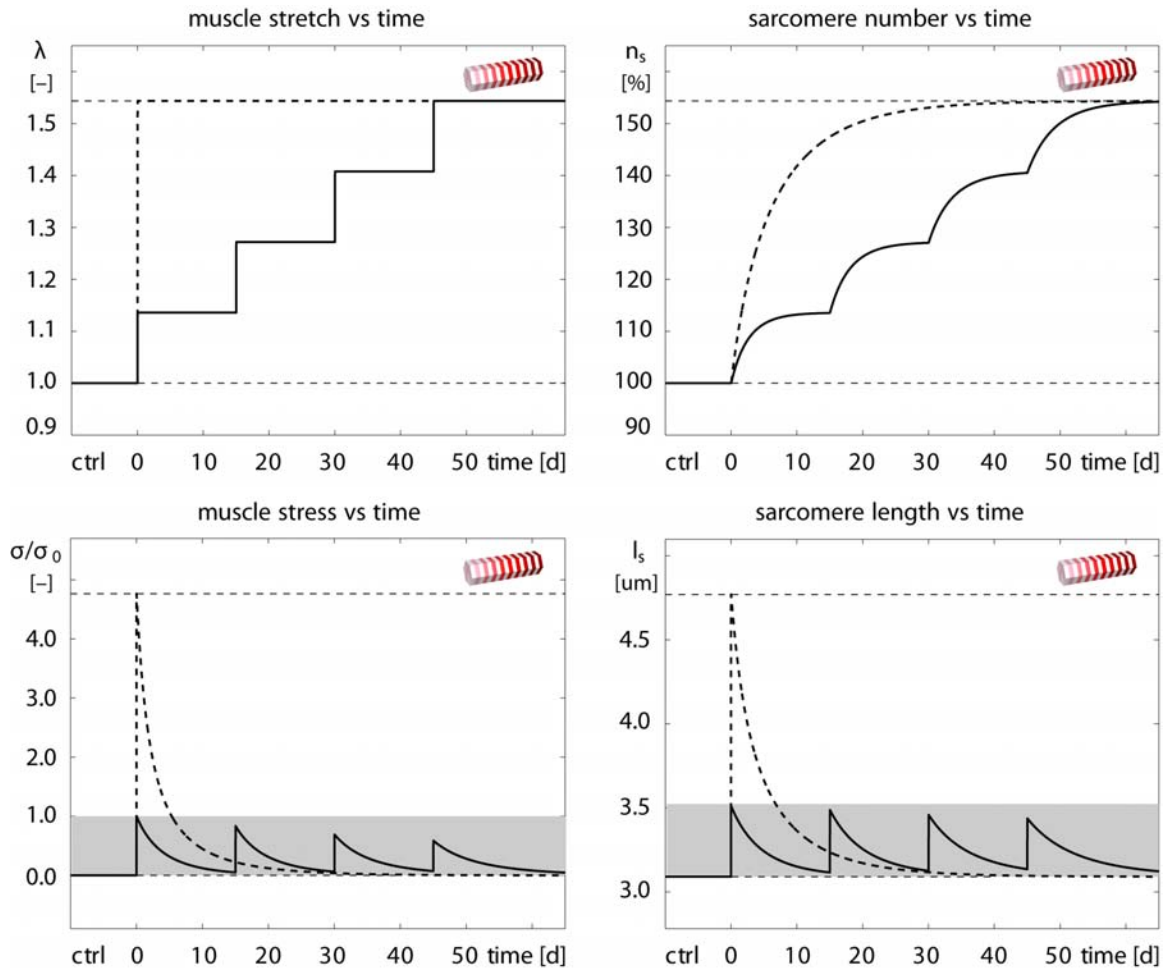


Figure 4.6: Temporal evolution of muscle stretch λ , muscle stress σ/σ_0 , serial sarcomere number n_s , and sarcomere length l_s in chronically stretched skeletal muscle. Single-step stretching (dashed lines) induces a drastic change in stretch resulting in a pronounced overstress and sarcomere lengthening. Multiple-step stretching (solid lines) induces a gradual change in stretch inducing a moderate overstress and sarcomere lengthening. Muscle stress and sarcomere length stay within their physiological regimes (gray box).

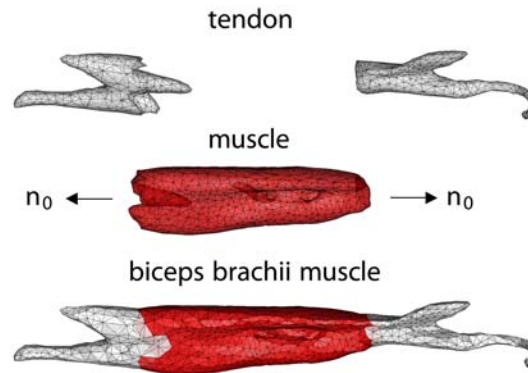


Figure 4.7: Biceps brachii muscle. The finite element model reconstructed from magnetic resonance images consists of 2,705 nodes and a total of 11,816 linear tetrahedral elements. The muscle, discretized by 9,393 elements (red), is attached to the elbow (left) and to the shoulder (right) through the distal and proximal biceps tendons, discretized by 2,423 elements (gray). The biceps brachii is a classical fusiform muscle with fibers \mathbf{n}_0 arranged in parallel bundles along its long axis [27].

top left, resulting in a pronounced overstress, bottom left, and pronounced sarcomere lengthening, bottom right. The multi-step stretching procedure indicated through the solid lines induced a gradual change in stretch, top left, resulting in a moderate overstress, bottom left, and moderate sarcomere lengthening, bottom right. While single-step stretching induced unphysiologically large muscle stresses and sarcomere lengths, multi-step stretching kept both these values within their physiological regimes, indicated through the gray boxes.

Clinical problem of biceps tendon tear

To illustrate the potential of the proposed model in stretch-induced lengthening of a realistic muscle geometry, we simulated sarcomerogenesis in the biceps brachii muscle. Stretch-induced re-lengthening might become necessary after complete tendon tear, when the retracted distal or proximal biceps tendon is surgically reattached to the bone [70]. Figure 4.7 illustrates our finite element model of the biceps brachii muscle, reconstructed from magnetic resonance images [27, 107]. We discretized the muscle-tendon unit with 11,816 linear tetrahedral elements connected at 2,705 nodes. The muscle consisted of 9,393 elements, shown in red. The distal and proximal biceps tendons, which connect the muscle to the elbow, left, and to the shoulder, right, consisted of 2,423 elements, shown in gray. Since the biceps brachii is a classical fusiform muscle [27], we assumed that its fibers are arranged in parallel bundles along its long axis indicated through the vector \mathbf{n}_0 .

We modeled the reattachment of the tendon after tendon tear, by lengthening the 40cm long muscle-tendon unit by 2cm. Here we were not particularly interested in the forces needed to apply this particular stretch [70]. Accordingly, for simplicity, we selected a simple Neo-Hookean elastic model

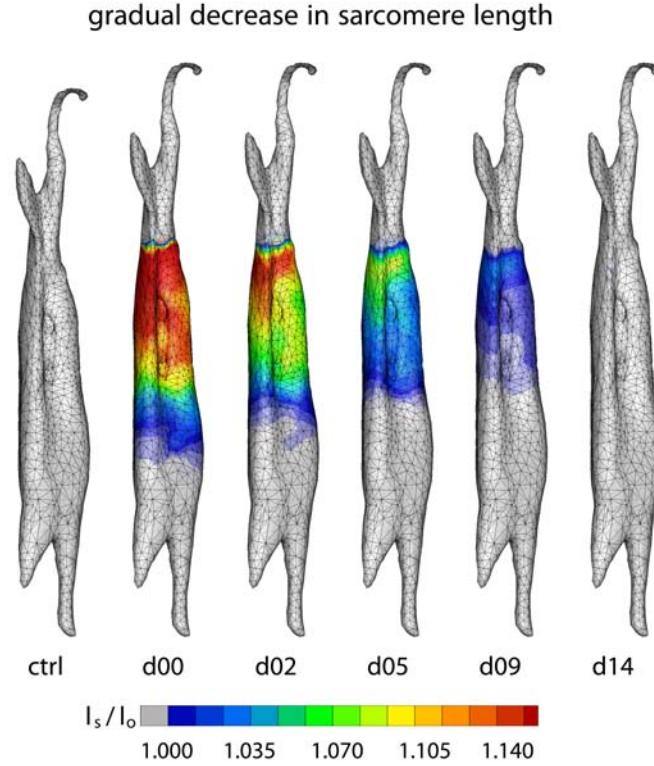


Figure 4.8: Spatio-temporal evolution of sarcomere length l_s/l_o in chronically stretched skeletal muscle. Upon lengthening the biceps brachii muscle by 2cm, i.e., by 5%, the sarcomere length increases acutely from $l_s/l_o = 1.00$ to $l_s/l_o = 1.14$ and beyond, and then returns chronically to its initial value of $l_s/l_o = 1.00$ within two weeks. The sarcomere length l_s is a measure for the elastic fiber stretch λ^e .

with $L = 0.714 \text{ N/mm}^2$ and $G = 0.179 \text{ N/mm}^2$ for the muscle tissue. Since the tendon tissue is more than one order of magnitude stiffer than the muscle tissue [43], we modeled the distal and proximal tendons as semi-rigid. For the muscle tissue, we adapted the model parameters calibrated in the previous section, and chose the maximum serial sarcomere number to $\vartheta^{\max} = 2.0$, the critical threshold for the onset of sarcomerogenesis to $\lambda^{\text{crit}} = 1.0$, the sarcomere deposition time to $\tau = 5.0$ days, and the sarcomere deposition nonlinearity to $\gamma = 0.25$. We used a time step size of $\Delta t = 0.2$ days and simulated a chronic adaptation interval of 14 days.

Figure 4.8 illustrates the spatio-temporal evolution of the sarcomere length l_s/l_o in the control state, left, and in the stretched state at day 0, day 2, day 5, day 9, and day 14, right. A total lengthening of 2cm stretched the overall muscle unit by 5% along its long axis. Since the tendon tissue was assumed to be semi-rigid, this resulted in an average sarcomere length of approximately $l_s/l_o = 1.14$. Upon stretching, the sarcomere length increased acutely from $l_s/l_o = 1.00$ to $l_s/l_o = 1.14$ on day 0,

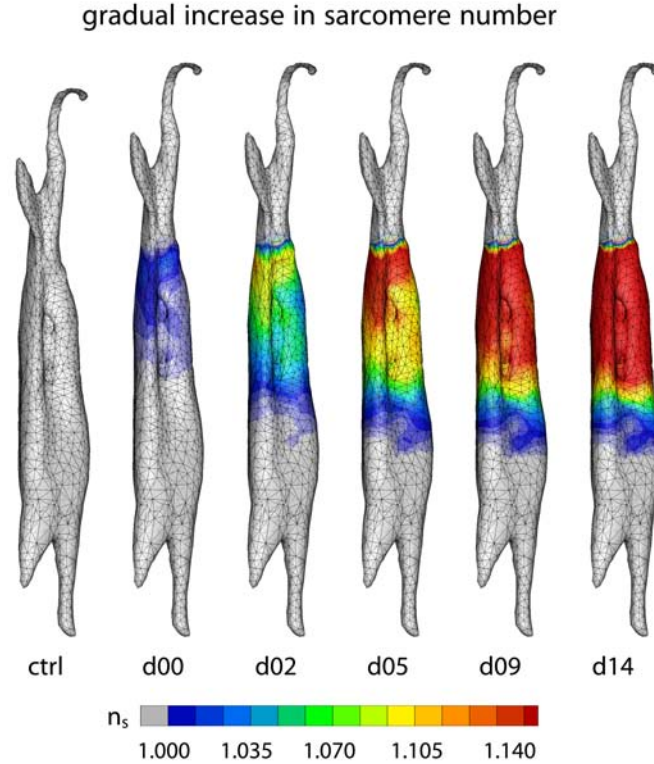


Figure 4.9: Spatio-temporal evolution of serial sarcomere number ϑ in chronically stretched skeletal muscle. Upon stretching the biceps brachii muscle by $\lambda = 1.14$, the serial sarcomere number increases gradually from $\vartheta = 1.00$ to $\vartheta = 1.14$ within two weeks, bringing the sarcomere length back to its initial value of $l_s/l_o = 1.00$. The serial sarcomere number ϑ is a measure for the inelastic fiber stretch λ^g .

and then returned chronically to its initial value of $l_s/l_o = 1.00$ within the simulated period of two weeks. Figure 4.8 demonstrates that the sarcomere length displayed a significant regional variation. Proximally, at the shoulder side, where the muscle-tendon interface is relatively sharp, the sarcomere length was $l_s/l_o = 1.14$ and larger, see Figure 4.8, top. Distally, at the elbow side, where the stiff tendon branches into the soft muscle tissue, the sarcomere length was $l_s/l_o = 1.04$ and smaller, see Figure 4.8, bottom. The sarcomere length l_s is a measure for the elastic fiber stretch λ^e .

Figure 4.9 illustrates the spatio-temporal evolution of the serial sarcomere number ϑ in the control state, left, and in the stretched state at day 0, day 2, day 5, day 9, and day 14, right. Upon stretching the biceps brachii muscle by $\lambda = 1.14$, the serial sarcomere number increased gradually from $\vartheta = 1.00$ to $\vartheta = 1.14$ within two weeks, while, at the same time, the sarcomere length decreased from $l_s/l_o = 1.14$ to $l_s/l_o = 1.00$. Similar to the sarcomere length, the serial sarcomere number displayed a significant regional variation, with largest values and sharp profiles proximally, at the shoulder side,

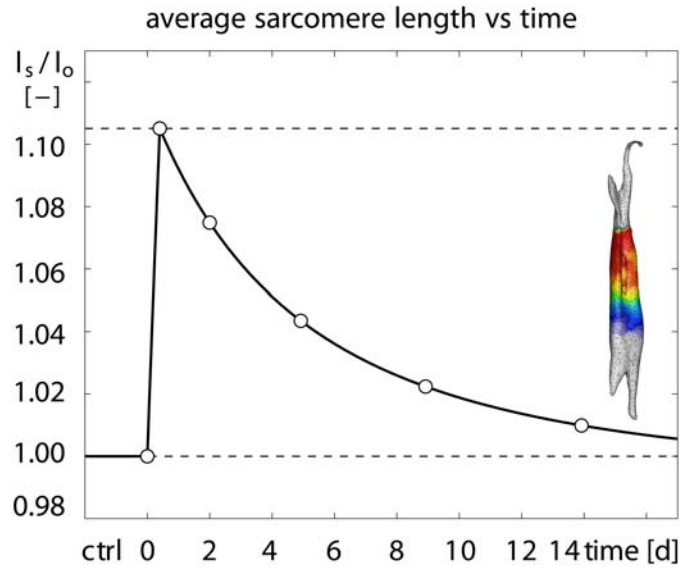


Figure 4.10: Temporal evolution of average sarcomere length l_s/l_o in chronically stretched skeletal muscle. Upon stretching the biceps brachii muscle by $\lambda=1.14$, the average sarcomere length increases acutely to 1.105 times its initial length and then returns chronically to its initial length within two weeks. Averaged sarcomere length at discrete time points (white circles) correspond to the volume averaged elastic stretches λ^e , averaged over the muscle tissue region in Figure 4.8.

and smallest values and smooth profiles distally, at the elbow side. The serial sarcomere number ϑ is a measure for the inelastic fiber stretch λ^s .

Figure 4.10 displays the temporal evolution of the average sarcomere length l_s calculated as the volume average of the elastic stretch λ^e , scaled by the initial sarcomere length l_o . The average sarcomere length increased rapidly by almost 0.105, and then decreased back to its initial length within a period of 14 days. Qualitatively, the shape of the curve corresponds to the evolution of the sarcomere length in the limb lengthening experiment of Figure 4.3. Quantitatively, the averaged sarcomere length at days 0, 2, 5, 9, and 14, indicated through the white circles, correspond to the volume averaged elastic stretches λ^e illustrated in Figure 4.8.

Figure 4.11 displays the temporal evolution of the total sarcomere number ϑ scaled by the initial sarcomere number. The average sarcomere number increased smoothly by 0.105 within a period of 14 days. Qualitatively, the shape of the curve corresponds to the evolution of the sarcomere number in the limb lengthening experiment of Figure 4.4. Quantitatively, the sarcomere numbers at days 0, 2, 5, 9, and 14, indicated through the white circles, correspond to the volume averaged inelastic stretches λ^s illustrated in Figure 4.9.

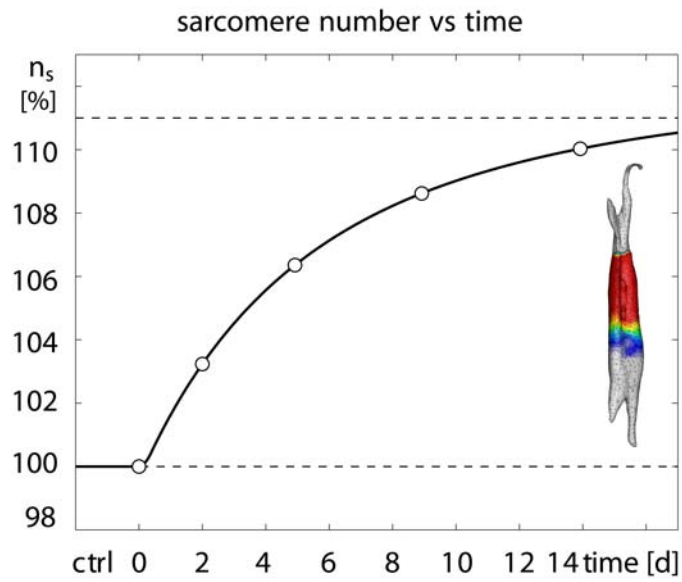


Figure 4.11: Temporal evolution of serial sarcomere number ϑ in chronically stretched skeletal muscle. Upon stretching the biceps brachii muscle by $\lambda = 1.14$, the sarcomere number increases gradually from 1.00 to 1.11 within two weeks, bringing the individual sarcomere lengths l_s back to their initial values. Sarcomere numbers at discrete time points (white circles) correspond to the volume averaged inelastic stretches λ^s , averaged over the muscle tissue region in Figure 4.9.

4.4 Discussion

We have proposed, for the first time, a mechanistic multiscale model for stretch-induced sarcomerogenesis, in which chronic muscle lengthening is characterized through a scalar-valued internal variable, the serial sarcomere number. The model interprets the macroscopic elastic and inelastic fiber stretches λ^e and λ^g as metrics for the microscopic sarcomere length and sarcomere number l_s and ϑ . It is in excellent qualitative and quantitative agreement with the sarcomere lengths observed in a chronic limb lengthening experiment.

Limitations

Although our first prototype model agrees nicely with experimental findings, a few limitations remain to be addressed in future model refinements. First, for the sake of simplicity, we have chosen a relatively straightforward baseline elastic model, see equation (4.7). Since we model the growth process as strain-driven [36] and not stress-driven [87], the choice of the constitutive model affects the growth process only indirectly. An appropriate muscle model would become important though if we wanted to predict limit stresses and forces required to apply the desired stretch [70]. However, as our approach is inherently modular, it would be relatively straightforward to integrate a more physiological constitutive model [24, 29]. Second, since tendon tissue is more than one order of magnitude stiffer than muscle tissue [27, 43], we have modeled the tendon as semi-rigid. This approach provides quick insight into overall characteristics and trends. Extending the model towards a tendon with a finite stiffness should not pose additional complexity, provided the tendon model parameters are known [43]. Third, we have assumed that muscle lengthening translates directly into sarcomere lengthening, i.e., that the elastic fiber stretch is directly correlated to the sarcomere length [75]. This approach is relatively common in the skeletal muscle literature [13, 144], although potential second order effects could possibly contribute to additional muscle lengthening. Fourth, we have adopted a simple functional form for the evolution of the sarcomere number in equations (4.9) and (4.10). This particular format is conceptually well-understood since it has been applied to model growth of other soft biological tissues, first in a stress-driven [118, 139] then in a strain-driven [72, 176] version. Although this format seems to yield an excellent agreement with experimental findings, alternative evolution equations might be possible and could be integrated in a relatively straightforward fashion. Along the same lines, we could further enhance the model to integrate sarcomere disassembly upon chronically reduced stretch [40], a phenomenon that has been studied intensely during immobilization [194, 216] and tendon retraction [70]. Last, to better calibrate the model, a richer data set would be desirable. Here we have based our model calibration on a two-week long limb lengthening study in rabbits [144]. At this point, it is unclear whether the adaptation speed observed in small animals translates directly to humans. Currently, the lack of chronic experiments with multiple well-defined time points still limits the clinical use of the model. However, recent developments in

second harmonic generation microendoscopy [136] now allow us to measure local sarcomere length non-invasively in humans, to precisely quantify spatial and temporal sarcomere variations in vivo.

Significance

Our model is the first mechanistic model to link macroscopic elastic and inelastic stretch to microscopic sarcomere length and number using nonlinear continuum theories of finite growth. On the microscopic scale, chronic muscle stretching beyond the physiological limit creates unphysiologically large sarcomere lengths [20], which, in turn, induce a serial sarcomere deposition [42]. The resulting increase in sarcomere number causes a chronic restoration of the initial sarcomere length [86]. On the macroscopic scale, the serial sarcomere deposition induces a chronic reduction of the macroscopic elastic stretch, gradually reducing the passive stress [71], a phenomenon similar to classical stress relaxation [38]. Our model provides a mechanistic understanding of the underlying mechanisms accompanying chronic muscle stretch and sarcomerogenesis [104]. At this point, it does not describe the mechanobiology and the mechanotransduction pathways associated with sarcomerogenesis [61]. However, ultimately, it would be desirable to tie the mechanical response to mechanoreception, intracellular signaling pathways, and target activation [41].

We have shown that our model can explain why gradual multi-step stretching is less invasive than single-step stretching [85]. It also explains regional variation in sarcomere lengths [182], shorter close to and longer away from the muscle-tendon interface, where the stiff tendon provides additional support to stretch [75]. Acutely, our model could serve as a design tool to prevent short-term muscle damage caused by mechanical overstretch. Macroscopically for a given limit stress, or equivalently, microscopically for a given limit sarcomere length, we could optimize temporal stretching sequences that predict the maximum possible stretch within acceptable limits [230]. The ultimate goal would be to maximize stretch-induced muscle growth, such that the muscle always stays within a physiologically reasonable operating range. Chronically, our model could serve as a design tool to predict long-term muscle adaptation. We could easily integrate it into existing skeletal muscle models to optimize muscle lengthening in response to eccentric training [195] or to predict different surgical procedures such as tendon transfer, tendon reattachment, or tendon lengthening [12]. The ultimate goal would be to guarantee optimal regeneration and long-term repair durability.

4.5 Conclusion

Striated muscle adapts to chronic mechanical stretch through the creation and serial deposition of new sarcomere units. The phenomenon of sarcomerogenesis has been quantified in chronic animal experiments, but it has never been modeled computationally. Here we have presented a mathematical model for chronic muscle growth through sarcomerogenesis and illustrated its computational realization. Acutely, upon 14% lengthening of the extensor digitorum lateralis muscle, the model

predicts a sarcomere lengthening from $3.09\mu\text{m}$ to $3.51\mu\text{m}$ with a model error of 0.00%. Chronically, the model predicts the gradual return to the initial sarcomere length within two weeks with a model error of 2.13%, which is within the range of the experimental standard deviation. Once calibrated with a richer data set, our model may be used to help surgeons to make informed decisions about optimal stretch increments, stretch timing, and stretch amplitudes. Our study might to open new avenues in orthopedic and reconstructive surgery and enhance muscle adaptation, repair, and regeneration for patients with ill proportioned limbs, tendon lengthening, tendon transfer, tendon tear, or chronically retracted muscles.

4.6 Acknowledgments

This material is part of a final project for the Stanford graduate course ME337 Mechanics of Growth. This work was supported by the National Science Foundation CAREER award CMMI-0952021 and by the National Institutes of Health Grant U54 GM072970.

Chapter 5

A multiscale model for sarcomere loss

Abstract

High heels are a major source of chronic lower limb pain. Yet, more than one third of all women compromise health for looks and wear high heels on a daily basis. Changing from flat footwear to high heels induces chronic muscle shortening associated with discomfort, fatigue, reduced shock absorption, and increased injury risk. However, the long-term effects of high-heeled footwear on the musculoskeletal kinematics of the lower extremities remain poorly understood. Here we create a multiscale computational model for chronic muscle adaptation to characterize the acute and chronic effects of global muscle shortening on local sarcomere lengths. We perform a case study of a healthy female subject and show that raising the heel by 13 cm shortens the gastrocnemius muscle by 5% while the Achilles tendon remains virtually unaffected. Our computational simulation indicates that muscle shortening displays significant regional variations with extreme values of 22% in the central gastrocnemius. Our model suggests that the muscle gradually adjusts to its new functional length by a chronic loss of sarcomeres in series. Sarcomere loss varies significantly across the muscle with an average loss of 9%, virtually no loss at the proximal and distal ends, and a maximum loss of 39% in the central region. These changes reposition the remaining sarcomeres back into their optimal operating regime. Computational modeling of chronic muscle shortening provides a valuable tool to shape our understanding of the underlying mechanisms of muscle adaptation. Our study could open new avenues in orthopedic surgery and enhance treatment for patients with muscle contracture caused by other conditions than high heel wear such as paralysis, muscular atrophy, and muscular dystrophy.

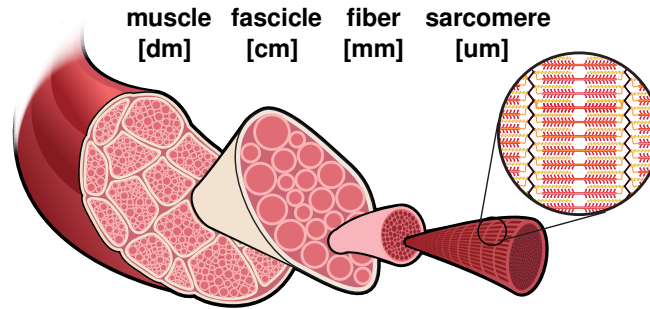


Figure 5.1: Chronic muscle adaptation across the scales. Muscle shortening spans from the whole muscle level via the fascicle level and fiber level all the way down to the sarcomere level and bridges five orders of magnitude in length.

5.1 Motivation

More than two thirds of all American women frequently dress in high-heeled shoes [8], 40% wear their high heels on a daily basis, 10% even more than eight hours per day [221]. High heels are a major contributor to foot problems and lower limb pain, associated with chronic conditions such as hallux vagus, corns, calluses, metatarsalgia, Achilles tendon tightness, planar fasciitis, and Haglund's deformity [53]. In the United States alone, the annual health care cost attributed to high-fashion footwear is estimated to exceed \$3 billion [208]. High-heeled footwear forces the foot into a plantarflexed position associated with shortening of the calf muscle-tendon unit [52]. Short-term, this position is energetically inefficient: It causes excessive actin-myosin overlap and forces muscle fibers into a non-optimal operating range [60]. Long-term, our calf muscles adapt to their new position: They shorten to reposition the actin-myosin overlap into back its optimal regime [53]. Figure 5.1 summarizes the spatial scales involved in chronic muscle adaptation [217].

On the muscle level, frequent high heel wear affects primarily in the gastrocnemius muscle, while the lengths of the soleus muscle and the Achilles tendon remain virtually unchanged [103]. On the fascicle level, frequent high heel use shortens the average fascicle length of the medial gastrocnemius muscle by 12% [51]. Not surprisingly, these functional and structural changes affect the active range of motion of the ankle joint and cause a noticeable shift towards the supinated position [53]. This reduced range of motion decreases efficient shock absorption and increases the risk of ligament sprains [103]. In addition, habitual high heel wearers compromise muscle efficiency, suffer from discomfort and muscle fatigue, and increase the risk of strain injuries [52]. Yet, switching back to flat footwear can be extremely painful [105]; it overstretches the triceps surae and may trigger planar fasciitis [156], the most common cause of heel pain [206].

The smallest functional unit involved in chronic muscle adaptation is a sarcomere. Sarcomeres are 3 μ m long assemblies of thick filaments of myosin sliding along thin filaments of actin [132]. On the

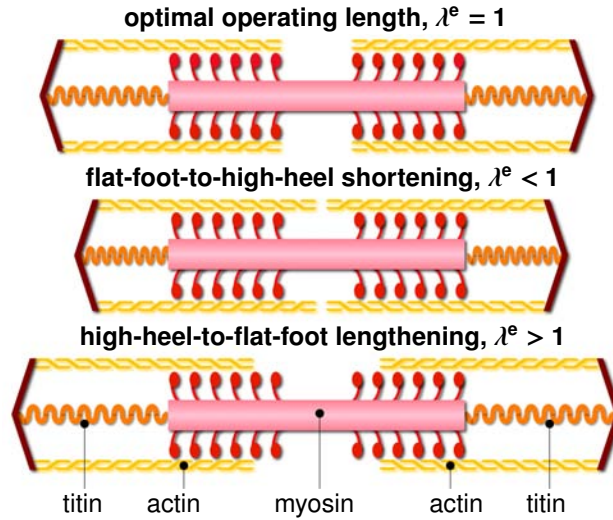


Figure 5.2: Chronic muscle adaptation on the sarcomere scale. Sarcomeres are $3\mu\text{m}$ long assemblies of thick filaments of myosin sliding along thin filaments of actin. An optimal overlap of actin and myosin is critical to maximum force generation. To maintain sarcomeres within their optimal operating range, skeletal muscle responds to chronic shortening by removing sarcomeres in series.

sarcomere level, an optimal overlap of actin and myosin filaments is critical to maximum force generation [152]. Not surprisingly, the sarcomere length is tightly regulated [76]. Figure 5.2 illustrates a sarcomere unit at its optimal operating length, and in non-optimal shortened and lengthened positions. To always maintain each sarcomere within its optimal operating range, skeletal muscle responds to a chronic reduction in functional length through the active removal of sarcomeres in series [196]. Almost half a century ago, controlled immobilization experiments in mice [215] and cat [196] have demonstrated the chronic loss of sarcomeres in series by fixing a muscle in a shortened position. Recent studies suggest that frequent high heel use has similar effects: It reduces the fascicle length, which may trigger the controlled removal of sarcomeres in an attempt to reposition the muscle in its optional operating regime [51].

Taken together, the above studies provide valuable insight into chronic muscle shortening at the individual scales. Yet, the interaction of the underlying mechanisms across the scales remains poorly understood [217]. Here we present a continuum model for chronic muscle adaptation, in which changes in whole muscle length are treated as emergent properties of local changes in sarcomere number, muscle fiber length, and fascicle length. Continuum modeling is a valuable tool to reveal the mechanisms behind skeletal muscle adaptation [217]. Combined with the theory of finite growth [6], the nonlinear field theories of mechanics provide high-resolution insight into local stretch concentrations in response to altered muscle kinematics [26]. Multiscale models of finite growth correlate the global elastic stretch along the muscle fiber direction with the local sarcomere length [28].

To maintain this length within its physiologically optimal regime, the local sarcomere number undergoes dynamic change, which translates globally into an inelastic stretch or growth [72]. Previous models for cardiac muscle, the extensor digitorum, and the biceps brachii have successfully applied this concept to model positive growth associated with chronic muscle lengthening in dilated cardiomyopathy [73], limb lengthening, and tendon tear [225]. Here we adopt the same paradigm to model negative growth associated with chronic muscle shortening in frequent high heel wear.

5.2 Methods

To simulate the short- and long-term effects of high-heeled footwear, we create a subject-specific model of the lower limb using magnetic resonance images in flat foot and high heel positions. We perform a finite element analysis of acute and chronic muscle shortening using the continuum theory of finite growth.

5.2.1 Continuum model

To represent large muscle deformations, we adopt the kinematics of finite growth, and introduce the deformation map $\varphi(\mathbf{X}, t)$ mapping particles \mathbf{X} from the initial configuration to particles $\mathbf{x} = \varphi(\mathbf{X}, t)$ in the new configuration. We multiplicatively decompose its gradient $\mathbf{F} = \nabla_{\mathbf{X}}\varphi$ into an elastic contribution \mathbf{F}^e and an inelastic contribution \mathbf{F}^g [183], which we associate with chronic muscle adaptation [225],

$$\mathbf{F} = \nabla_{\mathbf{X}}\varphi = \mathbf{F}^e \cdot \mathbf{F}^g. \quad (5.1)$$

The Jacobian $J = \det(\mathbf{F})$ defines the change in muscle volume,

$$J = \det(\mathbf{F}) = J^e J^g, \quad (5.2)$$

which we decompose into an elastic volume change $J^e = \det(\mathbf{F}^e)$ and an inelastic volume change $J^g = \det(\mathbf{F}^g)$ attributed to muscle adaptation. Similar to the deformation gradient and the Jacobian, we interpret the total stretch λ along the fiber direction of the initial configuration \mathbf{n}_0 as the product of the elastic stretch λ^e and the inelastic stretch λ^g associated with chronic changes in muscle length [151],

$$\lambda = [\mathbf{n}_0 \cdot \mathbf{F}^t \cdot \mathbf{F} \cdot \mathbf{n}_0]^{1/2} = \lambda^e \lambda^g. \quad (5.3)$$

We model chronic muscle shortening as the removal of sarcomeres in series. This implies that we can express the muscle adaptation tensor \mathbf{F}^g as rank-one update of the identity tensor \mathbf{I} [225],

$$\mathbf{F}^g = \mathbf{I} + [\vartheta - 1] \mathbf{n}_0 \otimes \mathbf{n}_0, \quad (5.4)$$

where ϑ is the relative serial sarcomere number. Values of $\vartheta < 1$ represent the removal of sarcomeres in series associated with chronic muscle shortening; values of $\vartheta > 1$ represent the addition of sarcomeres in series associated with chronic muscle lengthening [120]. As a consequence of the specific format of the adaptation tensor \mathbf{F}^g , the serial sarcomere number ϑ not only represents the local muscle fiber shortening λ^g , but also to the volume change in response to sarcomere loss J^g ,

$$\vartheta = \lambda^g = \det(\mathbf{F}^g) = J^g. \quad (5.5)$$

We use the Sherman-Morrison formula to calculate the inverse of the adaptation tensor, $\mathbf{F}^{g-1} = \mathbf{I} + [1 - \vartheta] / \vartheta \mathbf{n}_0 \otimes \mathbf{n}_0$. With the muscle fiber direction in the current configuration $\mathbf{n} = \mathbf{F} \cdot \mathbf{n}_0$ and the inverse \mathbf{F}^{g-1} we find an explicit expression for the elastic tensor,

$$\mathbf{F}^e = \mathbf{F} \cdot \mathbf{F}^{g-1} = \mathbf{F} + \frac{1 - \vartheta}{\vartheta} \mathbf{n} \otimes \mathbf{n}. \quad (5.6)$$

We can then express the Finger tensor in terms of the serial sarcomere number ϑ ,

$$\mathbf{b}^e = \mathbf{F}^e \cdot \mathbf{F}^{et} = \mathbf{F} \cdot \mathbf{F}^t + \frac{1 - \vartheta^2}{\vartheta^2} \mathbf{n} \otimes \mathbf{n}. \quad (5.7)$$

To focus on chronic muscle shortening, for simplicity, we assume homogeneously distributed isotropic material properties for the passive muscle tissue and adopt a strain energy function of Neo-Hookean type,

$$\psi = \frac{1}{2}L \ln^2(J^e) + \frac{1}{2}G [\mathbf{b}^e : \mathbf{i} - 3 - 2 \ln(J^e)], \quad (5.8)$$

where L and G are the Lamé constants and \mathbf{i} is the spatial identity tensor. We assume that the overall muscle microstructure, stiffness, and density are preserved upon adaptation [155], and derive the corresponding Kirchhoff stress tensor from the second law of thermodynamics,

$$\boldsymbol{\tau} = 2 \frac{\partial \psi}{\partial \mathbf{b}^e} \cdot \mathbf{b}^e = [L \ln(J^e) - G] \mathbf{i} + G \mathbf{b}^e. \quad (5.9)$$

At the subcellular level, we model the evolution of the serial sarcomere number ϑ as a strain-driven process [199]. We adopt the following evolution equation [226],

$$\dot{\vartheta} = k(\vartheta) \phi(\lambda^e), \quad (5.10)$$

where k is the adaptation function [139],

$$k = -\frac{1}{\tau} \left[\frac{\vartheta - \vartheta^{\min}}{1 - \vartheta^{\min}} \right]^\gamma, \quad (5.11)$$

parameterized in terms of the adaptation speed τ , the shape parameter for the adaptation function γ , and the minimum serial sarcomere number ϑ^{\min} , and ϕ is the adaptation criterion,

$$\phi = \langle \lambda^{\text{crit}} - \lambda^e \rangle. \quad (5.12)$$

Similar to the yield criterion in plasticity, the adaptation criterion ϕ activates sarcomere removal only if the elastic stretch is lower than the critical stretch as $\langle \lambda^{\text{crit}} - \lambda^e \rangle = \lambda^{\text{crit}} - \lambda^e$ and deactivates sarcomere changes for elastic stretches above the critical stretch as $\langle \lambda^{\text{crit}} - \lambda^e \rangle = 0$.

5.2.2 Computational model

To solve the nonlinear finite element equations of for chronic muscle adaptation, we implement our model as a user subroutine into the implicit commercial finite element solver Abaqus/Standard Version 6.13 (Simulia, Providence, RI) [2]. We introduce the relative serial sarcomere number ϑ as an internal variable, and solve its evolution equation (5.10) locally at the integration point level [72]. At each discrete time step t , we determine the current sarcomere number ϑ for a given current deformation state \mathbf{F} and a given sarcomere number ϑ_n from the previous time step t_n using a finite difference approximation,

$$\dot{\vartheta} = \frac{\vartheta - \vartheta_n}{\Delta t}, \quad (5.13)$$

where $\Delta t = t - t_n$ denotes the current time increment. We adopt an implicit time integration scheme and reformulate the evolution equation (5.10) with the help of equation (5.13), to introduce the discrete residual \mathbf{R} in terms of the unknown sarcomere number,

$$\mathbf{R} = \vartheta - \vartheta_n + k \phi \Delta t \doteq 0. \quad (5.14)$$

We solve this nonlinear equation using a local Newton iteration [73]. Within each iteration step, we calculate the linearization of the residual \mathbf{R} with respect to the serial sarcomere number ϑ ,

$$\mathbf{K} = \frac{\partial \mathbf{R}}{\partial \vartheta} = 1 - \left[\frac{\partial k}{\partial \vartheta} \phi + k \frac{\partial \phi}{\partial \vartheta} \right] \Delta t. \quad (5.15)$$

Here, $\partial k / \partial \vartheta = -\gamma k / [\vartheta - \vartheta^{\min}]$ and $\partial \phi / \partial \vartheta = \lambda / \vartheta^2$ denote the linearizations of the adaptation function (5.11) and of the adaptation criterion (5.12). Within each Newton iteration, we update the unknown sarcomere number,

$$\vartheta \leftarrow \vartheta - \mathbf{R} / \mathbf{K}, \quad (5.16)$$

until we achieve local convergence, i.e., until the absolute value of the sarcomere update $\Delta \vartheta = -\mathbf{R} / \mathbf{K}$ reaches a user-defined threshold value, here we choose 10^{-8} . After determining the current sarcomere number ϑ , we can successively determine the adaptation tensor \mathbf{F}^g from equation (5.4), the elastic tensor $\mathbf{F}^e = \mathbf{F} \cdot \mathbf{F}^g^{-1}$ from equation (5.6), the elastic left Cauchy-Green tensor $\mathbf{b}^e = \mathbf{F}^e \cdot \mathbf{F}^{e\text{t}}$ from

equation (5.7), the Kirchhoff stress $\boldsymbol{\tau}$ from equation (5.9), and, finally, the fourth-order tensor of the Eulerian constitutive moduli,

$$\mathbf{c} = 4 \mathbf{b}^e \cdot \frac{\partial^2 \psi}{\partial \mathbf{b}^e \otimes \mathbf{b}^e} \cdot \mathbf{b}^e = \mathbf{c}^e + \mathbf{c}^g. \quad (5.17)$$

The first term, the Hessian of the free energy function at constant growth \mathbf{F}^g , defines the elastic constitutive moduli,

$$\mathbf{c}^e = L \mathbf{i} \otimes \mathbf{i} + [G - L \ln(J^e)] [\mathbf{i} \overline{\otimes} \mathbf{i} + \mathbf{i} \underline{\otimes} \mathbf{i}], \quad (5.18)$$

with the common abbreviations, $\{\bullet \overline{\otimes} \circ\}_{ijkl} = \{\bullet\}_{ik} \{\circ\}_{jl}$ and $\{\bullet \underline{\otimes} \circ\}_{ijkl} = \{\bullet\}_{il} \{\circ\}_{jk}$, for the non-standard fourth order products. The second term, the Hessian of the free energy function at constant deformation \mathbf{F} , defines the correction of the constitutive moduli due to muscle adaptation [225],

$$\mathbf{c}^g = -\frac{k}{\lambda \vartheta \mathbf{K}} [L \mathbf{I} + 2G/\vartheta^2 \mathbf{n} \otimes \mathbf{n}] \otimes [\mathbf{n} \otimes \mathbf{n}] \Delta t. \quad (5.19)$$

Instead of the Kirchhoff stress (5.9) and the constitutive moduli (5.17), the user-defined subroutine in Abaqus/Standard utilizes the Cauchy or true stress, $\boldsymbol{\sigma} = \boldsymbol{\tau}/J$,

$$\boldsymbol{\sigma}^{\text{abaqus}} = [[L \ln(J^e) - G] \mathbf{i} + G \mathbf{b}^e] / J, \quad (5.20)$$

and the Jauman rate of the Kirchhoff stress divided by the Jacobian, which requires the following modification of the tangent moduli [228],

$$\mathbf{c}^{\text{abaqus}} = [\mathbf{c} + \frac{1}{2} [\boldsymbol{\tau} \overline{\otimes} \mathbf{i} + \mathbf{i} \overline{\otimes} \boldsymbol{\tau} + \boldsymbol{\tau} \underline{\otimes} \mathbf{i} + \mathbf{i} \underline{\otimes} \boldsymbol{\tau}]] / J. \quad (5.21)$$

The local stress $\boldsymbol{\sigma}^{\text{abaqus}}$ of equation (5.20) and the local tangent moduli $\mathbf{c}^{\text{abaqus}}$ of equation (5.21) enter the righthand side vector and the iteration matrix of the global Newton iteration. Upon its convergence, we store the relative serial sarcomere number ϑ locally at the integration point level.

5.2.3 Magnetic Resonance Imaging

To create a finite element model of the lower limb, we collect magnetic resonance images of a healthy 20-year old female subject [25]. We acquire two sets of axial images, in flat foot and in high heel positions, using a product fat water separation gradient echo sequence with parallel imaging using IDEAL (GE Healthcare, Waukesha, WI) [180] and a 3T MRI system using Discovery MR750 (GE Healthcare, Waukesha, WI). To control the foot position during the high heel scan, we build a cardboard shoe model with a well-defined heel height of 13 cm.

Figure 5.3 shows the resulting magnetic resonance images of the right lower limb in flat foot and high heel positions. Images have an in-plane resolution of 0.62 mm \times 0.62 mm and a slice thickness of 3mm. The magnetic resonance images provide the basis for the the finite element model and define

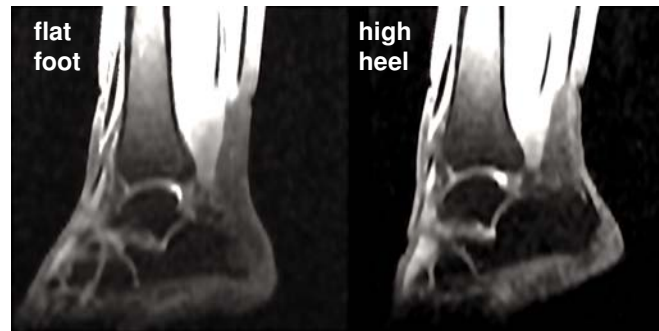


Figure 5.3: Sagittal magnetic resonance images of the right lower limb of a healthy 20-year old female subject. Images show the ankle joint in flat foot position, right, and in high heel position at a heel height of 13 cm, left. The scans provide the basis for the the finite element model and define the boundary conditions when changing from flat foot to high heel position.

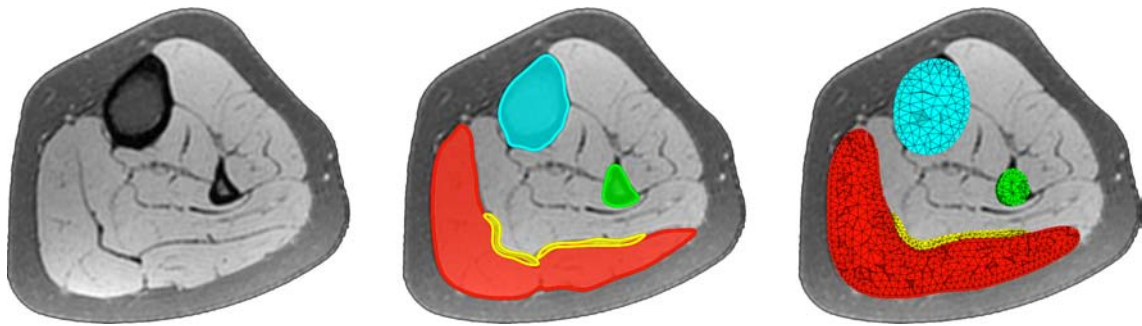


Figure 5.4: Generation of finite element model from magnetic resonance images of the lower limb. We manually segment the image slices and identify the muscles, bones, and tendons as regions of interest in the medical image viewer OsiriX [184], left. To create a mesh for each component, we convert the individual regions into binary masks and process them with CGAL [64], middle. Finally, we filter the preliminary mesh to create smooth surfaces [204], right.

the boundary conditions when changing from flat foot to high heel position.

Figure 5.4 illustrates the workflow to generate a finite element model from magnetic resonance images. Using the medical image viewer OsiriX [184], we manually identify the individual muscles, bones, and tendons as regions of interest in a slice-by-slice manner. We then export binary masks from these regions to create a mesh for every component using the Computational Geometry Algorithms Library CGAL [64]. Finally, we filter the preliminary mesh to create a final mesh with smooth surfaces [204].

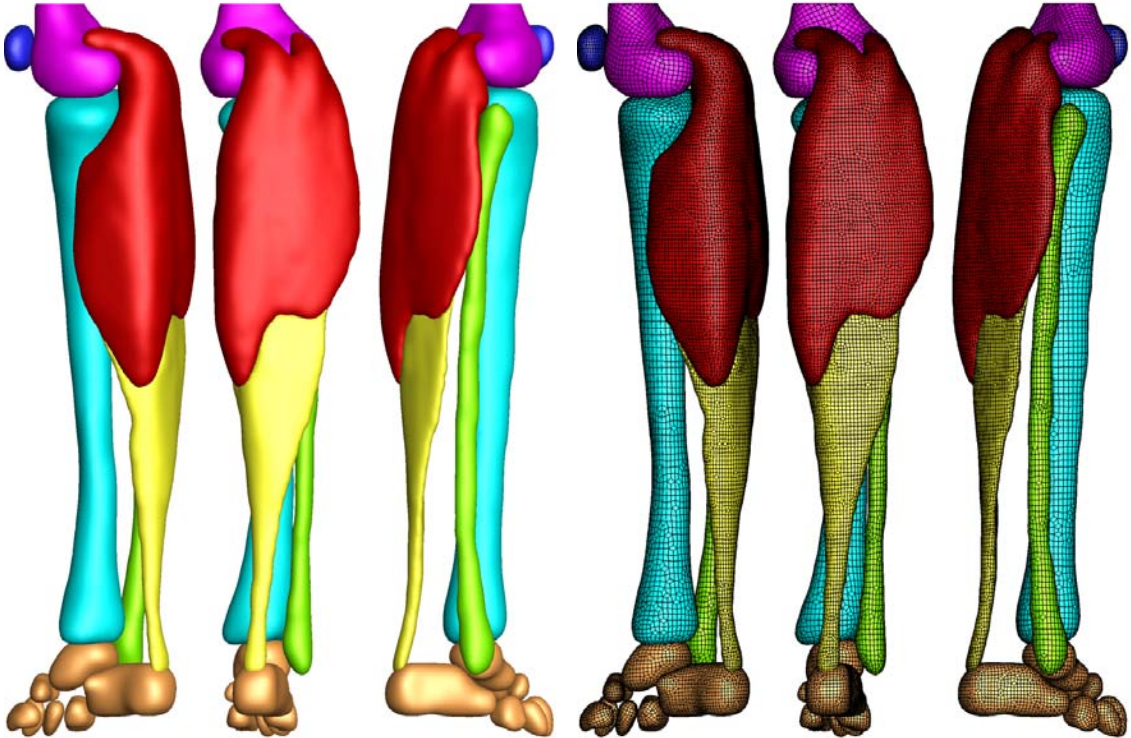


Figure 5.5: Finite element model of the lower limb. The model consists of 81,146 nodes and 377,034 linear tetrahedral and pyramid elements. The proximal end of the gastrocnemius muscle (165,820 elements, red) is fixed next to the femur while the distal end is connected to the Achilles tendon (55,945 elements, yellow). The femur (22,838 elements, magenta), patella (8,987 elements, blue), tibia (48,369 elements, cyan), fibula (22,086 elements, green), and the tarsal bones (52,989 elements, orange) are modeled as rigid bodies.

5.2.4 Finite element model

Figure 5.5 shows the final finite element model of the lower limb, which contains 81,146 nodes and 377,034 linear tetrahedral and pyramid elements. We choose a combination of tetrahedral and pyramid elements because of their ease of use when meshing complex geometries from clinical images. We note, however, that linear tetrahedral elements are known to be overly stiff, and that using either quadratic tetrahedra or hexahedral elements would fix this issue. Our model consists of the femur with 22,838 elements, shown in magenta, the patella with 8,987 elements, shown in blue, the gastrocnemius muscle with 165,820 elements, shown in red, the tibia with 48,369 elements, shown in cyan, the fibula with 22,086 elements, shown in green, the Achilles tendon with 55,945 elements, shown in yellow, and the tarsal bones with 52,989 elements, shown in orange.

We model the gastrocnemius muscle as Neo-Hookean elastic with Lamé constants $L = 0.714 \text{ N/mm}^2$ and $G = 0.179 \text{ N/mm}^2$. Once the elastic fiber stretch falls below the threshold of $\lambda^{\text{crit}} = 1.0$, we gradually remove sarcomeres towards a minimum sarcomere number of $\vartheta^{\text{min}} = 0.0$ with an

Table 5.1: Dimensions of muscle tendon unit in flat foot and high heel positions. Wearing footwear with a heel height of 13 cm shortens the gastrocnemius medialis by 12 mm while the Achilles tendon remains unaffected. These changes in length define the inhomogeneous Dirichlet boundary conditions of our finite element simulation.

	muscle-tendon unit [mm]	gastrocnemius medialis [mm]	achilles tendon [mm]
flat foot	396	225	171
high heel	384	213	171
difference	-12	-12	0

adaptation speed $\tau = 1.0$ days and a shape parameter $\gamma = 1.0$. This implies that here, we drive muscle loss through non-tensile loading, while physiological muscle loss could generally occur in response to a variety of other environmental changes [217]. For computational efficiency, we assume that the bones and the Achilles tendon are significantly stiffer than the gastrocnemius muscle and model them as rigid bodies [141, 223].

Table 5.1 summarizes the dimensions of the muscle tendon unit in flat foot and high heel positions extracted from our magnetic resonance images. When changing from the flat footwear to high heels, the gastrocnemius medialis shortens by 12 mm while the Achilles tendon maintains its length. These measurements support our model assumption of a rigid tendon. To fix the muscle-tendon unit in space, we apply homogeneous Dirichlet boundary conditions at the medial and lateral heads of the gastrocnemius muscle where they attach to the condyle of the femur. To move the model from flat foot to high heel position and vice versa, we apply inhomogeneous Dirichlet boundary conditions at the distal nodes of the Achilles tendon and prescribe a gradual upward and downward displacement of 12 mm.

5.2.5 Muscle fiber model

As the foot is moved into the high heel position, we gradually allow the gastrocnemius muscle to remove sarcomeres in series to reposition the remaining sarcomeres at their optimal operating length. As a bipennate muscle, the gastrocnemius muscle consists of two rows of oblique muscle fibers, which face in opposite diagonal directions and converge jointly in the Achilles tendon. To account for these regionally varying fiber orientations, we divide the muscle into six regions of interest and assign each region an individual fiber orientation [174].

Figure 5.6 illustrates our muscle fiber orientation model of the gastrocnemius muscle. Table 5.2 summarizes the fiber orientations \mathbf{n}_0 associated with six discrete regions of interest [174].

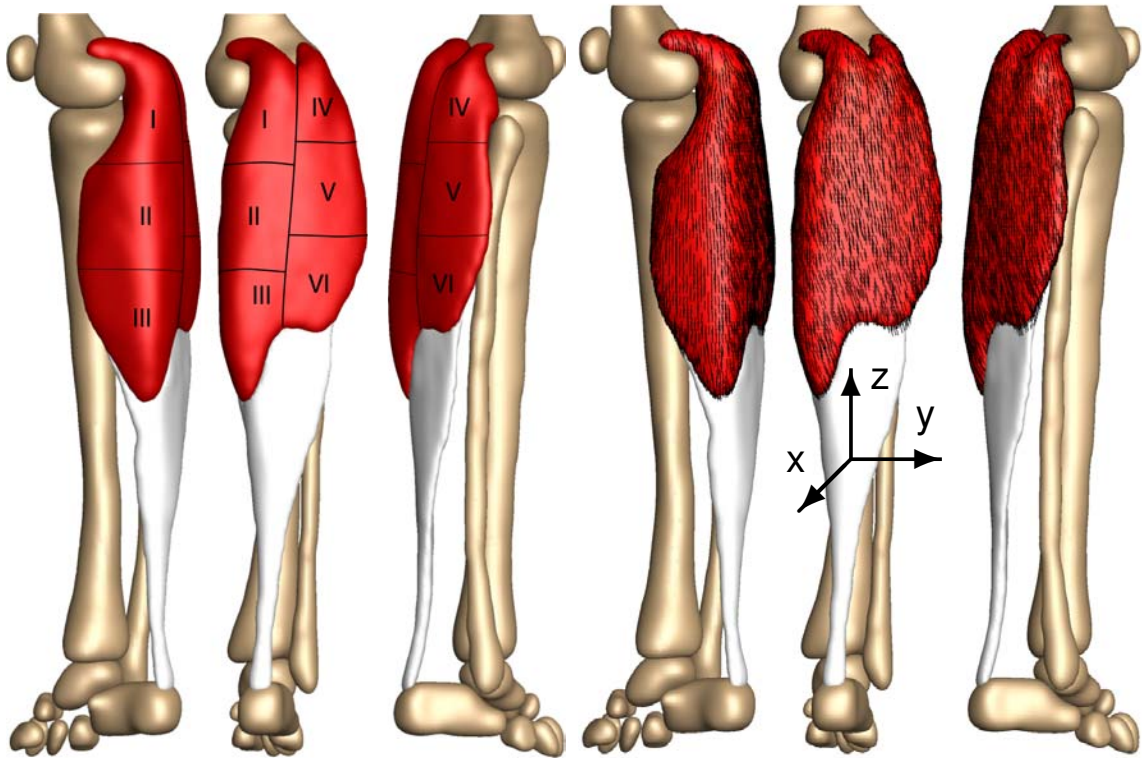


Figure 5.6: Muscle fiber orientation model of the gastrocnemius muscle. The gastrocnemius muscle (red) is a bipennate muscle. It consists of two rows of oblique muscle fibers, which face in opposite diagonal directions and converge in a joined tendon (grey). Table 5.2 summarizes the six characteristic regions of interest with their six discrete fiber orientations \mathbf{n}_0 [174].

Table 5.2: Muscle fiber orientations in the gastrocnemius muscle. The gastrocnemius muscle is a bipennate muscle. It consists of two rows of oblique muscle fibers, which face in opposite diagonal directions and converge in the Achilles tendon. Figure 5.6 illustrates six characteristic regions of interest with the six fiber orientations \mathbf{n}_0 [174].

region	location	n_{0x}	n_{0y}	n_{0z}
I	medial-proximal	0.014	-0.197	0.980
II	medial-central	0.025	-0.242	0.970
III	medial-distal	0.075	-0.317	0.946
IV	lateral-proximal	0.021	-0.193	0.981
V	lateral-central	0.024	-0.208	0.978
VI	lateral-distal	0.040	-0.247	0.968

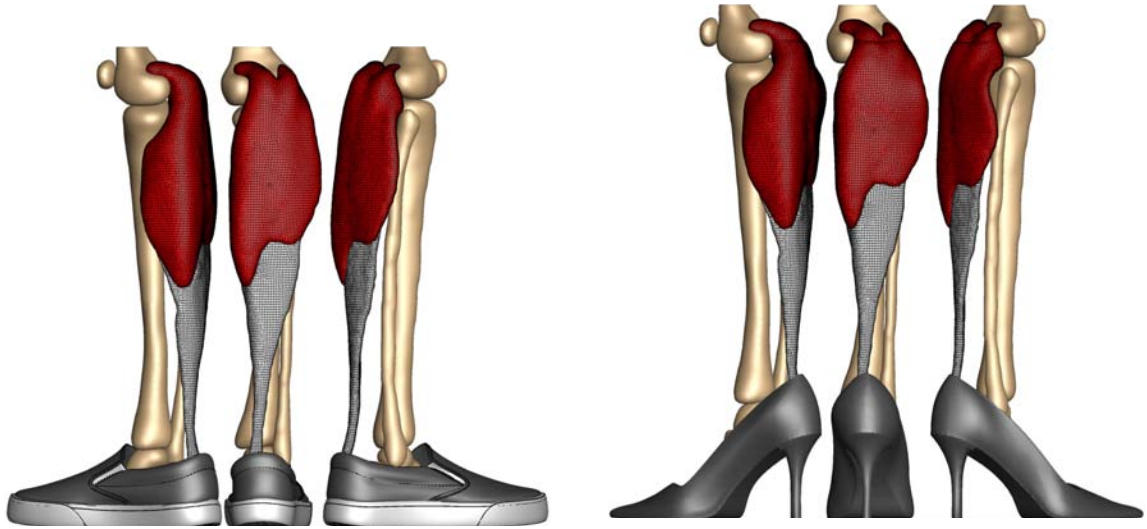


Figure 5.7: Finite element model of muscle shortening in response to frequent high heel use. The left model shows the baseline state created from magnetic resonance images in flat foot position. The right model shows the shortened state created from images in high heel position. To move the flat foot into the high heel position, we apply inhomogeneous Dirichlet boundary conditions by prescribing a 12 mm upward displacement of the distal end of the Achilles tendon. Then we maintain the foot in this position to allow the muscle to adapt to its new physiological length.

5.2.6 Boundary conditions

To explore the acute and chronic effects of global muscle shortening on local sarcomere lengths, we simulate three scenarios: (i) acute effects when changing from flat foot to high heel position, (ii) chronic effects when maintaining the high heel position, and (iii) acute effects when changing back from high heel to flat foot position.

Figure 5.7 illustrates our finite element model of the lower limb. The left model shows the baseline state created from magnetic resonance images in flat foot position. The right model shows the shortened state created from images in high heel position. First, we move the model from flat foot to high heel position by prescribing an upward displacement on the distal nodes of the Achilles tendon. Then, we keep the foot in this position and allow the gastrocnemius to shorten and adapt to its new physiological length. Last, after the muscle has adapted, we move the foot back into the flat foot position.

5.3 Results

All three simulations run robustly, converge quadratically, and generate conceptually feasible results, which we discuss in detail in the following three subsections.

5.3.1 Acute effects when switching from flat foot to high heel

Figure 5.8 illustrates the acute change in sarcomere length when switching from flat footwear to high heels. Wearing shoes with a heel height of 13 cm induces a muscle shortening of 12 mm. In response to acute muscle shortening, the sarcomere length decreases. A decrease in length places the sarcomeres into a non-optimal operating regime at $\lambda^e < 1.0$ and the whole muscle into an energetically unfavorable working range. Sarcomere lengths display significant regional variations with an extreme shortening of $l_s/l_0 = 0.78$ in the central gastrocnemius.

5.3.2 Chronic effects when switching from flat foot to high heel

Figure 5.9 illustrates the chronic change in sarcomere length in frequent high heel wearers. In response to chronic muscle shortening, the initially shortened sarcomere length increases gradually as the muscle remains in its shortened position. This repositions the sarcomeres back into their optimal operating regime at $\lambda^e = 1.0$. Initially, sarcomere lengths display significant regional variations with extreme values of $l_s/l_0 = 0.78$ located in the central gastrocnemius. Over time, these variations disappear. As the muscle adapts to its new physiological length, the sarcomere lengths converge towards a homogeneous distribution at their initial length l_0 .

Figure 5.10 illustrates the chronic change in sarcomere number in frequent high heel wearers. In response to chronic muscle shortening, the sarcomere number decreases gradually as the muscle remains in its shortened position. The average weighted sarcomere number gradually decreases from $\vartheta = 1.00$ to 0.96 after one week and 0.94 after two weeks until it converges to 0.91 after ten weeks of frequent high heel use. At this point, each sarcomere is repositioned back in its optimal operating regime.

The side-by-side comparison of Figures 5.9 and 5.10 illustrates the interplay between the elastic and inelastic fiber stretches λ^e and λ^g : Initially, changing from flat footwear to high heels compresses the muscle and the elastic fiber stretch drops significantly below its baseline value of one. On the sarcomere level, this implies significant sarcomere shortening and an increase in actin and myosin overlap. Over time, the relative serial sarcomere number decreases below its baseline value of one, while, at the same time, the sarcomere length returns to its initial value. The solution converges towards a state at which the elastic fiber stretch has returned to one throughout the entire muscle and the inelastic fiber stretch has taken up all the deformation.

Figures 5.9 and 5.10 indicate that the sarcomere loss is highly heterogeneous. At the proximal end of the gastrocnemius, where the medial and lateral heads attach to the rigid condyle of the femur, the muscle does not sense the kinematic change associated with wearing high heels. At its distal end, where the compliant muscle smoothly blends into the stiff Achilles tendon, relative kinematic changes are suppressed by the structural support of the tendon. Sarcomere loss is localized between these two regions with extreme values of $\vartheta = 0.61$ corresponding to a chronic local fiber shortening 39%.

acute decrease in sarcomere length / elastic fiber stretch

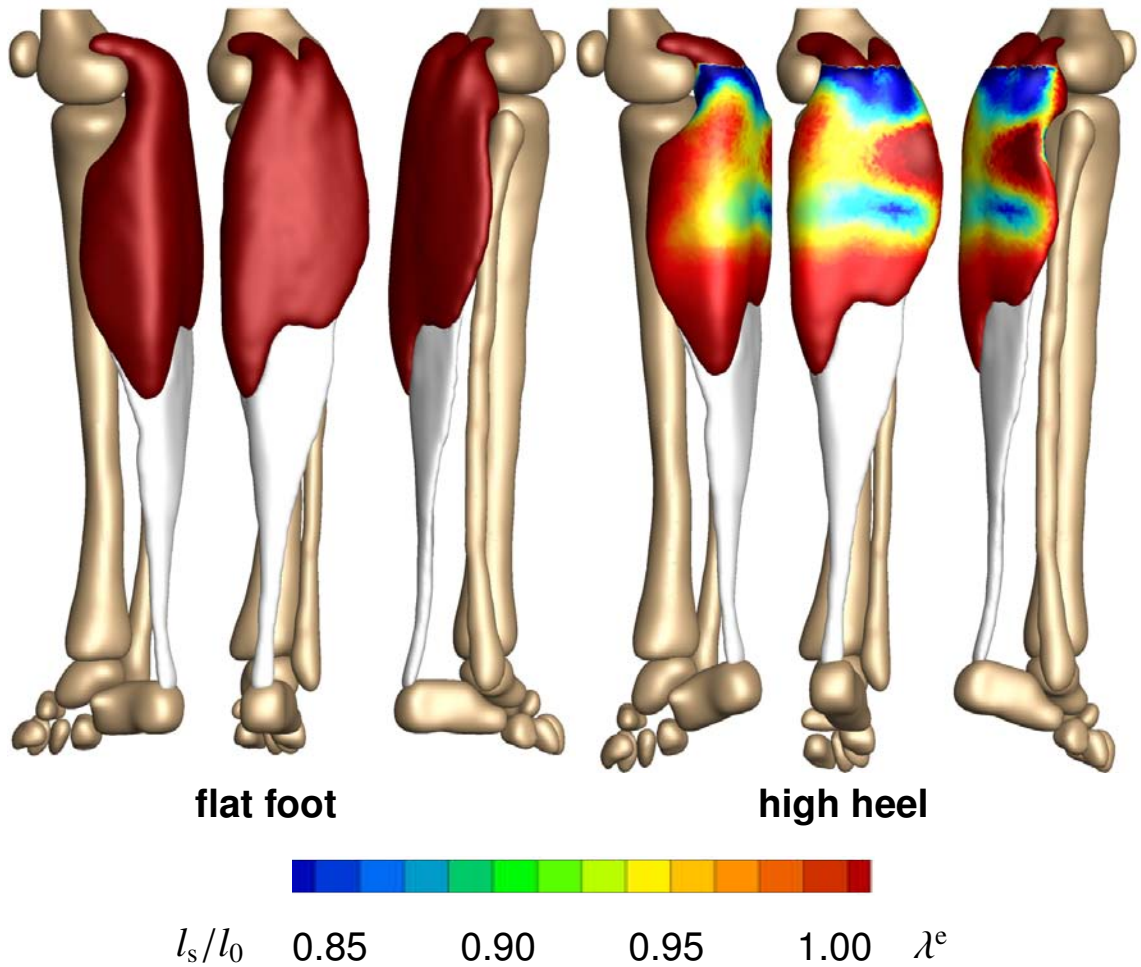


Figure 5.8: Acute decrease in sarcomere length when switching from flat footwear to high heels. In response to acute muscle shortening, the sarcomere length decreases. Sarcomere lengths display significant regional variations with extreme values of $l_s/l_0 = 0.78$ in the central gastrocnemius. The relative sarcomere length l_s/l_0 is a measure for the elastic fiber stretch λ^e .

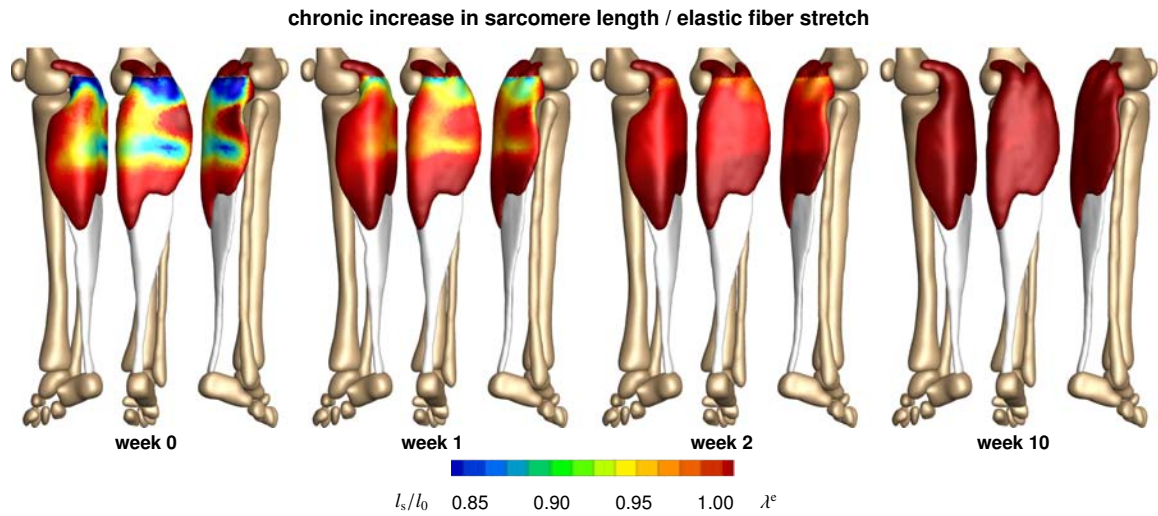


Figure 5.9: Chronic increase in sarcomere length when frequently wearing high-heeled footwear. In response to chronic muscle shortening, the sarcomere length increases gradually as the muscle remains in its shortened position. Sarcomere lengths display significant regional variations with extreme values of $l_s/l_0 = 0.78$ located in the central gastrocnemius. The relative sarcomere length l_s/l_0 is a measure for the elastic fiber stretch λ^e .

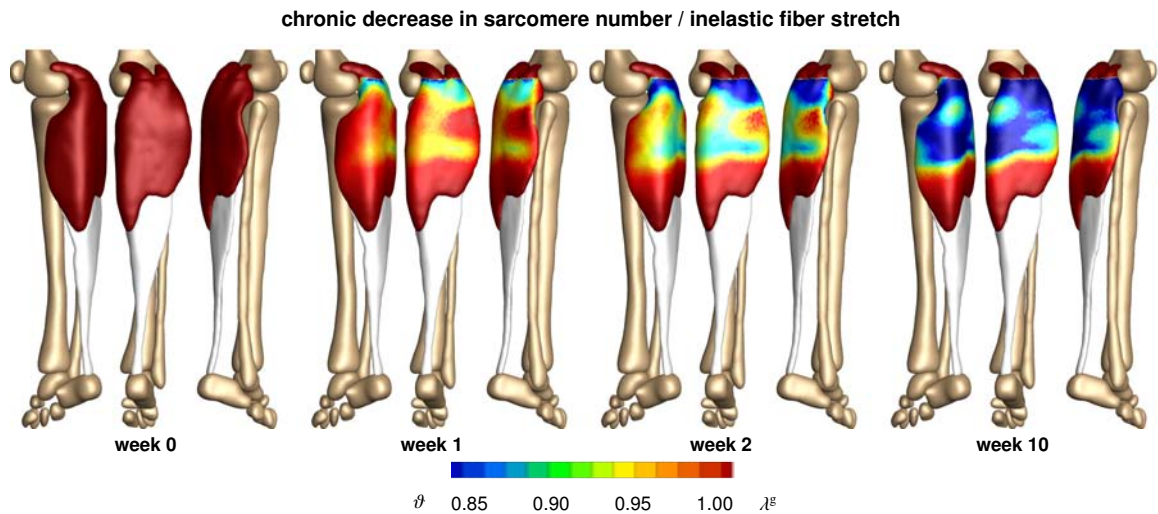


Figure 5.10: Chronic decrease in sarcomere number when frequently wearing high-heeled footwear. In response to chronic muscle shortening, the sarcomere number decreases gradually as the muscle remains in its shortened position. Sarcomere loss displays significant regional variations with extreme values of $\vartheta = 0.61$ located in the central gastrocnemius. The relative sarcomere number ϑ is a measure for the inelastic fiber stretch λ^e .

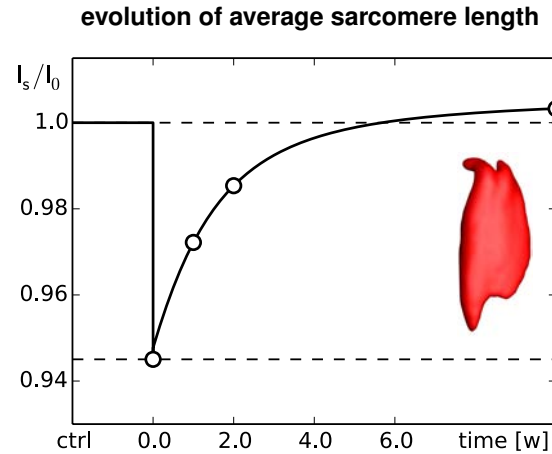


Figure 5.11: Chronic increase in sarcomere length when switching from flat footwear to high heels. In response to muscle shortening of 12 mm, the sarcomere length in the gastrocnemius muscle decreases acutely from $l_s/l_0 = 1.0$ to 0.95 and then returns chronically to its initial length. The marked time points correspond to the contour plots in Figure 5.9.

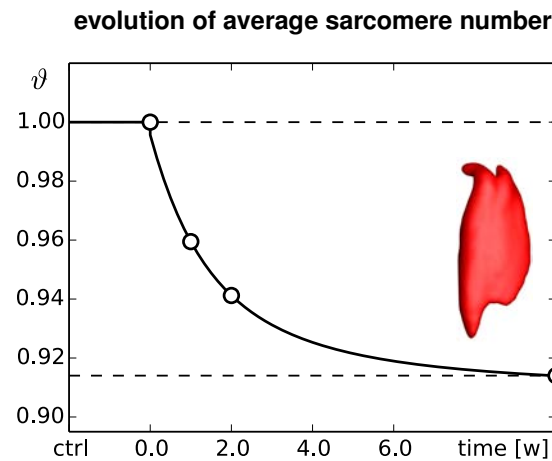


Figure 5.12: Chronic decrease in sarcomere number when switching from flat footwear to high heels. In response to muscle shortening of 12 mm, the sarcomere number in the gastrocnemius muscle decreases chronically from $v = 1.0$ to 0.96 after one week and 0.94 after two weeks until it converges at 0.91 after ten weeks. The marked time points correspond to the contour plots in Figure 5.10.

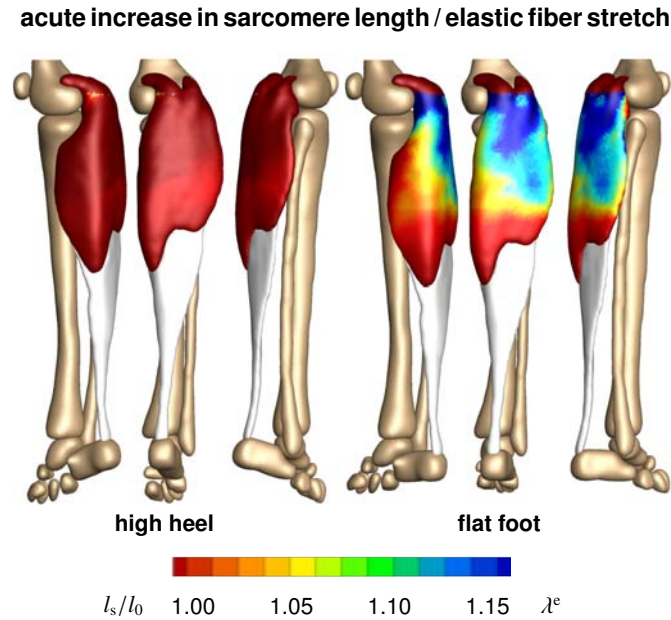


Figure 5.13: Acute increase in sarcomere length when switching from high heels to flat footwear. In response to acute muscle lengthening, the sarcomere length increases. Sarcomere lengths display significant regional variations with extreme values of $l_s/l_0 = 1.29$ located in the central gastrocnemius. The relative sarcomere length l_s/l_0 is a measure for the elastic fiber stretch λ^e .

Figures 5.11 and 5.12 summarize the dynamic changes in sarcomere length and sarcomere number. Both graphs reflect the interplay between elastic and inelastic fiber stretch with a gradual transition from acute sarcomere shortening with $\lambda^e < 1$ at $\lambda^g = 1$ to chronic sarcomere loss with $\lambda^g < 1$ at $\lambda^e = 1$. Since the graphs contain the averaged values across the entire muscle, the minimum average sarcomere length and average sarcomere number of 0.94 and 0.91 are less pronounced than the local extreme values of 0.78 and 0.61 of the contour plots in Figures 5.9 and 5.10.

5.3.3 Acute effects when switching from high heel to flat foot

Figure 5.13 illustrates the acute change in sarcomere length when switching back to flat foot position after a period of extended high heel wearing. In response to acute muscle lengthening, the sarcomere length increases. An increase in length places the sarcomeres into a non-optimal operating regime at $\lambda^e > 1.0$. Sarcomere lengths display significant regional variations with an extreme lengthening of $l_s/l_0 = 1.29$ in the central gastrocnemius.

5.4 Discussion

Even though high heels are known to be a major source of chronic lower limb pain, more than one third of American women wear high heels on a daily basis. To characterize the effects of high-heeled footwear on muscle adaptation in the lower limb, we created a multiscale computational model for chronic muscle shortening. To calibrate the model, we performed a case study of a healthy female subject and created two lower limb models using magnetic resonance images, one in flat foot and one in high heel position. Surprisingly, when moving the foot from flat position to a heel height of 13 cm, the length of the calf muscle-tendon unit changes only marginally from 396 mm to 384 mm corresponding to a stretch of $\lambda = 0.97$. However, a closer look reveals two essential characteristics: The Achilles tendon remains at a constant length of 171 mm with $\lambda = 1.00$, while the gastrocnemius experiences the entire length change of 12 mm from 225 mm to 213 mm corresponding to a stretch of $\lambda = 0.95$. More importantly, the finite element simulation suggests that this stretch is not distributed homogeneously across the gastrocnemius muscle: In the proximal and distal regions, where the muscle is structurally supported by the stiffer femur and Achilles tendon, the muscle experience virtually no stretch; in the central muscle region, local stretches take extreme values of $\lambda = 0.78$. Acutely, switching from flat footwear to high heels causes excessive actin-myosin overlap and forces the muscle to operate in a non-optimal operating regime [52], see Figure 5.2. When moving from the flat to the high heel position, our simulations predict an acute average reduction in sarcomere length by 5%, see Figure 5.11, with local extrema of sarcomere shortening of 22% in the central gastrocnemius, see Figure 5.9. These values are in excellent agreement with recent studies, which have reported a fascicle length difference of 12% in the medial gastrocnemius muscle, with lengths of 56.0 ± 7.7 mm in the flat foot group compared to 49.6 ± 5.7 mm in the high heel group [51]. In the same study, in agreement with our measurements and simulations, the length of the Achilles tendon was almost identical in both groups with 18.69 cm in the flat foot group and 18.91 cm in the high heel group [51].

Chronically, skeletal muscle adapts to its new physiological length by removing sarcomeres in series to reposition its sarcomeres back into their optimal regime [214], see Figure 5.2. When maintaining the foot in the high heel position, our simulations predict a chronic average reduction in serial sarcomere number by 9%, see Figure 5.12, with local maxima of sarcomere loss of 31% in the central gastrocnemius, see Figure 5.10. These values lie within the range of the reported sarcomere loss during immobilization experiments in mice, where the serial sarcomere number decreased by 10% from 2,200 to 1,975 in the soleus after four weeks of immobilization [215] and by 9% from 3,200 to 2,900 in the tibialis anterior after two weeks of immobilization [40]. These values are slightly lower than the reported sarcomere loss in cat, where the serial sarcomere number decreased by 40% from 13,844 to 8,258 in the soleus after four weeks of immobilization [196]. Undoubtedly, these immobilization experiments impose a more drastic kinematic constraint than frequent high heel wearing [59]. Nonetheless, the chronic sarcomere loss reported upon immobilization represents a valuable upper

limit for the sarcomere loss we can expect in women who frequently wear high-heeled shoes.

Acutely, switching back from frequent high heel use to flat footwear causes a drastic reduction in actin-myosin overlap and forces the muscle to operate in a non-optimal operating regime [76], see Figure 5.2. When moving from the foot from high heel to flat, our simulations predict an acute sarcomere lengthening with local extrema of 29% in the central gastrocnemius, see Figure 5.13. Our large regional variations in sarcomere length are in agreement with previous studies, which have reported significant regional variations in fascicle lengths and sarcomere lengths in the stretched cat biceps femoris muscle [46]. Our sarcomere lengths agree with common observation that switching back from high heels to flat footwear induces muscle overstretch associated with muscle pain [105] and increased risk of strain injuries [52].

While our study provides valuable insight into the mechanisms of chronic muscle shortening on the muscle and sarcomere levels, our current model has a few limitations: First, to illustrate the conceptual feasibility of our method, we have only prototyped the study for a single heel height and a single study subject. It would be interesting to explore the dimensions of the muscle-tendon unit in Table 5.1 for flat foot and high heel positions with varying heel heights in different study subjects [60]. Second, for simplicity, in equation (5.8), we have modeled skeletal muscle as isotropic Neo-Hookean material. While an isotropic model might be a sufficient approximation under compressive loading when switching from flat foot to high heel, a more sophisticated anisotropic model that takes into account strain stiffening might be more appropriate under tensile loading when switching from high heel to flat foot [26, 74]. Since we have only reported strains and stretches, here, sophisticated constitutive modeling might not be critical; yet, it would be worth considering in future studies, especially when addressing chronic force alterations in muscle [103] and tendon [63, 142]. Third, the model presented here only accounts for sarcomere removal upon chronic understretch. To add sarcomeres in series upon chronic overstretch [217], we would need to modify the adaptation function in equation (5.11) to $k = [(\vartheta^{\max} - \vartheta)/(\vartheta^{\max} - 1)]^\gamma/\tau$ and activate it through the modified adaptation criterion in equation (5.12) as $\phi = \langle \lambda^e - \lambda^{\text{crit}} \rangle$ using the generic approach [139] adopted for skeletal muscle [225]. Last, until now, we have only compared our model qualitatively against animal immobilization models in mice [215] and cat [196]. Recent developments in microendoscopy now enable the non-invasive sarcomere imaging in vivo [136]. We have designed our model with these new technologies in mind [50]. We are currently in the process of measuring sarcomere lengths in flat foot and high heel positions in different regions of the gastrocnemius muscle to validate our model with in vivo human data.

What can we learn from this study? First and foremost, we have seen that we can interpret chronic changes in whole muscle length as emergent properties of local changes in sarcomere number, muscle fiber length, and fascicle length. This has allowed us to create multiscale computational models, which strongly support the hypothesis that frequent high-heel use alters the natural position of the calf muscle-tendon complex. Our results suggest that this change could initiate a chain reaction of

negative effects [53]: Acutely, it creates excessive actin-myosin overlap associated with energetically inefficient muscle use [60]. Chronically, it initiates an adaptation process associated with the loss of sarcomeres and significant muscle shortening [51]. A major concern is that these changes are chronic. Changing back to flat footwear does not provide immediate cure; quite the contrary: For most frequent high heel wearers, switching to the flat foot position can be extremely painful. It overstretched the triceps surae [105], which might cause muscle pain and planar fasciitis [156]. To ensure comfort and reduce risk of injury [52], recent recommendations suggest limiting the heel height to 5 cm or less [60]. To maintain muscle fiber lengths and ankle range of motion [105], recent studies recommend intensive passive stretching exercise with long frequent stretching times in dorsiflexion direction [103]. Our study strongly supports these recommendations.

5.5 Concluding remarks

We have created a computational model of the lower limb to study the acute and chronic effects of high-heeled footwear on the kinematics of the calf muscle-tendon unit. Through the case study of a healthy female subject, we have shown that raising the heel by 13 cm reduces the length of the muscle-tendon unit by 12 mm or 3%. Notably, this change affects almost exclusively the gastrocnemius muscle, which experiences an average shortening of 5%, while the length of the Achilles tendon remains virtually unchanged. Our computational simulations indicate that muscle shortening displays significant regional variations with extreme values of 22% in the central gastrocnemius. Our model suggests that the muscle gradually adjusts to its new functional length by a chronic loss of sarcomeres in series. Sarcomere loss varies regionally with virtually no loss at the proximal and distal ends and a maximum loss of 39% in the central muscle region. Collectively, these changes result in chronic muscle shortening associated with discomfort, compromised muscle efficiency, increased fatigue, reduced shock absorption, and increased risk of strain injuries. Computational modeling of chronic muscle shortening provides a valuable tool to shape our understanding of the interacting mechanisms in skeletal muscle adaptation. Our study could open new avenues in orthopedic surgery and enhance treatment in patients with muscle contracture caused by other conditions than high heel wear such as paralysis, muscular atrophy, and muscular dystrophy.

Acknowledgments

We thank Professor Gerald E. Loeb for stimulating discussions that initiated this study. This research was supported by the Stanford Graduate Fellowship to Alexander Zöllner, by the Stanford Mechanical Engineering SURI support to Jacquelynn Pok, by the NSERC PDF Fellowship to Emily McWalter, by GE Healthcare, by the NIH grant NIH EB002524, and by the NIH grant AR062068 to Garry Gold, and by the NSF CAREER award CMMI 0952021, by the NSF INSPIRE grant 1233054,

and by the NIH grant U01 HL119578 to Ellen Kuhl.

Chapter 6

A virtual sizing tool for mitral valve annuloplasty

Abstract

Functional mitral regurgitation, a backward leakage of the mitral valve, is a result of left ventricular growth and mitral annular dilatation. Its gold standard treatment is mitral annuloplasty, the surgical reduction in mitral annular area through the implantation of annuloplasty rings. Recurrent regurgitation rates may, however, be as high as 30% and more. While the degree of annular downsizing has been linked to improved long-term outcomes, too aggressive downsizing increases the risk of ring dehiscences and significantly impairs repair durability. Here we prototype a virtual sizing tool to quantify changes in annular dimensions, surgically-induced tissue strains, mitral annular stretches, and suture forces in response to mitral annuloplasty. We create a computational model of dilated cardiomyopathy onto which we virtually implant annuloplasty rings of different sizes. Our simulations confirm the common intuition that smaller rings are more invasive to the surrounding tissue, induce higher strains, and require larger suture forces than larger rings: The total suture force was 2.2N for a 24mm ring, 1.9N for a 28mm ring, and 0.8N for a 32mm ring. Our model predicts the highest risk of dehiscence in the septal and postero-lateral annulus where suture forces are maximal. These regions co-localize with regional peaks in myocardial strain and annular stretch. Our study illustrates the potential of realistic predictive simulations in cardiac surgery to identify areas at risk for dehiscence, guide the selection of ring size and shape, rationalize the design of smart annuloplasty rings and, ultimately, improve long-term outcomes after surgical mitral annuloplasty.

6.1 Motivation

Functional mitral regurgitation is a backward leakage of the mitral valve in the absence of any disease to the valve itself [122, 157, 179]. A major cause of functional mitral regurgitation is dilated

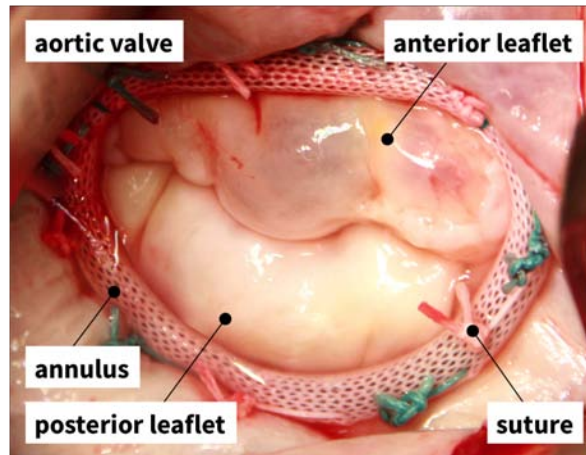


Figure 6.1: Mitral annuloplasty

cardiomyopathy, in which pathologic remodeling of the myocardium results in increased chamber size [66]. During the course of dilated cardiomyopathy, the growing ventricle dilates the mitral annulus and increases tension on the chordae tendineae [108]. These pathological forces on annulus and chordae eventually render the mitral valve unable to seal against systolic blood pressure, resulting in retrograde blood flow, further reduction in ejection fraction, arrhythmic disorder, and increased risk for myocardial infarction [131].

Mitral valve annuloplasty, as illustrated in Figure 6.1, remains the number one surgical treatment for functional mitral regurgitation [123,146,190]. Correcting the distorted mitral annulus through the implantation of undersized annuloplasty prostheses has been shown to temporarily improve symptoms of functional mitral regurgitation. However, to date, there is no accepted standard for the optimal ring choice or degree of downsizing [32,177]. Recent studies have shown that a large population of patients treated with undersized annuloplasty show recurrent mitral regurgitation and require re-operation [146,201]. Continued ventricular remodeling might be responsible for the return of mitral regurgitation and for the suboptimal long-term results of undersized annuloplasty [127].

We propose that successful mitral annuloplasty is a compromise between fixing the leaking valve and minimizing the insult to the surrounding tissue [177]. The heart, both in a physiological and pathological setting, responds to mechanical stimuli to maintain a homeostatic equilibrium state [92,228]. In dilated cardiomyopathy, the ventricular myocardium dilates in response to myocardial infarction or other insults to the myocardial tissue to establish a new state of mechanical equilibrium [69,178]. The implantation of an undersized annuloplasty ring, initially aimed at surgically reversing the effects of ventricular remodeling, induces additional non-homeostatic deformations and forces in the surrounding tissue [18,30]. Long-term, these alterations trigger changes in flow conditions and continued ventricular remodeling [128], which can ultimately render the original intervention

suboptimal. Quantifying surgically-induced forces is an important first step towards an improved understanding of the effects of undersized annuloplasty on the mitral valve and the surrounding myocardium. To date, there is neither a model to quantify surgical strains and forces, nor a tool to optimize ring choice and the degree of undersizing.

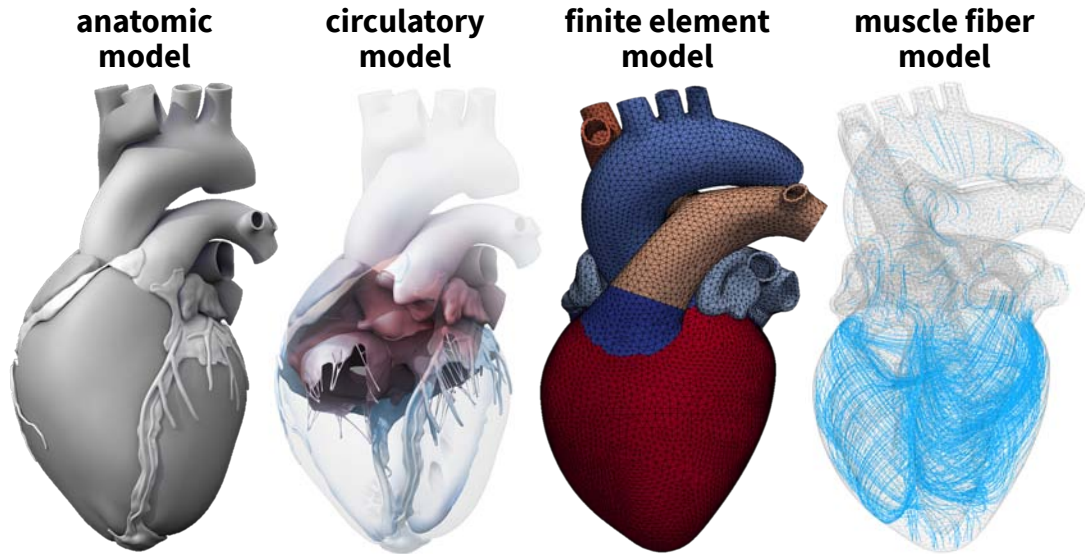


Figure 6.2: The Living Heart model

Simulating the human heart—with all four chambers and valves—is increasingly recognized as a critical step towards quantifying myocardial strain and stress [18]. Until recently, whole heart simulations were virtually impossible because of insufficient medical image resolution and a lack of computational power. Recent advances in non-invasive imaging and computer simulation now allow us to create three-dimensional models of the entire human heart [231]. Figure 6.2 illustrates the Living Heart model, a high-fidelity multiphysics model of a healthy, four-chamber adult human heart and its proximal vasculature [17]. Created from computer tomography and magnetic resonance images, the Living Heart model consist of 47,323 nodes, 141,969 degrees of freedom, and 208,561 linear tetrahedral elements with individual fiber and sheet directions [219]. Combined with algorithms of growth and remodeling [176], it allows us to reliably predict alterations in cardiac form and function during dilated cardiomyopathy [69]. Here we use the dilated Living Heart model as a starting point to quantify surgically-induced strains and forces in response to mitral annuloplasty.

The objective of this manuscript is two-fold: First, we quantify the geometric size reduction, mitral annular stretches, and mitral valvular strains in response to different degrees of downsizing using the dilated Living Heart model; second, we quantify the suture forces associated with annular downsizing to characterize the trade-off between maximizing the degree of repair and minimizing the insult to

the surrounding tissue. Our overall goal is to prototype a virtual surgical tool for the optimal design and selection of cardiovascular devices using predictive computational simulation.

6.2 Methods

6.2.1 Cardiac Growth Model

To create the geometry of dilated cardiomyopathy, we multiplicatively decompose the deformation gradient \mathbf{F} , the spatial gradient of the deformation map φ , into an elastic part \mathbf{F}^e and a growth part \mathbf{F}^g [183],

$$\mathbf{F} = \mathbf{F}^e \cdot \mathbf{F}^g \quad \text{with} \quad \mathbf{F} = \nabla_{\mathbf{X}} \varphi. \quad (6.1)$$

To account for quasi-incompressibility of the elastic tissue response, we further decompose the elastic tensor \mathbf{F}^e into volumetric and isochoric parts,

$$\mathbf{F}^e = \mathbf{F}_{\text{vol}}^e \cdot \bar{\mathbf{F}}^e \quad \text{with} \quad \mathbf{F}_{\text{vol}}^e = (J^e)^{1/3} \mathbf{I} \quad \text{and} \quad \bar{\mathbf{F}}^e = (J^e)^{-1/3} \mathbf{F}^e. \quad (6.2)$$

Here \mathbf{I} denotes the second-order unit tensor, $J^e = \det(\mathbf{F}^e) = J_{\text{vol}}^e$ is the elastic Jacobian and $\bar{J}^e = \det(\bar{\mathbf{F}}^e) = 1$ is the isochoric Jacobian [90]. We can now characterize the elastic deformation in terms of the elastic Jacobian J^e and the isochoric elastic Green-Lagrange strain tensor $\bar{\mathbf{E}}^e$,

$$J^e = \det(\mathbf{F}^e) \quad \text{and} \quad \bar{\mathbf{E}}^e = \frac{1}{2} [(J^e)^{-2/3} (\mathbf{F}^e)^t \cdot \mathbf{F}^e - \mathbf{I}]. \quad (6.3)$$

The underlying principle of the theory of finite growth is that only elastic deformations generate stress. We thus introduce the following strain energy function $\psi(J^e, \bar{\mathbf{E}}^e)$,

$$\psi(J^e, \bar{\mathbf{E}}^e) = U(J^e) + \bar{\psi}(\bar{\mathbf{E}}^e), \quad (6.4)$$

which we decompose additively into a volumetric part $U(J^e)$ and an isochoric part $\bar{\psi}(\bar{\mathbf{E}}^e)$,

$$U(J^e) = \frac{1}{2} K_0 [(J^e)^2 - 2 \ln(J^e)] \quad \text{and} \quad \bar{\psi}(\bar{\mathbf{E}}^e) = \frac{1}{2} C_0 [\exp(\bar{\mathbf{E}}^e : \mathbf{B}_0 : \bar{\mathbf{E}}^e) - 1]. \quad (6.5)$$

Here K_0 and C_0 are the volumetric and isochoric elastic stiffnesses, and the fourth-order tensor \mathbf{B}_0 contains the weighting factors of the orthotropic Fung-type model for myocardial tissue [84]. In Voigt notation, \mathbf{B}_0 takes a diagonal representation, $\widehat{\mathbf{B}}_0 = \text{diag} \{ B_{\text{ff}}, B_{\text{ss}}, B_{\text{nn}}, 2B_{\text{fs}}, 2B_{\text{fn}}, 2B_{\text{sn}} \}$, where the individual entries are the weights of the normal and shear strains in the fiber, sheet, and normal directions. According to the standard arguments of thermodynamics, the Piola-Kirchhoff

stress \mathbf{S} follows as thermodynamically conjugate to the Green-Lagrange strain $\mathbf{E} = \frac{1}{2} [\mathbf{F}^t \cdot \mathbf{F} - \mathbf{I}]$,

$$\mathbf{S} = \frac{\partial \psi}{\partial \mathbf{E}} = \frac{\partial \psi}{\partial \mathbf{E}^e} : \frac{\partial \mathbf{E}^e}{\partial \mathbf{E}} = (\mathbf{F}^g)^{-1} \cdot \mathbf{S}^e \cdot (\mathbf{F}^g)^{-t}. \quad (6.6)$$

The above relation suggests to interpret the Piola Kirchhoff stress \mathbf{S} as the pull back of the elastic Piola Kirchhoff stress \mathbf{S}^e , which is thermodynamically conjugate to the elastic Green-Lagrange strain, $\mathbf{E}^e = \frac{1}{2} [(\mathbf{F}^e)^t \cdot \mathbf{F}^e - \mathbf{I}]$,

$$\mathbf{S}^e = \frac{\partial \psi}{\partial \mathbf{E}^e} = \mathbf{S}_{\text{vol}}^e + \mathbf{S}_{\text{iso}}^e = \frac{\partial U}{\partial \mathbf{E}^e} + \frac{\partial \bar{\psi}}{\partial \mathbf{E}^e}. \quad (6.7)$$

To model cardiac dilation through chronic cardiomyocyte lengthening, we introduce a scalar-valued growth multiplier ϑ that reflects the serial deposition of sarcomeres along the fiber direction \mathbf{f}_0 [71]. The growth tensor \mathbf{F}^g and the elastic tensor \mathbf{F}^e then take a simple rank-one update structure,

$$\mathbf{F}^g = \mathbf{I} + [\vartheta - 1] \mathbf{f}_0 \otimes \mathbf{f}_0 \quad \text{and} \quad \mathbf{F}^e = \mathbf{F} + \frac{1 - \vartheta}{\vartheta} \mathbf{f} \otimes \mathbf{f}_0, \quad (6.8)$$

where $\mathbf{f} = \mathbf{F} \cdot \mathbf{f}_0$. This implies that the growth multiplier $\vartheta = \det(\mathbf{F}^g) = J^g$ not only characterizes the local muscle cell lengthening but also the local volume change J^g . We assume that chronic cardiomyocyte lengthening is induced by mechanical overstretch [101],

$$\dot{\vartheta} = \frac{1}{\tau} \langle \lambda - \lambda^{\text{crit}} \rangle \quad \text{with} \quad \lambda = [\mathbf{f}_0 \cdot \mathbf{F}^t \cdot \mathbf{F} \cdot \mathbf{f}_0]^{1/2}, \quad (6.9)$$

where the term in the Macaulay brackets ensures that growth is activated only if the current fiber stretch λ exceeds the physiological stretch limit λ^{crit} . We calculate λ^{crit} as a regionally varying baseline stretch under physiological conditions. The parameter τ characterizes the timeline of dilated cardiomyopathy.

We implement the cardiac growth model as a user defined subroutine into the non-linear finite element program Abaqus/Standard version 6.13 [2]. We represent the growth multiplier ϑ as an internal variable and store the current growth state locally on the integration point level. For a given deformation state \mathbf{F} , we evolve the growth multiplier in time using a finite difference approximation of the first order time derivative, $\dot{\vartheta} = [\vartheta - \vartheta_n]/\Delta t$, where ϑ_n denotes the growth multiplier of the previous time step and $\Delta t = t - t_n$ is the current time increment. We update the growth multiplier of the current time step according to the evolution equation (6.9) as $\vartheta = \vartheta_n + \langle \lambda - \lambda^{\text{crit}} \rangle \Delta t / \tau$. From the updated growth state, we successively calculate the elastic tensor \mathbf{F}^e using equation (6.8.2), the elastic Jacobian J^e and the isochoric elastic Green-Lagrange strain tensor $\bar{\mathbf{E}}^e$ using equations (6.3.1) and (6.3.2), and the Piola Kirchhoff stress \mathbf{S} using equation (6.6). Rather than working with the Piola Kirchhoff stress \mathbf{S} , Abaqus/Standard uses the Cauchy stress $\boldsymbol{\sigma} = \mathbf{F} \cdot \mathbf{S} \cdot \mathbf{F}^t / J$ where $J = \det(\mathbf{F})$. To ensure optimal quadratic convergence of the Newton-Raphson procedure during

the global equilibrium iteration, Abaqus/Standard requires the Jaumann rate of the Kirchhoff stress $\tau = J \dot{\sigma}$ [69].

6.2.2 Living Heart Model

Figure 6.2, left, illustrates the Living Heart model, an anatomically accurate four-chamber model of the healthy human heart that provides the basis for our simulation [17]. The underlying anatomic model was created from magnetic resonance images of a healthy, 21-year old, 50th percentile U.S. male. Images were reconstructed from 0.75mm thick slices using a medium soft-tissue kernel with retrospective electrocardiogram gating [232]. The initial DICOM images were exported as JPEG files, segmented using Amira, post-processed using Maya, and converted into NURBS surfaces, from which the final solid model was created. Figure 6.2, center left, illustrates the resulting geometric model of the heart with all four chambers, the left and right atria and the left and right ventricles, connected by the four valves [231]. Figure 6.2, center right, illustrates the finite element model of the Living Heart discretized with 208,561 linear tetrahedral elements and 47,323 nodes. This discretization introduces 141,969 degrees of freedom for the vector-valued deformation φ and 208,561 internal variables for the growth multiplier ϑ . Figure 6.2, right, shows the muscle fiber model with 208,561 discrete fiber vectors \mathbf{f}_0 wrapping helically around the heart and 208,561 discrete sheet vectors \mathbf{s}_0 pointing transmurally outward [219]. To fix the heart in space, we apply homogeneous Dirichlet boundary conditions at the geometric centers of the in- or outlets of all blood vessels. To prescribe different pressure values in each chamber, we model all valves in a fully closed state.

6.2.3 Dilated Cardiomyopathy Model

To calibrate the model at its healthy baseline state, we adopt the averaged patient-specific parameter values from an in vivo inverse finite element analysis of five healthy human hearts, three male and two female, age 36 ± 11 years [68]. Specifically, we select the volumetric stiffness in (6.5.1) to $K_0 = 1,000$ kPa and use a transversely isotropic version of the isochoric model (6.5.2), which we further reduce to two independent parameters, the isochoric stiffness C_0 and the nonlinearity parameter B_0 . We scale the fiber stiffness to $B_{\text{ff}} = B_0$, the transverse stiffnesses to $B_{\text{ss}} = B_{\text{nn}} = 0.4 B_0$, and the shear stiffnesses to $B_{\text{sn}} = 0.2 B_0$ and $B_{\text{fs}} = B_{\text{fn}} = 0.35 B_0$ [68]. Using the five subject-specific sets of magnetic resonance images, we identify the two isochoric parameters to $C_0 = 0.115 \pm 0.008$ kPa and $B_0 = 14.4 \pm 3.2$ such that $B_{\text{ff}} = 14.4$, $B_{\text{ss}} = B_{\text{nn}} = 5.76$, $B_{\text{sn}} = 2.88$, and $B_{\text{fs}} = B_{\text{fn}} = 5.04$. To identify the growth threshold λ^{crit} in equation (6.9), we train the model with its baseline conditions. We simulate the physiological end-diastolic state by applying a left ventricular and atrial pressure of 5 mmHg and a right ventricular and atrial pressure of 2 mmHg. For each integration point, we record the physiological fiber stretch $\lambda = [\mathbf{f}_0 \cdot \mathbf{F}^t \cdot \mathbf{F} \cdot \mathbf{f}_0]^{1/2}$ and store it locally as the growth threshold λ^{crit} . To model overload-induced cardiac dilation, we double the left ventricular and atrial pressures towards an end-diastolic pressure of 10 mmHg, while keeping the right ventricular and

arterial pressures at their baseline value of 2 mmHg. We gradually increase the pressure, keep it at its maximum value to allow the ventricles to grow, and then unload the heart. We only consider growth in the ventricles, not in the atria and main blood vessels.

6.2.4 Mitral Annuloplasty Model

We use the dilated heart to simulate the effects of mitral annuloplasty and quantify mitral annular changes after implantation of rings in three different sizes. We select the commonly used Carpentier-Edwards Physio ring as a typical example of a semi-rigid, closed annuloplasty ring and virtually implant rings with 24 mm, 28 mm, and 32 mm diameter onto the dilated annulus [31, 44].

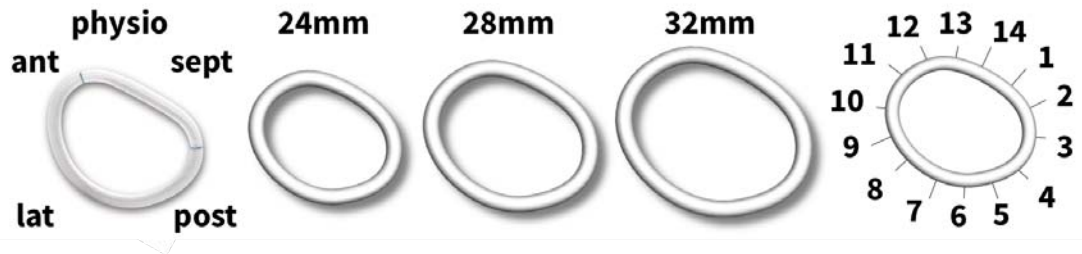


Figure 6.3: Using the Living Heart model as virtual sizing tool for mitral annuloplasty

Figure 6.3 illustrates the Carpentier-Edwards Physio ring, its reconstructed geometries with 24 mm, 28 mm, and 32 mm diameter, and its fourteen sutures for virtual ring implantation (right). The mechanical design goal of the Physio ring is to remodel the mitral annulus while maintaining coaptation and valve integrity in systole and permitting good hemodynamics in diastole [177]. We position the ring into the dilated mitral annulus and represent its sutures using fourteen one-dimensional connector elements. We record the suture forces as we reduce the length of the connector elements to zero.

6.3 Results

6.3.1 Dilated Cardiomyopathy

Before we employ the Living Heart model to elucidate the effects of undersized annuloplasty, we create the geometry of a dilated human heart using the theory of finite growth.

Ventricular Remodeling.

Figure 6.4 illustrates the two chamber and four chamber views of the heart before and after ventricular remodeling in response to diastolic overload. The color code indicates the growth multiplier ϑ , which varies from the baseline state with $\vartheta = 1.0$, shown in blue, to the dilated state with up to $\vartheta = 2.0$, shown in red. Stretch-induced overload of the left ventricle results in significant ventricular

dilation driven largely by changes in the antero-septal region. Specifically, the basal portion of the left ventricle, close to the mitral valve, displays the largest degree of dilation.

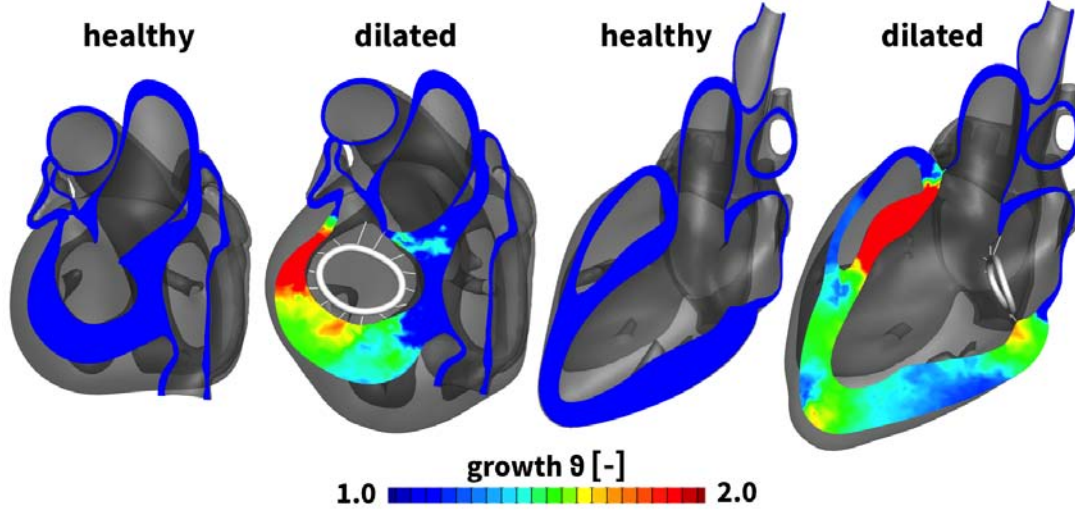


Figure 6.4: Two chamber and four chamber views of the heart before and after ventricular remodeling in response to diastolic overload

Annular Dilation.

Figure 6.5 highlights the geometry of the mitral annulus before and after ventricular remodeling in response to diastolic overload. Overload-induced remodeling in the myocardial tissue directly affected the size and geometry of the mitral annulus. The annular stretch λ characterizes chronic annular dilation from the healthy, ungrown state with $\lambda = 1.0$, shown in blue, to the dilated state up to $\lambda = 2.0$, shown in red. Annular dilation is largest in the anterior region, while the posterior region displays the least growth. Naturally, mitral annular dilation is co-localized with growth-induced deformations of the surrounding myocardial tissue highlighted in Figure 6.4.

Table 6.1: Annular dimensions of healthy and dilated annulus

	mitral annular area [mm ²]	mitral annular perimeter [mm]	septal-lateral distance [mm]	comm-comm distance [mm]
healthy	581.05	88.07	27.47	23.72
dilated	988.01	116.50	36.14	36.66

Table 6.1 summarizes the mitral annular area, mitral annular perimeter, septal-lateral distance, and commissure-commissure distance for the healthy and dilated hearts. Specifically, the mitral annular area increases from 581.05 mm² to 988.01 mm², a degree of dilation that has previously

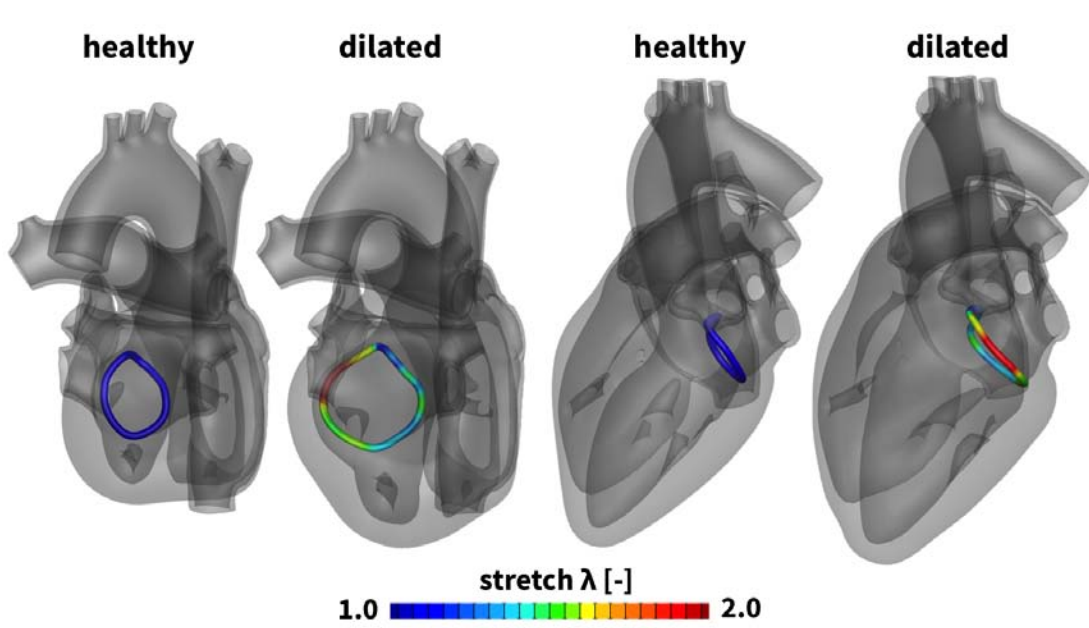


Figure 6.5: Two chamber and four chamber views of the heart before and after annular dilation in response to diastolic overload

been reported to result in severe mitral regurgitation. Changes in the septal-lateral and commissure-commissure distances from 27.47 mm and 23.72 mm to 36.14 mm and 36.66 mm indicate a significant circularization of the mitral annulus.

6.3.2 Mitral Annuloplasty

We now use the dilated Living Heart model to explore the effects of mitral annuloplasty on annular geometry, annular dilation, and the mechanics of the peri-annular tissues. To highlight the potential of the Living Heart model as a virtual sizing tool, we implant three common rings of standard sizes 24, 28, and 32 mm diameter.

Ventricular Effects.

Figure 6.6 illustrates the two chamber and four chamber views after the implantation of all three rings. The color code indicates the surgically induced maximum principal stretch λ^{\max} , which varies from the baseline state $\lambda^{\max} = 1.0$, shown in blue, to a maximum stretch state of $\lambda^{\max} = 1.3$, shown in red. From a mechanical perspective, ring implantation induces the largest stretches septally toward the aorto-mitral junction and in the postero-lateral region. Surgically induced maximum stretches were $\lambda^{\max} = 1.30$ for the 24 mm-diameter ring, $\lambda^{\max} = 1.24$ for the 28 mm-diameter ring, $\lambda^{\max} = 1.18$ for the 32 mm-diameter ring. Maximum principal stretches increase with decreasing rings size, while the overall stretch pattern remain invariant to the degree of downsizing.

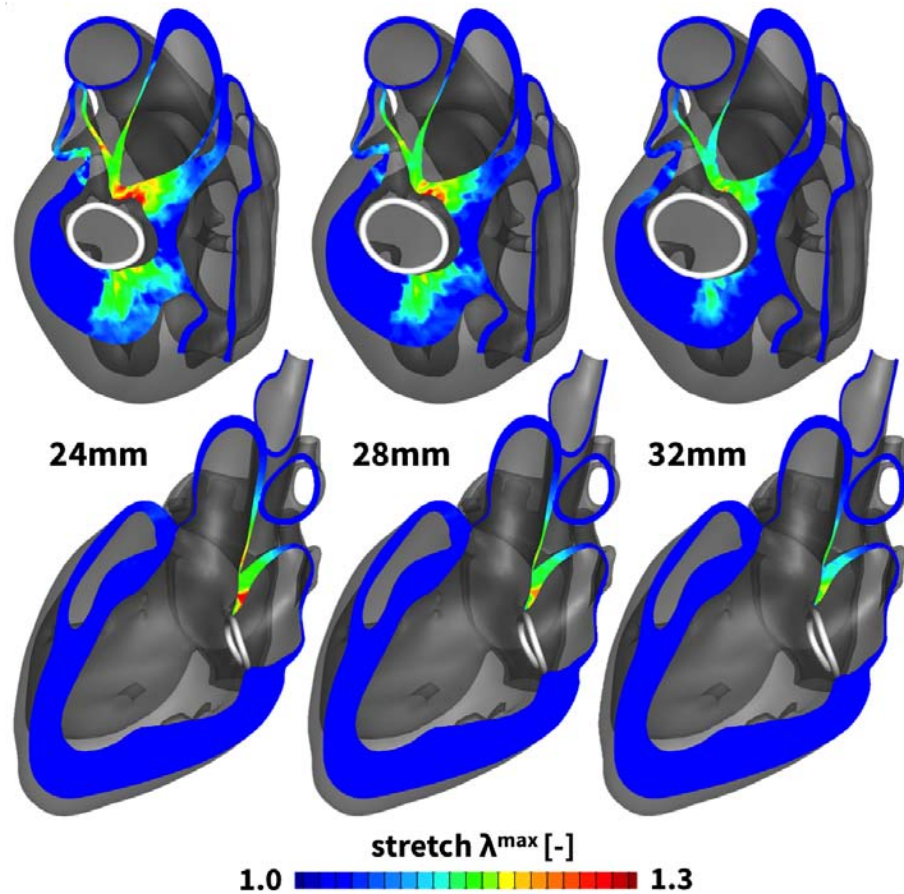


Figure 6.6: Two chamber and four chamber views of the heart after virtual ring implantation

Annular Effects.

Figure 6.7 highlights the effects of mitral annuloplasty on mitral dimensions. Figure 6.7, left, displays the initial healthy annulus and the dilated annulus in response to ventricular remodeling. Figure 6.7, right, depicts the stretch introduced through annuloplasty with rings of 24, 28, and 32 mm diameter. For all three cases, compressive stretches of $\lambda < 1.0$ indicate a reduction in annular dimensions in response to surgical downsizing. Downsizing is largest in the septal and postero-lateral regions and smallest in the anterior and posterior regions. The magnitude of compressive stretch is inversely proportional to the ring size; the 24 mm ring introduces the largest compressive stretch and the 32 mm ring the smallest. Specifically, mean compressive stretches were 0.75, 0.85, and 0.92 for the 24, 28, and 32 mm rings. Interestingly, peak compressive stretches were rather invariant to ring size with 0.51, 0.46, and 0.54, respectively. Notably, the saddle-height, a measure for the out-of-plane topology of the mitral annulus, is markedly reduced with all three rings.

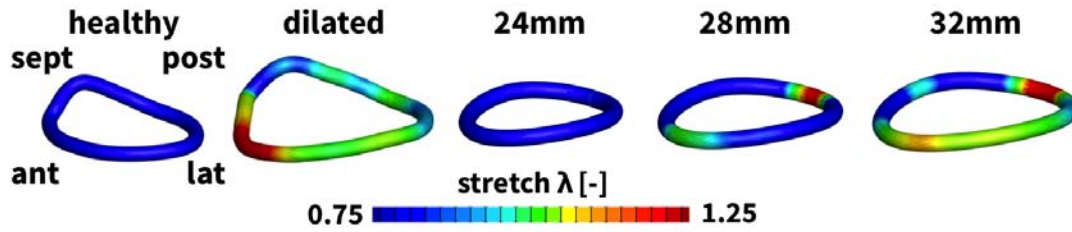


Figure 6.7: Annular stretch in the healthy and dilated annulus, and after ring-implantation

Table 6.2: Annular dimensions with 24 mm, 28 mm, and 32 mm diameter Physio rings implanted

ring size [mm]	mitral annular area [mm ²]	mitral annular perimeter [mm]	septal-lateral distance [mm]	comm-comm distance [mm]
24	480.20	81.94	23.49	27.86
28	612.76	92.77	26.66	30.90
32	772.05	104.06	29.87	35.17

Table 6.2 summarizes the mitral annular area, mitral annular perimeter, septal-lateral distance, and commissure-commissure distance after the implantation of the three rings. As expected, the three rings significantly reduce all four metrics. The most significant size reduction results from implanting the 24 mm diameter ring, which essentially re-establishes the ungrown mitral valve dimensions with septal-lateral and commissure-commissure distances of 27.86 mm and 23.49 mm in comparison to the healthy baseline state with 27.47 mm and 23.72 mm.

Suture Forces.

Table 6.3 summarizes the suture forces upon ring implantation. In agreement with the stretch distributions in Figure 6.7, suture forces increase with the degree of downsizing. The total force to implant the 24 mm diameter ring is 2.2 N; for the 28 mm and 32 mm diameter rings, the total force decreases to 1.9 N and 0.8 N, respectively. The individual suture forces are distributed heterogeneously around the perimeter of the annuloplasty ring. Generally, suture forces are highest in the antero-septal region, on sutures #12 and #13, and in the postero-lateral region, on sutures #5 and #6, which coincide with the regions of largest myocardial strains in Figure 6.6 and largest annular downsizing in Figure 6.7.

6.4 Discussion

The objective of this manuscript was to explore the Living Heart model as a virtual surgical tool for the optimal design, selection, and sizing of cardiovascular devices. Here we have focused specifically on characterizing and quantifying the effects of undersized annuloplasty in the context of dilated

Table 6.3: Suture forces upon ring implantation

size [mm]	#1 [mN]	#2 [mN]	#3 [mN]	#4 [mN]	#5 [mN]	#6 [mN]	#7 [mN]
24	119.0	142.8	42.7	39.8	163.5	235.2	111.3
28	70.8	94.7	92.0	119.7	65.5	134.5	65.9
32	51.5	66.7	32.7	34.6	7.6	61.3	29.5
size [mm]	#8 [mN]	#9 [mN]	#10 [mN]	#11 [mN]	#12 [mN]	#13 [mN]	#14 [mN]
24	166.6	179.1	161.0	71.2	275.6	349.8	182.6
28	96.4	144.7	122.9	244.0	217.8	260.6	116.4
32	36.5	29.8	16.3	53.0	143.5	151.1	53.6

cardiomyopathy.

6.4.1 Dilated Cardiomyopathy

To create a model of dilated cardiomyopathy, we used the Living Heart model in combination with the theory of finite growth [71]. Specifically, we focused on the effects of overstretch-induced growth on ventricular remodeling and mitral annular dilation. Understanding remodeling-induced alterations in mitral valve geometry is critical to tailor mitral valve repair to a specific remodeling pattern [159]. Our simulations in Figure 6.4 predict a significant dilation of the left ventricle, particularly in the anterior and septal regions of the mitral annulus. In addition to annular stretch as a mechanical measure of annular deformation in Figure 6.5, we quantify standard clinical metrics of annular dimension in Table 6.1. Both mechanical and clinical data are in good agreement with literature reports: Our model predicts an increase of mitral annular area by a factor of 1.7 and an increase in septal-lateral distance of 1.3, values, which are in agreement with three-dimensional ultrasound measurements in patients with dilated cardiomyopathy [122]. Our model also predicts a marked circularization of the mitral annulus with a healthy and diseased ellipticity of 1.16 and 0.99, characteristic of patients with dilated cardiomyopathy [122]. Both mechanical and clinical changes observed during ventricular growth are also in good agreement with experimental measurements in an ovine model of ischemic dilated cardiomyopathy [178].

6.4.2 Mitral Annuloplasty

To explore the effects of device selection on the myocardial tissue surrounding the mitral valve, we virtually implanted three annuloplasty rings into the dilated Living Heart model and quantified myocardial strains and mitral annular downsizing using both mechanical and clinical metrics. Our

results suggest that more severe downsizing, as quantified in Table 6.2, introduces larger tissue deformation both in the myocardium and the mitral annulus itself. Surgically-induced deformations in the ventricular myocardium in Figure 6.6 and in the mitral annulus in Figure 6.7 are co-localized. While these observations agree with our common intuition, our simulations also predict the regional variation of surgically-induced deformations with peak values in the septal and postero-lateral regions of the myocardium and the mitral annulus.

Regional variations in myocardial strain, stretch, and stress are virtually impossible to quantify in the beating heart, but critically important to optimize surgical procedures and device design. For example, our model predicts large stretches in response to undersized annuloplasty in the postero-lateral region of the mitral valve. This region is also largely affected in patients with ischemic cardiomyopathy following infarction of the posterior wall. Disease-specific rings have been developed for this patient population to minimize stress on the posterior wall segment by use of a postero-lateral dip [54]. In addition, the Edwards IMR ETLogix ring provides an increased sewing margin to accommodate double row sutures that may prevent potential ring dehiscence in this particular pathology. In the present case, the Edwards IMR ETLogix ring would have provided an advantage over the standard Physio ring. While our findings may, in part, be specific to the particular anatomy of the Living Heart model, they generally highlight the potential of a virtual surgical test environment for optimizing ring selection.

The junction between the mitral and aortic valves is another region of elevated annular strain as predicted by our simulation. From a structural point of view, this region is thin and non-muscular and provides little resistance to the laterally oriented suture forces. Our results suggest that, because of the proximity of the mitral valve to the aortic valve complex, undersized annuloplasty may indirectly affect the performance of an otherwise fully functional aortic valve [57]. A decreased proximity between the mitral and aortic valves, as seen in patients with hypertrophic cardiomyopathy, may further increase the risk of systolic anterior motion of the anterior mitral valve leaflet [126]. Predictive simulations of surgical procedures provide informed criteria to balance the benefits of undersized annuloplasty and the increased risk of disrupting cardiac physiology.

6.4.3 Suture Forces

Without doubt, the Living Heart model ranks among the most detailed human heart simulators to date. Such complexity, however, comes at the cost of many potential sources of uncertainty. So far, we have discussed primarily strains that can be validated using invasive and non-invasive imaging modalities including implanted marker techniques in animals [7, 80, 175, 209] and tissue doppler imaging in patients [169]. In addition to strains, we also report suture forces. Mechanical loading along the suture lines has been closely associated with repair durability [158]. In Abaqus/Standard, one-dimensional connector elements allow us to gradually decrease the distance between selected points to simulate sutures and postprocess the required suture forces [2]. These forces are strongly

dependent on the material model and its associated parameters [129, 179]. Our results from Table 6.3 are in good agreement with in vivo measurements of suture forces during annular downsizing in a porcine model [96, 97]. Our simulations predict a total force of 2.2 N, which agrees well with the reported total suture force for maximum downsizing of 3.5 N [97].

The quantification of suture forces is not only interesting from a validation point of view, it is also of practical importance to the cardiac surgeon. Suture bites represent focal stress points both in the fabric of the annuloplasty ring and in the myocardial tissue. High suture forces indicate risk of tissue damage and ring dehiscence [111]. Our simulations not only provide insight into the long-term failure of undersized annuloplasty by predicting regions of continued ventricular remodeling, but also help prevent short-term failure by identifying potential sites of ring dehiscence.

6.4.4 Conclusion

We have, for the first time, used a human heart simulator to model the surgical procedure of mitral valve repair. Our simulations utilize the Living Heart model, a highly accurate, anatomic representation of a healthy adult human heart with all four chambers and valves. Starting with a healthy heart, we simulated the progression of dilated cardiomyopathy, its impact on the mitral valve complex, and its repair using annuloplasty rings. While it is virtually impossible to characterize the entire mechanical environment of the mitral valve complex in vivo, our simulations allow us to precisely quantify tissue strains, annular stretch, mitral valve kinematics, and suture forces and identify local regions of maximum stretch or force. Taken together, our simulations suggest that during undersized valvular annuloplasty, the highest suture forces co-localize with regional peaks in myocardial strain and annular stretch. Our model predicts the highest risk of dehiscence in the septal and postero-lateral regions. In agreement with our intuition, our simulations demonstrate that a more drastic downsizing results in higher suture forces. However, our simulations precisely quantify the individual suture forces and show that in our case, implanting a 24 mm ring requires three times larger forces than implanting the same ring with 32 mm diameter. Realistic predictive simulations of surgical intervention have the potential to optimize surgical procedures, improve device design, and guide treatment planning on an individual, personalized basis.

Acknowledgements

The authors acknowledge the stimulating discussions with Jay D. Humphrey at Yale University and the technical support from Roger Clarke at Zygote Media Group. This work was supported by the 5T32HL007974-14 grant (M.K. Rausch), the Stanford Graduate Fellowship (A.M. Zöllner), the Marie-Curie international outgoing fellowship (M. Genet), the NSF grant 1233054 and NIH grant U01-HL119578 (E. Kuhl).

Conclusions

In the scope of this thesis, I have successfully created and run patient specific simulations of adaptive tissue. I have successfully derived and calibrated constitutive models for adaptive tissue. To put our constitutive framework to practice in realistic scenarios I have created patient specific geometry models from medical imaging data. Our tool of choice to solve the created system of partial differential equations was the finite element method. The main advantage of the finite element method over analytical models is its natural ability to capture geometries that are difficult or impossible to describe using analytical models, but can be subdivided into smaller, finite elements. In particular, accurate patient specific models are virtually impossible to realize using analytical models. The same holds for the modeling of physical contact between one or more bodies. Again, the finite element method can be applied using small or finite sliding contact models to create realistic simulations of the interaction. However, all these features and the flexibility compared to analytical mathematical models do not come free. Compared to their analytical counterparts, finite element models are typically computationally expensive and cumbersome to create. Therefore, in addition to the concluding remarks, the opportunities and obstacles of using the finite element method to model adaptive tissues and their interaction with devices and changing boundary conditions are presented in the following.

Skin Expansion

I have presented a novel computational model for growing biological membranes in which I have summarized the underlying mechanobiology in a single phenomenological internal variable, the in-plane area growth. To demonstrate the model performance, I have simulated tissue expansion in pediatric forehead reconstruction. Driven by the clinical interest for a mechanistic model for skin expansion, I have continuously improved our model. Without altering the key equations for skin growth, I have transformed the model into a more efficient spatial formulation and implemented it into the general purpose finite code ABAQUS/Standard. This allowed for more realistic simulations of the expander device itself and its interaction with the skin. The resulting model in its latest version is applicable to arbitrary skin geometries derived from medical imaging and can use a discrete volume

controlled expander with sliding contact under the skin. I can now control the amount of overstretch by the step-wise inflation of a virtually implanted tissue expander. This allows us to predict the rheological effect of stress relaxation. Upon acute inflation, the chronic increase in skin area at constant stretch, associated with a chronic decrease in elastic stress, stretch and pressure can be observed. All these measures are clinically relevant since they control capillary refill, adaptation speed, tissue necrosis, scarring, and patient discomfort, but are virtually impossible to measure in situ with the exception of the expander pressure. Therefore, the finite element method provides an extraordinary tool to support surgical planning and expander development in the future. While the modeling effort is significant, I expect the simulation based approach to become more and more relevant in the future, particularly in the domain of customized 3D printed tissue expanders.

Skeletal Muscle Adaption

The creation of serial sarcomere units (sarcomerogenesis) and their removal (contracture) have been demonstrated and quantified in chronic animal studies through the over- and under-stretching of skeletal muscle. I have created a novel computational model for skeletal muscle sarcomerogenesis and contracture. When calibrated using experimental data, the sarcomerogenesis model is able to predict the lengthening of an extensor digitorum lateralis muscle with a model error smaller than the standard deviation of the data. Similar results were achieved for the contracture model, with a slightly larger error. The model can be applied to arbitrary muscle geometries and the local fiber orientation can be set as a material property on the element level. I have demonstrated the model features simulating sarcomerogenesis after tendon transfer surgery and contracture following the extended wearing of high heeled footwear. For both scenarios it was observed that the magnitudes of local adaptation far exceed what would be predicted from the organ level stretch. While these results explain phenomena reported in the medical literature, patient specific modeling of skeletal muscle growth has limited clinical applications and relevance. Most functionally relevant phenomena, such as the stress and stretch differences observed in single step compared to multi-step procedures, are well captured by the central one-dimensional growth equation. Seeing the high imaging and modeling effort, the creation of patient specific 3D finite element models may only be justified under special circumstances.

Cardiovascular Applications

I have used a four chamber human heart simulator to model mitral valve annuloplasty surgery. Using a healthy human heart as a baseline geometry, I simulated left ventricular growth and mitral annular dilation. Based on the resulting, diseased geometry I then simulated the surgical downsizing of the mitral annulus using an annuloplasty ring. To study the effect of the ring size on the mitral valve

kinematics I virtually implanted 3D reconstructed Carpentier Edwards Physio II rings with three different diameters. To quantify the surgery outcome, I then virtually measured the septal-lateral and commissure-commissure distances, the strain in the surrounding tissue, and the suture forces. In agreement with findings reported in the medical literature, the smallest ring size provided the best reconstruction of the original mitral valve geometry, but also caused the highest suture forces and strains in the surrounding tissue. As expected, increasing the ring size reduced the invasiveness of the procedure, but resulted in larger annular areas and a less effective reconstruction overall. While the measurement of most of these values in vivo is virtually impossible for just one ring, there is no way to implant and compare multiple options at all. Finite element simulations provide a way to virtually test different ring sizes and shapes and quantify their effect before surgery. Performing virtual annuloplasty surgery can help the surgeon to pick a ring size and type that effectively reconstructs the annular geometry while optimizing for low suture forces and tissue strains. In addition to applications in surgical planning, finite element simulations can help to guide the development of new implants or create better sizing guidelines.

Concluding Remarks

Patient specific finite element simulation is a promising tool in biomedical research, surgical planning, and medical device development. However, as I have discussed previously in this chapter, applications should be selected carefully due to the computational and modeling resources needed. In summary, it can be stated that finite element simulations of adaptive tissue are well suited for applications in plastic surgery as for example skin expansion procedures. The superficial position of the skin and its primarily two-dimensional nature allow for fast and efficient geometry modeling. In addition, access to measure mechanical parameters is easily available and the measurement procedures are typically non-invasive. In contrast, applications for simulations of skeletal muscle adaptation show limited benefits compared to the extensive modeling effort. While the geometry modeling requires expensive image acquisition using CT or MRI scanning, the addition of clinically useful information from these 3D simulations is minimal compared to one-dimensional models. Lastly, the finite element method is an excellent tool for cardiovascular surgery planning. Procedures such as mitral valve repair surgery are performed on high risk, high cost patient populations with major comorbidities and comortalities. The benefits of tools like the virtual ring sizing tool presented in this thesis promise to far outweigh their additional cost. Overall, after careful cost benefit analyses, finite element models of adapting soft tissue are a promising tool for applications in surgery planning and fast paced medical device R&D environments. I envision current trends in medicine like customized 3D printed implants to accelerate the development and adaptation of these models in the future.

Bibliography

- [1] Abaqus 6.12. *Analysis User's Manual*. SIMULIA. Dassault Systèmes. 2012.
- [2] Abaqus 6.13. *Analysis User's Manual*. 2013. Simulia. Dassault Systèmes.
- [3] Agache PG, Monneur C, Leveque JL, DeRigal J. Mechanical properties and Young's modulus of human skin in vivo. *Arch Dermatol Res*. 1980;269:221-232.
- [4] Ambrosi D, Mollica F. On the mechanics of a growing tumor. *Int J Eng Sci*. 2002;40:1297-1316.
- [5] Ambrosi D, Preziosi L, Vitale G. The insight of mixtures theory for growth and remodeling. *ZAMP*. 2010;61:177-191.
- [6] Ambrosi D, Ateshian GA, Arruda EM, Cowin SC, Dumais J, Goriely A, Holzapfel GA, Humphrey JD, Kemkemer R, Kuhl E, Olberding JE, Taber LA, Garikipati K. Perspectives on biological growth and remodeling. *J Mech Phys Solids*. 2011;59:863-883.
- [7] Amini, R., Eckert, C.E., Koomalsingh, K., McGarvey, J., Minakawa, M., Gorman, J.H., Gorman, R.C., Sacks, M.S. On the in vivo deformation of the mitral valve anterior leaflet: Effects of annular geometry and referential configuration. *Annals of Biomedical Engineering* 2012;40:1455-1467.
- [8] American Podiatric Medical Association. 2003. High Heels Survey.
- [9] Argenta LC, Watanabe MJ, Grabb WC. The use of tissue expansion in head and neck reconstruction. *Annals Plast Surg*. 1983;11:31-37.
- [10] Arneja JS, Gosain AK. Giant congenital melanocytic nevi of the trunk and an algorithm for treatment. *J Craniofac Surg*. 2005;16:886-893.
- [11] Arneja JS, Gosain AK. Giant congenital melanocytic nevi. *Plast Reconstr Surg*. 2007;120:26e-40e.
- [12] Arnold AS, Liu MQ, Schwartz MH, Ounpuu S, Delp SL. The role of estimating muscle-tendon lengths and velocities of the hamstrings in the evaluation and treatment of crouch gait. *Gait Posture*. 2006;23:273-281.

- [13] Arnold EM, Delp SL. Fibre operating lengths of human lower limb muscles during walking. *Phil Trans R Soc London B Biol Sci.* 2011;366:1530-1539.
- [14] Astanin S, Preziosi L. Mathematical modelling of the Warburg effect in tumour cords. *J Theor Bio.* 2009;258:578-590.
- [15] Austad ED, Pasyk KA, McClatchey KD, Cheery GW. Histomorphologic evaluation of guinea pig skin and soft tissue after controlled tissue expansion. *Plast Reconstr Surg.* 1982;70:704-710.
- [16] Austad ED, Thomas SB, Pasyk KA. Tissue expansion: Divided or loan? *Plast Reconstr Surg.* 1982;78:63-67.
- [17] Baillargeon, B., Rebelo, N., Fox, D.D., Taylor, R.L., Kuhl, E., 2014. The Living Heart Project: A robust and integrative simulator for human heart function. *European Journal of Mechanics A/Solids*, 48, 38-47.
- [18] Baillargeon, B., Costa, I., Leach, J.R., Lee, L.C., Genet, M., Toutain, A., Wenk, J.F., Rausch, M.K., Rebelo, N., Acevedo-Bolton, G., Kuhl, E., Navia, J.L., Guccione, J.M., 2015. Human cardiac function simulator for the optimal design of a novel annuloplasty ring with a sub-valvular element for correction of ischemic mitral regurgitation. *Cardiovascular Engineering and Technology* 6(2), 105-116.
- [19] Baker SR. Fundamentals of expanded tissue. *Head & Neck.* 1991;13:327-333.
- [20] Barnett JG, Holly RG, Ashmore CR. Stretch-induced growth in chicken wing muscles: biochemical and morphological characterization. *Am J Physiol.* 1980;239:C39-C46.
- [21] Barone FE, Perry L, Keller T, Maxwell GP. The biomechanical and histopathologic effect of surface texturing with silicone and polyurethane in tissue implantation and expansion. *Plast Reconstr Surg.* 1992;90:77-86.
- [22] Beauchenne JG, Chambers MM, Peterson AE, Scott PG. Biochemical, biomechanical, and physical changes in the skin in an experimental animal model of therapeutic tissue expansion. *J Surg Res.* 1989;47:507-514.
- [23] Bernardini F, Mittleman J, Rushmeier H, Silva C, Taubin G. The ball-pivoting algorithm for surface reconstruction. *IEEE Trans Vis Comp Graph.* 1999;5:349-359.
- [24] Böl M, Reese S, Parker KK, Kuhl E. Computational modeling of muscular thin films for cardiac repair. *Comp Mech.* 2009;43:535-544.
- [25] Blemker SS, Asakawa DS, Gold GE, Delp SL. 2007. Image-based musculoskeletal modeling: Applications, advances, and future opportunities. *J Magn Res Img.* 25:441-451.

- [26] Böl M, Reese S. 2008. Micromechanical modelling of skeletal muscles based on the finite element method. *Comp Meth Biom Biomed Eng.* 11:489–504.
- [27] Böl M, Sturmat M, Weichert C, Kober C. A new approach for the validation of skeletal muscle modeling using MRI data. *Comp Mech.* 2011;47:591-601.
- [28] Böl M, Stark H, Schilling N. 2011. On a phenomenological model for fatigue effects in skeletal muscles. *J Theor Bio.* 281:122–132.
- [29] Böl M, Abilez OJ, Assar AN, Zarins CK, Kuhl E. In vitro / in silico characterization of active and passive stresses in cardiac muscle. *Int J Multiscale Comp Eng.* 2012;10:171-188.
- [30] Bothe, W., Kuhl, E., Kvitting, J.P., Rausch, M.K., Göktepe, S., Swanson, J.C., Farahmandnia, S., Ingels, N.B., Miller, D.C., 2011. Rigid, complete annuloplasty rings increase anterior mitral leaflet strains in the normal beating ovine heart. *Circulation* 124, S81-S96.
- [31] Bothe, W., Rausch, M.K., Kvitting, J.P., Echtner, D.K., Walther, M., Ingels, N.B., Kuhl, E., Miller, D.C. 2012. How do annuloplasty rings affect mitral annular strains in the normal beating ovine heart? *Circulation*, 126, S231-S238.
- [32] Bothe, W., Miller, D.C., Doenst, T., 2013. Sizing for mitral annuloplasty: where does science stop and voodoo begin?, *The Annals of Thoracic Surgery* 95(4), 1475-1483.
- [33] Bottinelli R, Reggiani C. Skeletal muscle plasticity in health and disease. *Advances in Muscle Research.* 2002; Volume 2, Springer.
- [34] Brobmann GF, Huber J. Effects of different shaped tissue expanders on transluminal pressure, oxygen tension, histopathologic changes, and skin expansion in pigs. *Plast Reconstr Surg.* 1985;76:731-736.
- [35] Brockes, JP Amphibian limb regeneration: Rebuilding a complex structure. *Science.* 1997;276:81-87
- [36] Buganza Tepole A, Ploch CJ, Wong J, Gosain AK, Kuhl E. Growing skin - A computational model for skin expansion in reconstructive surgery. *J Mech Phys Solids.* 2011;59:2177-2190.
- [37] Buganza Tepole A, Gosain AK, Kuhl E. Stretching skin: The physiological limit and beyond. *Int J Nonlin Mech.* doi: 10.1016/j.ijnonlinmec.2011.07.006.
- [38] Buganza Tepole A, Gosain AK, Kuhl E. Stretching skin: The physiological limit and beyond. *Int J Nonlin Mech.* 2012;47:938-949.
- [39] Buganza Tepole A, Kuhl E. Systems-based approaches towards wound healing. *Pediatric Res.* 2013;doi:10.1038/pr.2013.3.

- [40] Burkholder TJ, Lieber RL. Sarcomere number adaptation after retinaculum transection in adult mice. *J Exp Bio.* 1998;201:309-316.
- [41] Burkholder TJ. Mechanotransduction in skeletal muscle. *Front Biosci.* 2007;12:174-191.
- [42] Caiozzo VJ, Utkan A, Chou R, Khalafi A, Chandra H, Baker M, Rourke B, Adams G, Baldwin K, Green S. Effects of distraction on muscle length: Mechanisms involved in sarcomerogenesis. *Clin Orthop Rel Res.* 2002;403S:S133-S145.
- [43] Calvo B, Ramirez A, Alonso A, Grasa J, Soteras F, Osta R, Munoz MJ. Passive nonlinear elastic behavior of skeletal muscle: Experimental results and model formulation *J Biomech.* 2010;43:133-145.
- [44] Carpentier, A.F., Lessana, A., Relland, J.Y., Belli, E., Mihaileanu, S., Berrebi, A.J., Palsky, E., Loulmet, D.F., 1995. The “Physio-Ring”: an advanced concept in mitral valve annuloplasty. *Annals of Thoracic Surgery* 60, 1177-1186.
- [45] Castilla EE, da Graca Dutra M, Orioli-Parreiras IM. Epidemiology of congenital pigmented naevi: I. Incidence rates and relative frequencies. *Br J Dermatol.* 1981;104:307-315.
- [46] Chanaud CM, Pratt CA, Loeb GE. 1991. Functionally complex muscles of the cat hindlimb. II. Mechanical and architectural heterogeneity within the biceps femoris. *Exp Brain Res.* 85:257-270.
- [47] Ciarletta P., Ben Amar M. Papillary networks in the dermal-epidermal junction of skin: a biomechanical model. *Mech Res Comm.* in press.
- [48] Ciarletta P, Ambrosi D, Maugin GA. Mass transport in morphogenetic processes: A second gradient theory for volumetric growth and material remodeling. *J Mech Phys Solids.* 2012;60:432-450.
- [49] Cox B. A multi-scale, discrete-cell simulation of organogenesis: Application to the effects of strain stimulus on collective cell behavior during ameloblast migration. *J Theor Bio.* 2010;262:58-72.
- [50] Cromie MJ, Sanchez GN, Schnitzer MJ, Delp SL. 2013. Sarcomere lengths in human extensor carpi radialis brevis measured by microendoscopy. *Muscle & Nerve* 48:286-292.
- [51] Csapo R, Maganaris CN, Seynnes OR, Narici MV. 2010. On muscle, tendon and high heels. *J Exp Bio.* 213:2582–2588.
- [52] Cronin NJ, Barrett RS, Carty CP. 2012. Long-term use of high-heeled shoes alters the neuromechanics of human walking. *J Appl Physiol.* 112:1054–1058.
- [53] Cronin NJ. 2014. The effects of high heeled shoes on female gait: A review. *J Electr Kinesiol.* 24:258–263.

- [54] Daimon, M., Fukuda, S., Adams, D.H., McCarthy, P.M., Gillinov, A.M., Carpentier, A., Filsoufi, F., Abascal, V.M., Rigolin, V.H., Salzberg, S., Huskin, A., Langenfeld, M., Shiota, T., 2006. Mitral valve repair with Carpentier-McCarthy-Adams IMR ETlogix annuloplasty ring for ischemic mitral regurgitation. Early echocardiographic results from a multi-center study. *Circulation* 114(1 suppl), I588-I593.
- [55] De Filippo RE, Atala A. Stretch and growth: the molecular and physiologic influences of tissue expansion. *Plast Reconstr Surg.* 2002;109:2450-2462.
- [56] Dervaux J, Ciarletta P, Ben Amar M. Morphogenesis of thin hyperelastic plates: A constitutive theory of biological growth in the Föppl-von Karman limit. *J Mech Phys Solids.* 2009;57:458-471.
- [57] Ducharme, A., Courval, J.F., Dore, A., Leclerc, Y., Tardif, J.C., 1999. Severe aortic regurgitation immediately after mitral valve annuloplasty. *Annals of Thoracic Surgery* 67(5), 1487-1489.
- [58] Duits EHA, Molenaar J, van Rappard JHA. The modeling of skin expanders. *Plast Reconstr Surg.* 1989;83:362-367.
- [59] Dupont Salter AC, Richmond FJR, Loeb GE. 2011. Effects of muscle immobilization at different lengths on tetrodotoxin-induced disuse atrophy. *IEEE Trans Neur Sys Reha Eng.* 11:209-217.
- [60] Ebbeling CJ, Hamill J, Crusemeyer JA. 1994. Lower extremity mechanics and energy cost of walking in high-heeled shoes. *J Orth Sports Phys Therapy.* 19:190-196.
- [61] Ehler E, Gautel M. The sarcomere and sarcomerogenesis. In: *The Sarcomere and Skeletal Muscle Disease.* edited by Laing NG. 2008. Springer.
- [62] Epstein M, Maugin GA. Thermomechanics of volumetric growth in uniform bodies. *Int J Plast.* 2000;16:951-978.
- [63] Eurviriyankul S, Askes H. 2011. Tendon layout optimization through configurational force equilibration in plane stress analysis of prestressed concrete structures. *Comp Struct.* 89:1673-1680.
- [64] Fabri A, Pion S. 2009. CGAL: the Computational Geometry Algorithms Library. In: *17th ACM SIGSPATIAL Int Conf.* pp. 538-539. ACM Press, New York, New York, USA.
- [65] Francis AJ, Marks R. Skin stretching and epidermopoiesis. *Br J Exp Pathol.* 1977;58:35-39.
- [66] Fuster, V., Gersh, B.J., Giuliani, E.R., Tajik, A.J., Brandenburg, R.O., Frye, R.L., 1981. The natural history of idiopathic dilated cardiomyopathy. *American Journal of Cardiology* 47(3), 525-531.

- [67] Garikipati K. The kinematics of biological growth. *Appl Mech Rev.* 2009;62:030801.1-030801.7.
- [68] Genet, M., Lee, L.C., Nguyen, R., Haraldsson, H., Acevedo-Bolton, G., Zhang, Z., Ge, L., Ordovas, K., Kozerke, S., Guccione, J.M., 2014. Distribution of normal human left ventricular myofiber stress at end-diastole and end-systole - A target for in silico studies of cardiac procedures. *Journal of Applied Physiology* 117, 142-152.
- [69] Genet, M., Lee, L.C., Baillargeon, B., Guccione, J.M., Kuhl, E., 2015. Modeling pathologies of systolic and diastolic heart failure. *Annals of Biomedical Engineering* doi: 10.1007/s10439-015-1351-2.
- [70] Gerber C, Meyer DC, Frey E, von Rechenberg B, Hoppeler H, Frigg R, Jost B, Zumstein MA. Reversion of structural muscle changes caused by chronic rotator cuff tears using continuous muscolotendinous traction. *J Shoulder Elbow Surg.* 2009;18:163-171.
- [71] Göktepe S, Abilez OJ, Parker KK, Kuhl E. A multiscale model for eccentric and concentric cardiac growth through sarcomerogenesis. *J Theor Bio.* 2010;265:433-442.
- [72] Göktepe S, Abilez OJ, Kuhl E. A generic approach towards finite growth with examples of athlete's heart, cardiac dilation, and cardiac wall thickening. *J Mech Phys Solids.* 2010;58:1661-1680.
- [73] Göktepe S, Abilez OJ, Parker KK, Kuhl E. 2010. A multiscale model for eccentric and concentric cardiac growth through sarcomerogenesis. *J Theor Bio.* 265:433-442.
- [74] Göktepe S, Menzel A, Kuhl E. 2014. The generalized Hill model: A kinematic approach towards active muscle contraction. *J Mech Phys Solids.* 72:20-39.
- [75] Goldspink G. Sarcomere length during post-natal growth of mammalian muscle fibers. *J Cell Sci.* 1968;3:539-548.
- [76] Gordon AM, Huxley AF, Julian FJ. The variation in isometric tension with sarcomere length in vertebrate muscle fibers. *J Physiol.* 1966;184:170-192.
- [77] Goriely A, BenAmar M. Differential growth and instability in elastic shells. *Phys Rev Letters.* 2005;94:198103.
- [78] Goriely A, Tabor M. Biomechanical models of hyphal growth in actinomycetes. *J Theor Bio.* 2003;222:211218.
- [79] Goriely A, BenAmar M. On the definition and modeling of incremental, cumulative, and continuous growth laws in morphoelasticity. *Biomech Model Mechanobio.* 2007;6:289296.

- [80] Gorman III, J.H., Gupta, K.B., Streicher, J.T., Gorman, R.C., Jackson, B.M., Ratcliffe, M.B., Bogen, D.K., Edmunds, L.H., 1996. Dynamic three-dimensional imaging of the mitral valve and left ventricle by rapid sonomicrometry array localization. *Journal of Thoracic and Cardiovascular Surgery* 112, 712-726.
- [81] Gosain AK, Santoro TD, Larson DL, Gingrass RP. Giant congenital nevi: A 20-year experience and an algorithm for their management. *Plast Reconstr Surg.* 2001;108:622-636.
- [82] Gosain AK, Cortes W. Pediatric tissue expansion for forehead reconstruction: A 13-year review and an algorithm for its use. *Am Soc Plast Surg.* Baltimore, 2007; Abstract 13288.
- [83] Gosain AK, Zochowski CG, Cortes W. Refinements of tissue expansion for pediatric forehead reconstruction: A 13-year experience. *Plast Reconstr Surg.* 2009;124:1559-1570.
- [84] Guccione, J.M., McCulloch, A.D., Waldman, L.K., 1991. Passive material properties of intact ventricular myocardium determined from a cylindrical model. *Journal of Biomechanical Engineering* 113, 42-55.
- [85] Hayatsu K, De Deyne PG. Muscle adaptation during distraction osteogenesis in skeletally immature and mature rabbits. *J Orth Res.* 2001;19:897-905.
- [86] Herring SW, Grimm AF, Grimm BR. Regulation of sarcomere number in skeletal muscle: A comparison of hypotheses. *Muscle & Nerve.* 1984;7:161-173.
- [87] Himpel G, Kuhl E, Menzel A, Steinmann P. Computational modeling of isotropic multiplicative growth. *Comp Mod Eng Sci.* 2005;8:119-134.
- [88] Himpel G, Menzel A, Kuhl E, Steinmann P. Time-dependent fiber reorientation of transversely isotropic continua - Finite element formulation and consistent linearization. *Int J Num Meth Eng.* 2008;73:1413-1433.
- [89] Hollenstein M, Ehret AE, Itskov M, Mazza E. A novel experimental procedure based on pure shear testing of dermatome-cut samples applied to porcine skin. *Biomech Model Mechanobio.* 2011;10:651-661.
- [90] Holzapfel, GA, 2000. *Nonlinear Solid Mechanics: A Continuum Approach for Engineering.* John Wiley & Sons.
- [91] Humphrey J. *Cardiovascular tissue mechanics: Cells, tissues, and organs.* Springer. 2002.
- [92] Humphrey, J.D., Holzapfel, G.A., 2012. Mechanics, mechanobiology, and modeling of human abdominal aorta and aneurysms. *Journal of Biomechanics* 45(5), 805-814.
- [93] Huxley H, Hanson J. Changes in the cross-striations of muscle during contraction and stretch and their structural interpretation. *Nature.* 1994;173:973-976.

- [94] Jaalouk DE, Lammerding J. Mechanotransduction gone awry. *Nature Rev Mol Cell Bio.* 2009;10:63-73.
- [95] Javili A, Steinmann P. On the thermodynamics of solids with boundary structures. *Int J Solids & Structures.* 2010;47:3245-3253.
- [96] Jensen, M.O., Jensen, H., Nielsen, S.L., Smerup, M., Johansen, P., Yoganathan, A.P., Nygaard, H., Hasenkam, J.M. 2008. What forces act on a flat rigid mitral annuloplasty ring? *Journal of Heart Valve Disease* 17(3), 267-275.
- [97] Jensen, M.O., Honge, J.L., Benediktsson, J.A., Siefert, A.W., Jensen, H., Yoganathan, A.P., Snow, T.K., Hasenkam, J.M. Nygaard, H., Nielsen, S.L., 2014 Mitral valve annular downsizing forces: Implications for annuloplasty device development. *Journal of Thoracic and Cardiovascular Surgery* 148(1), 83-89.
- [98] Johnson TM, Lowe L, Brown MD, Sullivan MJ, Nelson BR. Histology and physiology of tissue expansion. *J Dermatol Surg Oncol.* 1993;19:1074-1078.
- [99] Jor JWY, Nash MP, Nielsen PMF, Hunter PJ. Estimating material parameters of a structurally based constitutive relation for skin mechanics. *Biomech Model Mechanobio.* 2011;10:767-778.
- [100] Kaplan EN. The risk of malignancy in large congenital nevi. *Plast Reconstr Surg.* 1974;53:421-428.
- [101] Kerckhoffs RCP, Omens JH, McCulloch AD. A single strain-based growth law predicts concentric and eccentric cardiac growth during pressure and volume overload. *Mech Res Comm.* 2012;42:40-50.
- [102] Kikuchi N, Oden JT, 1988. Contact Problems in Elasticity: A Study of Variational Inequalities and Finite Element Methods. Studies in Applied Mathematics, Society for Industrial and Applied Mathematics.
- [103] Kim Y, Lim JM, Yoon BC. 2013. Changes in ankle range of motion and muscle strength in habitual wearers of high-heeled shoes. *Foot Ankle Int.* 34:414-419.
- [104] Klepach D, Lee LC, Wenk JF, Ratcliffe MB, Zohdi TI, Navia JA, Kassab GS, Kuhl E, Guccione JM. Growth and remodeling of the left ventricle. *Mech Res Comm.* 2012;42:134-141.
- [105] Knight K. 2010. Why walking flat-footed hurts after high heels. *J Exp Bio.* 213: Insight JEB i.
- [106] Kobbelt LP, Vorsatz J, Labsik U, Seidel HP. A shrink wrapping approach to remeshing polygonal surfaces. *Comp Graph Forum.* 1999;18:119-130.

- [107] Kober C, Berg BI, Sturmat M, Rieger J, Gallo, L, Böl M, Mack M, Zeilhofer HF, Sader R. Macroscopic muscular modeling based on in vivo 4d radiology. *Int J Multiscale Comp Eng.* 2012;2:131-142.
- [108] Kono, T., Sabbah, Hani, N., Rosman, H., Alam, M., Jafri, S., Goldstein, S., 1992. Left ventricular shape is the primary determinant of functional mitral regurgitation in heart failure. *Journal of the American College of Cardiology* 20(7), 1594-1598.
- [109] Kroon M, Holzapfel GA. A model for saccular cerebral aneurysm growth by collagen fibre remodelling. *J Theor Bio.* 2007;247:775-787.
- [110] Kroon W, Delhaas T, Arts T, Bovendeerd P. Computational modeling of volumetric soft tissue growth: Application to the cardiac left ventricle. *Biomech Model Mechanobio.* 2009;8:301-309.
- [111] Kronzon, I., Sugeng, L., Perk, G., Hirsh, D., Weinert, L., Fernandez, M.A.G., Lang, R.M., 2009. Real-time 3-dimensional transesophageal echocardiography in the evaluation of post-operative mitral annuloplasty ring and prosthetic valve dehiscence. *Journal of the American College of Cardiology* 53(17), 1543-1547.
- [112] Kuhl E, Steinmann P. Mass- and volume specific views on thermodynamics for open systems. *Proc Royal Soc.* 2003;459:2547-2568.
- [113] Kuhl E, Steinmann P. On spatial and material settings of thermohyperelstodynamics for open systems. *Acta Mech.* 2003;160:179-217.
- [114] Kuhl E, Menzel A, Steinmann P. Computational modeling of growth - A critical review, a classification of concepts and two new consistent approaches. *Comp Mech.* 2003;32:71-88.
- [115] Kuhl E, Steinmann P. Computational modeling of healing - An application of the material force method. *Biomech Model Mechanobio.* 2004;2:187-203.
- [116] Kuhl E, Garikipati K, Arruda EM, Grosh K. Remodeling of biological tissue: Mechanically induced reorientation of a transversely isotropic chain network. *J Mech Phys Solids.* 2005;53:1552-1573.
- [117] Kuhl E, Menzel A, Garikipati K. On the convexity of transversely isotropic chain network models. *Phil Mag.* 2006;86:3241-3258.
- [118] Kuhl E, Maas R, Himpel G, Menzel A. Computational modeling of arterial wall growth: Attempts towards patient-specific simulations based on computer tomography. *Biomech Model Mechanobio.* 2007;6:321-331.
- [119] Kuhl E, Holzapfel GA. A continuum model for remodeling in living structures. *J Mat Sci.* 2007;2:8811-8823.

- [120] Kuhl E. 2014. Growing matter - A review of growth in living systems. *J Mech Behavior Biomed Mat.* 29:529-543.
- [121] Kvistedal YA, Nielsen PMF. Estimating material parameters of human skin in vivo. *Biomech Model Mechanobio.* 2009;8:1-8.
- [122] Kwan, J., Shiota, T., Agler, D.A., Popović, Z.B., Qin, J.X., Gillinov, M.A., Stewart, W.J., Cosgrove, D.M., McCarthy, P.M., Thomas, J.D., 2003. Geometric differences of the mitral apparatus between ischemic and dilated cardiomyopathy with significant mitral regurgitation real-time three-dimensional echocardiography study. *Circulation* 107(8), 1135-1140.
- [123] Lachmann, J., Shirani, J., Plestis, K.A., Frater, R.W.M., LeJemtel, T.H., 2001. Mitral ring annuloplasty: an incomplete correction of functional mitral regurgitation associated with left ventricular remodeling. *Current Cardiology Reports* 3(3), 241-246.
- [124] Langevin HM, Bouffard NA, Badger GJ, Iatridis JC, Howe AK. Dynamic fibroblast cytoskeletal response to subcutaneous tissue stretch ex vivo and in vivo. *Am J Physiol Cell Physiol.* 2005;288:C747C756.
- [125] Lee EH. Elastic-plastic deformation at finite strains. *J Appl Mech.* 1969;36:1-6.
- [126] Lee, K.S., Stewart, W.J., Lever, H.M., Underwood, P.L., Cosgrove, D.M., 1993. Mechanism of outflow tract obstruction causing failed mitral valve repair. Anterior displacement of leaflet coaptation. *Circulation* 88(5), II24-II29.
- [127] Lee, A.P.W., and Acker, M., Kubo, S.H., Bolling, S.F., Park, S.W., Bruce, C.J., Oh, J.K., 2009. Mechanisms of recurrent functional mitral regurgitation after mitral valve repair in non-ischemic dilated cardiomyopathy importance of distal anterior leaflet tethering. *Circulation* 119(19), 2606-2614.
- [128] Lee, C.H., Oomens, P.J., Rabbah, J.P., Yoganathan, A., Gorman, R.C., Gorman, J.H., Amini, R., Sacks, M.S., 2013. A high-fidelity and micro-anatomically accurate 3D finite element model for simulations of functional mitral valve. *Lecture Notes in Computer Science* 7945, 416424.
- [129] Lee, C.H., Amini, R., Gorman, R.C., Gorman III, J.H., Sacks, M.S., 2014. An inverse modeling approach for stress estimation in mitral valve biomaterial assessment. *Journal of Biomechanics* 47, 2055-2063.
- [130] Levi K, Kwan A, Rhines AS, Gorcea M, Moore DJ, Dauskardt RH. Emollient molecule effects on the drying stresses in human stratum corneum. *Brit J Dermatol.* 2010;163:695-703.
- [131] Levine, R.A., Hung, J., Otsuji, Y., Messas, E., Liel-Cohen, N., Nathan, N., Handschumacher, M.D., Guerrero, J.L., He, S., Yoganathan, A.P., Vlahakes, G.J., 2002. Mechanistic insights into functional mitral regurgitation. *Current Cardiology Reports* 4(2), 125-129.

- [132] Lieber RL. 2009. *Skeletal Muscle Structure, Function, and Plasticity*. Lippincott Williams& Wilkins, Baltimore.
- [133] Limbert G, Taylor M. On the constitutive modeling of biological soft connective tissues. *Int J Solids & Structures*. 2002;39:2343-2358.
- [134] Limbert G. Dynamic skin wrinkles: Geometry or Mechanics? A probabilistic finite element approach. *ASME. Proc STLE/ASME Int Joint Tribology Conf* 2010:45-47.
- [135] Limbert G. A mesostructurally-based anisotropic continuum model for biological soft tissues - Decoupled invariant formulation. *J Mech Behavior Biomed Mat*. 2011;4:1637-1657.
- [136] Lewellyn ME, Barretto RP, Delp SL, Schnitzer MJ. Minimally invasive high-speed imaging of sarcomere contractile dynamics in mice and humans. *Nature*. 2008;454:784-788.
- [137] LoGiudice J, Gosain AK. Pediatric tissue expansion: Indications and complications. *J Craniofac Surg*. 2003;14:866-872.
- [138] Wong VW, Akaishi S, Longaker MT, Gurtner GC. Pushing back: Wound mechanotransduction in repair and regeneration. *J Invest Dermatol*. in press. doi:10.1038/jid.201.212.
- [139] Lubarda VA, Hoger A. On the mechanics of solids with a growing mass. *Int J Solids & Structures*. 2002;39:4627-4664.
- [140] Lubarda VA. Constitutive theories based on the multiplicative decomposition of deformation gradient: Thermoelasticity, elastoplasticity and biomechanics. *Appl Mech Rev*. 2004;57:95108.
- [141] Maganaris CN, Paul JP. 2002. Tensile properties of the in vivo human gastrocnemius tendon. *J Biomech*. 35:1639-1646.
- [142] Magnusson SP, Varici MV, Maganaris CN, Kjaer M. 2008. Human tendon behavior and adaptation, in vivo. *J Physiol*. 586:71-81.
- [143] Martins PALS, Natal Jorge RM, Ferreira AJM. A comparative study of several material models for prediction of hyper elastic properties: Application to silicone-rubber and soft tissues. *Strain*. 2006;42:135-147.
- [144] Matano T, Tamai K, Kurokawa T. Adaptation of skeletal muscle in limb lengthening: a light diffraction study on the sarcomere length in situ. *J Orthop Res*. 1994;12:193-196.
- [145] Mazza E, Papes O, Rubin MB, Bodner SR, Binur NS. Nonlinear elastic-viscoplastic constitutive equations for aging facial tissues. *Biomech Model Mechanobiol*. 2005;4:178-189.

- [146] McGee, E.C., Gillinov, A.M., Blackstone, E.H., Rajeswaran, J., Cohen, G., Najam, F., Shiota, T., Sabik, J.F., Lytle, B.W., McCarthy, McCarthy PM, Cosgrove DM, 2004. Recurrent mitral regurgitation after annuloplasty for functional ischemic mitral regurgitation. *Journal of Thoracic and Cardiovascular Surgery* 128(6), 916-924.
- [147] McGrath JA, Uitto J. Anatomy and organization of human skin. Chapter 3 in: Burns T, Breathnach S, Cox N, Griffiths C. *Rook's Textbook of Dermatology*. Volume 1, Eighth Edition; Blackwell Publishing. 2010.
- [148] McMahon J, Goriely A. Spontaneous cavitation in growing elastic membranes. *Math Mech Solids*. 2010;15:57-77.
- [149] Menzel A. Modelling of anisotropic growth in biological tissues - A new approach and computational aspects. *Biomech Model Mechanobiol*. 2005;3:147-171.
- [150] Menzel A. A fibre reorientation model for orthotropic multiplicative growth. *Biomech Model Mechanobiol*. 2007;6:303-320.
- [151] Menzel A, Kuhl E. Frontiers in growth and remodeling. *Mech Res Comm*. 2012;42,1-14.
- [152] Murtada SC, Arner A, Holzapfel GA. 2012. Experiments and mechanochemical modeling of smooth muscle contraction. Significance of filament overlap. *J Thero Bio*. 297:176-186.
- [153] Neal ML, Kerckhoffs, R. 2009. Current progress in patient-specific modeling. *Brief Bioinform* (2010) 11 (1): 111-126.
- [154] Neumann CG. The expansion of an area of skin by progressive distension of a subcutaneous balloon; use of the method for securing skin for subtotal reconstruction of the ear. *Plast Reconstr Surg*. 1959;19:124-130.
- [155] O'Dwyer NJ, Neilson PD, Nash J. 1989. Mechanisms of muscle growth related to muscle contracture in cerebral palsy. *Dev Med Child Neuro*. 31:543-547.
- [156] Opila KA, Wagner SS, Schiowitz S, Chen J. 1988. Postural alignment in barefoot and high-heeled stance. *Spine*. 13:542-547.
- [157] Otsuji, Y., Handschumacher, M.D., Schwammenthal, E., Jiang, L., Song, J.K. Guerrero, J.L., Vlahakes, G.J., Levine, R.A., 1997. Insights from three-dimensional echocardiography into the mechanism of functional mitral regurgitation direct in vivo demonstration of altered leaflet tethering geometry. *Circulation* 96(6), 1999-2008.
- [158] Padala, M., Hutchinson, R.A., Croft, L.R., Jimenez, J.H., Gorman, R.C., Gorman III, J.H., Sacks, M.S., Yoganathan, A.P., 2009. Saddle shape of the mitral annulus reduces systolic strains on the P2 segment of the posterior mitral leaflet. *Annals of Thoracic Surgery* 88, 1499-1505.

- [159] Padala, M., Gyoneva, L.I., Thourani, V.H., Yoganathan, A.P., 2014. Impact of mitral valve geometry on hemodynamic efficacy of surgical repair in secondary mitral regurgitation. *Journal of Heart Valve Disease* 23, 79-87.
- [160] Pamplona DC, de Abreu Alvim C. Breast reconstruction with expanders and implants. A numerical analysis. *Artificial Organs*. 2004;28:353-356.
- [161] Pamplona DC, Carvalho CR, Radwasnki H, Pitanguy I. Changes in the characterization of the human scalp due to the process of successive skin expansion. *Proc Mech Solids Brazil*. Eds: da Costa Mattos HS, Alves M. 2009;426-436.
- [162] Pamplona DC, Carvalho C. Characterization of human skin through skin expansion. *J Mech Mat Structures*. 2012;7:641-655.
- [163] Pamplona DC, Mota DEJS. Numerical and experimental analysis of inflating a circular hyperelastic membrane over a rigid and elastic foundation. *Int J Mech Sci*. 2012;65:18-23.
- [164] Pamplona DC, Velloso RQ, Radwanski HN. On skin expansion. *J Mech Behavior Biomed Mat*. 2013; accepted for publication.
- [165] Pang H, Shiwalkar AP, Madormo CM, Taylor RE, Andriacchi TP, Kuhl E. Computational modeling of bone density profiles in response to gait: A subject-specific approach. *Biomech Model Mechanobio*. doi: 10.1007/s10237-011-0318-y.
- [166] Pasyk KA, Austad ED, McClatchey KD, Cherry GW. Electron microscopic evaluation of guinea pig and soft tissue expanded with a self-inflating silicone implant. *Plast Reconstr Surg*. 1982;70:37-45.
- [167] Pasyk KA, Argenta LC. Histopathology of human expanded tissue. *Clinics Plast Surg*. 1987;14:435-445.
- [168] Pasyk KA, Argenta LC, Hassett C. Quantitative analysis of the thickness of human skin and subcutaneous tissue following controlled expansion with a silicone implant. *Plast Reconstr Surg*. 1988;81:516-523.
- [169] Pellerin, D., Sharma, R., Elliott, P., Veyrat, C., 2003. Tissue Doppler, strain, and strain rate echocardiography for the assessment of left and right systolic ventricular function. *Heart* 89 (Suppl III), iii9-iii17.
- [170] Preziosi L, Tosin AR. Multiphase modelling of tumour growth and extracellular matrix interaction: Mathematical tools and applications. *J Math Bio*. 2009;58:625-656.

- [171] Prot V, Skallerud B, Holzapfel GA. Transversely isotropic membrane shells with application to mitral valve mechanics. Constitutive modeling and finite element implementation. *Int J Num Meth Eng* 2007;71:987-1008.
- [172] Quaba AA, Wallace AF. The incidence of malignant melanoma (0 to 15 years of age) arising in large congenital nevocellular nevi. *Plast Reconstr Surg*. 1986;78:174-178.
- [173] Radovan C. Breast reconstruction after mastectomy using the temporary expander. *Plast Reconstr Surg*. 1982;69:195-208.
- [174] Rana M, Hamarneh G, Wakeling JM. 2013. 3D fascicle orientations in triceps surae. *J Appl Physiol*. 115:116–125.
- [175] Rausch MK, Bothe W, Kvitting JP, Göktepe S, Miller DC, Kuhl E. In vivo dynamic strains of the ovine anterior mitral valve leaflet. *J Biomech*. 2011;44:1149-1157.
- [176] Rausch MK, Dam A, Göktepe S, Abilez OJ, Kuhl E. Computational modeling of growth: Systemic and pulmonary hypertension in the heart. *Biomech Model Mechanobiol*. doi:10.1007/s10237-010-0275-x.
- [177] Rausch MK, Tibayan FA, Miller DC, Kuhl E. Evidence of adaptive mitral leaflet growth. *J Mech Behavior Biomed Mat*. 2012;15:208-217.
- [178] Rausch MK, Famaey N, O'Brien Shultz T, Bothe W, Miller DC, Kuhl E. Mechanics of the mitral valve: A critical review, an in vivo parameter identification, and the effect of prestrain. *Biomech Model Mechanobiol*. doi:10.1007/s10237-012-0462-z.
- [179] Rausch, M.K., Tibayan, F.A., Ingels, N.B., Miller, D.C., Kuhl E., 2013. Mechanics of the mitral annulus in chronic ischemic cardiomyopathy. *Annals of Biomedical Engineering* 41(10), 2171-2180.
- [180] Reeder SB, Wen Z, Yu H, Pineda AR, Gold GE, Markl M, Pelc NJ. 2004. Multicoil Dixon chemical species separation with an iterative least-squares estimation method. *Magn Reson Med*. 51:35-45.
- [181] Rivera R, LoGiudice J, Gosain AK. Tissue expansion in pediatric patients. *Clin Plast Surg*. 2005;32:35-44.
- [182] Rodriguez EK, Omens JH, Waldman LK, McCulloch AD. Effect of residual stress on transmural sarcomere length distributions in rat left ventricle. *Am J Phys*. 1993;264:H1048-H1056.
- [183] Rodriguez EK, Hoger A, McCulloch AD. Stress-dependent finite growth in soft elastic tissues. *J Biomech*. 1994;27:455-467.

- [184] Rosset A, Spadola L, Ratib O. 2004. OsiriX: An open-source software for navigating in multidimensional DICOM images. *J Digit Img.* 17:205–216.
- [185] Ryan, JM, Humphrey, JD”, Finite Element Based Predictions of Preferred Material Symmetries in Saccular Aneurysms *Annals of Biomedical Engineering*1999;27:641-647.
- [186] Schmid H, Pauli L, Paulus A, Kuhl E, Itskov M. How to utilise the kinematic constraint of incompressibility for modelling adaptation of soft tissues. *Comp Meth Biomech Biomed Eng.* doi: 10.1080/10255842.2010.548325.
- [187] Schmid H, Pauli L, Paulus A, Kuhl E, Itskov M. Consistent formulation of the growth process at the kinematic and constitutive level for soft tissues composed of multiple constituents. *Comp Meth Biomech Biomed Eng.* 2012;15:547-561.
- [188] Serup J, Jemec GBE, Grove GL. Handbook of Non-Invasive Methods and the Skin. Informa Healthcare. 2003.
- [189] Shively RE. Skin expander volume estimator. *Plast Reconstr Surg.* 1986;77:482-483.
- [190] Siefert, A.W., Touchton, S.A., McGarvey, J.R., Takebayashi, S., Rabbah, J.P., Jimenez, J.H., Saikrishnan, N., Gorman, R.C., Gorman, J.H., Yoganathan, A.P., 2013. In-vivo mitral annuloplasty ring transducer: Implications for implantation and annular downsizing. *Journal of Biomechanics* 46(14), 2550–2553.
- [191] Silver FH, Siperko LM, Seehra GP. Mechanobiology of force transduction in dermal tissue. *Skin Res Tech.* 2003;9:3-23.
- [192] Simpson CL, Patel DM, Green KJ. Deconstructing the skin. Cytoarchitectural determinants of epidermal morphogenesis. *Nature Rev Mol Cell Bio.* 2011;12:565-580.
- [193] Socci L, Pennati G, Gervaso F, Vena P. An axisymmetric computational model of skin expansion and growth. *Biomech Model Mechanobiol.* 2007;6:177-188.
- [194] Spector SA, Simard CP, Fournier M, Sternlicht E, Edgerton VR. Architectural alterations of rat hind-limb skeletal muscles immobilized at different lengths. *Exp Neurol.* 1982;76:94-110.
- [195] O’Sullivan K, McAuliffe S, DeBurca N. The effects of eccentric training on lower limb flexibility: A systematic review. *Brit J Sports Medicine.* 2012;doi:10.1136/bjsports-2011-090835.
- [196] Tabary JC, Tabary C, Tardieu C, Tardieu G, Goldspink G. 1972. Physiological and structural changes in the cat’s soles muscle due to immobilization at different lengths by plaster casts. *J Physiol.* 224:231–244.
- [197] Taber LA. Biomechanics of growth, remodeling and morphogenesis. *Appl Mech Rev.* 1995;48:487-545.

- [198] Taber LA, Eggers DW. Theoretical study of stress-modulated growth in the aorta. *J Theor Bio.* 1996;180:343-357.
- [199] Taber LA. 1998. Biomechanical growth laws for muscle tissue. *J Theor Bio.* 193:201–213.
- [200] Taber LA, Humphrey JD. Stress-modulated growth, residual stress, and vascular heterogeneity. *J Biomech Eng.* 2001;123:528-535.
- [201] Tahta, S.A., Oury, J.H., Maxwell, J.M., Hiro, S.P., Duran, C.M., 2002. Outcome after mitral valve repair for functional ischemic mitral regurgitation. *Journal of Heart Valve Disease* 11(1), 11-18.
- [202] Takei T, Rivas-Gotz C, Delling CA, Koo JT, Mills I, McCarthy TL, Centrella M, Sumpio BE. Effects of strain on human keratinocytes. *J Cell Physiol.* 1997;173:64-72.
- [203] Takei T, Mills I, Arai K, Sumpio BE. Molecular basis for tissue expansion: Clinical implications for the surgeon. *Plast Reconstr Surg.* 1998;102:247-258.
- [204] Taubin G, Zhang T, Golub G. 1996 Optimal surface smoothing as filter design. In: *Lecture Notes in Computer Science.* eds. B. Buxton, R. Cipolla. pp. 283–292. Springer Berlin Heidelberg.
- [205] Taylor RL. FEAP - A Finite Element Analysis Program. *User Manual, Version 8.2*, University of California at Berkeley, 2008.
- [206] Theodorou DJ, Theodorou SJ, Kakitsubata U, Lektrakul N, Gold GE, Roger B, Resnick D. Plantar fasciitis and fascial rupture: MR imaging findings in 26 patients supplemented with anatomic data in cadavers. *Radiographics.* 20:S181–S197.
- [207] Taylor RL. FEAP - A Finite Element Analysis Program. *Version 8.3, User Manual*, University of California at Berkeley, 2011.
- [208] Thompson FM, Coughlin MJ. 1994. The high price of high-fashion footwear. *J Bone Joint Surg.* 76:1586-1593.
- [209] Tsamis A, Cheng A, Nguyen TC, Langer F, Miller DC, Kuhl E. Kinematics of cardiac growth - In vivo characterization of growth tensors and strains. *J Mech Behavior Biomed Mat.* 2012;8:165-177.
- [210] van der Kolk CA, McCann JJ, Knight KR, O'Brien BM. Some further characteristics of expanded tissue. *Clin Plast Surg.* 1987;14:447-453.
- [211] Vandiver R, Goriely A. Differential growth and residual stress in cylindrical elastic structures. *Phil Trans R Soc A.* 2009;367:3607-3630.

- [212] van Rappard JHA, Molenaar J, van Doorn K, Sonneveld GJ, Borghouts JMHM. Surface-area increase in tissue expansion. *Plast Reconstr Surg.* 1988;82:833-839.
- [213] Verdier C, Etienne J, Duperray A, Preziosi L. Review: Rheological properties of biological materials. *Comptes Rendus Phys.* 2009;10:790-811.
- [214] Williams PE, Goldspink G. 1971. Longitudinal growth of striated muscle fibres. *J Cell Sci.* 9:751-767.
- [215] Williams PE, Goldspink G. 1971. The effect of immobilization on the longitudinal growth of striated muscle fibres. *J Anat.* 116:45-55.
- [216] Williams PE, Goldspink G. Changes in sarcomere lengths and physiological properties in immobilized muscle. *J Anat.* 1978;127:459-468.
- [217] Wisdom KM, Delp SL, Kuhl E. 2014. Review. Use it or lose it: Multiscale skeletal muscle adaptation to mechanical stimuli. *Biomech Mod Mechanobio.* available online first. doi:10.1007/s10237-014-0607-3.
- [218] Wollina U, Berger U, Stolle C, Stolle H, Schubert H, Zieger M, Hipler C, Schumann D. Tissue expansion in pig skin - A histochemical approach. *Anat Histol Embryol.* 1992;21:101-11.
- [219] Wong, J., Kuhl, E., 2014. Generating fibre orientation maps in human heart models using Poisson interpolation. *Computer Methodes in Biomechanics and Biomedical Engineering* 17, 1217-1226.
- [220] Wu KS, van Osdol WW, Dauskardt RH. Mechanical properties of human stratum corneum: Effects of temperature, hydration, and chemical treatment. *Biomaterials.* 2006;27:785-795.
- [221] Yoon JY, An DH, Yoo WG, Kwon YR. 2009. Differences in activities of the lower extremity muscles with and without heel contact during stair ascent by young women wearing high-heeled shoes. *J Orth Surg.* 14:418-422.
- [222] Zeng Y, Xu C, Yang J, Sun G, Xu X. Biomechanical comparison between conventional and rapid expansion of skin. *Brit Assoc Plast Surg.* 2003;56:660-666.
- [223] Zioupos P, Currey JD. 1998. Changes in the stiffness, strength, and toughness of human cortical bone with age. *Bone.* 22:57-66.
- [224] Zöllner AM, Buganza Tepole A, Gosain AK, Kuhl E. Growing skin - Tissue expansion in pediatric forehead reconstruction. *Biomech Mod Mechanobio.* in press. doi:10.1007/s10237-011-0357-4.
- [225] Zöllner AM, Buganza Tepole A, Kuhl E. On the biomechanics and mechanobiology of growing skin. *J Theor Bio.* 2012;297:166-175.

- [226] Zöllner AM, Buganza Tepole A, Gosain AK, Kuhl E. Growing skin - Tissue expansion in pediatric forehead reconstruction. *Biomech Mod Mechanobio*. 2012;11:855-867.
- [227] Zöllner AM, Abilez OJ, BI M, Kuhl E. Stretching skeletal muscle - Chronic muscle lengthening through sarcomerogenesis. *PLoS ONE*. 2012;7(10):e45661.
- [228] Zöllner AM, Holland MA, Honda KS, Gosain AK, Kuhl E. 2013. Growth on demand - Reviewing the mechanobiology of stretched skin. *J Mech Behavior Biomed Mat*. 28:495-509.
- [229] Zöllner AM, Pok JM, McWalter EJ, Gold GE, Kuhl E. On high heels and short muscles: A multiscale model for sarcomere loss in the gastrocnemius muscle. *J Theor Bio*. 2015;365:301310.
- [230] Zumstein MA, Frey E, von Rechenberg B, Frigg R, Gerber C, Meyer DC. Device for lengthening of a musculotendinous unit by direct continuous traction in the sheep. *BMC Vet Res*. 2012; doi:10.1186/1746-6148-8-50.
- [231] Zygote Media Group, Inc. The Zygote Solid 3D Heart Model, 2014.
- [232] Zygote Media Group, Inc. Zygote Solid 3d Heart Generations I & II Development Report. Technical Development of 3D Anatomical Systems, 2014.